

Microscale physico-chemical interactions between hydrodynamically confined liquids and immersed biological surfaces

Thèse N° 7705

Présentée le 31 octobre 2019

à la Faculté des sciences et techniques de l'ingénieur
Laboratoire de microsystemes 4
Programme doctoral en microsystemes et microélectronique

pour l'obtention du grade de Docteur ès Sciences

par

David Philipp TAYLOR

Acceptée sur proposition du jury

Prof. J. Brugger, président du jury
Prof. Ph. Renaud, directeur de thèse
Prof. A. van den Berg, rapporteur
Prof. B. Rapp, rapporteur
Prof. S. Maerkl, rapporteur

2019

Acknowledgements

The last four years of my life have been shaping in every sense – and will certainly remain in my memory as some of the most beautiful, fun and miraculous ones. I am deeply grateful to everyone who accompanied me in this time and these acknowledgements can reflect my gratitude only in parts.

I would like to first thank my supervisor and mentor Dr. Govind Kaigala for his guidance, patience and support in all matters, how weird and complicated they might have been, without ever being judgmental. I highly appreciate our open form of communication and am very grateful for your confidence in my abilities and your willingness to support at least some of my more explorational ideas. You always had an open door and took all possible (and impossible) measures to support me along my way.

I also hearty thank my academic supervisor Prof. Philippe Renaud for his wise guidance and support all through the last few years, as well as Prof. Todd Squires and his group at UCSB for their Californian hospitality and inspiring insights into the worlds of interfaces and rheology.

I would further like to thank my group at IBM Research in Rüschlikon. It was a pleasure and an honor working with you. I will miss short brakes at the pond and long brakes at the lake, just as well as fantastic brainstorming sessions with Dr. Robert Lovchik and Dr. Federico Paratore, philosophizing with Dr. Aditya Kashyap and political conversations with Dr. Xander van Kooten. Not to forget Anna, Lena, Deborah, Iago, Yuksel, Onur, the Juliens, Prerit and everybody else who has been part of the team – besides creating a fantastic working atmosphere, each of you has contributed to this work by countless discussions, hints and tips.

I would further like to thank my group manager Dr. Emmanuel Delamarche for having supported me since the first day of my master thesis. Going up the management chain, I would like to express my deep gratefulness to Dr. Walter Riess, who while managing a department of over a hundred researchers, some of them world-champions in their field, would never forget to take care of every single master student under his wings.

I also thank all colleagues from our Science and Technology department, who have also helped at many points with invaluable suggestions and highly skilled practical work, most of all the cleanroom staff (especially Ute Drechsler), the mechanical workshop staff (especially Marcel Bürge and Anel Zulic), as well as Dr. Darius Urbanas and Dr. Thilo Stöferle for their affinity to crazy ideas. I also thank the fantastic ZRL operations teams, from the “Lager” to the front-desk, who strive to support “their” researchers wherever they can.

Most of all, I thank my family, who missed their dad on many occasions within the last four years (even though I might have been physically present). All of us have invested a lot in this, our dissertation and I know it is an exceptional privilege to work towards a PhD, while at the same time building up a beautiful family. Rebecca, I thank you from the bottom of my heart for sacrificing yourself day for day to keep my back free. Levi, you were born just before I signed up for doctoral school and, now, just a week ago, your pre-school has started. Growing with you in these four years was certainly more shaping than any PhD could ever be. Noa, thank you for bringing even more sunshine to our lives and for being so patient with us three “big” ones. Also, thank you kids for reminding me each day what research actually is all about.

Thalwil, August 22, 2019

Acknowledgements

Abstract

In contrast to conventional microfluidics, where liquids are typically manipulated within closed channels, open-space microfluidics has emerged as a new class of techniques that are well suited for versatile interaction with biological substrates. In particular, non-contact microfluidic technologies, so called liquid scanning probes, allow to compartmentalize otherwise fully miscible liquids in the "open space" on immersed surfaces and are starting to translate from academic research to commercial products. One such family of liquid scanning probes localize liquids using hydrodynamic flow confinement (HFC). Such HFC-based liquid scanning probes enable controlling the physico-chemical microenvironments of immersed biological surfaces and thus are highly-suited for additive and subtractive patterning of surfaces and for interactions with cells on surfaces. This thesis presents a scaling analysis of HFC-based liquid scanning probes in the context of one such technology, the microfluidic probe (MFP). The analysis along each scaling dimension is based on first principle models and validated in the context of relevant biological applications.

To improve the efficiency in the use of expensive reagents, a method to recirculate a μl -scale volume of liquid within an HFC was developed. The concept was demonstrated in the context of forming a protein bio-array comprising 170 deposition sites using only 1.7 μl of protein-solution. The consumption of proteins was reduced by a factor of 10 compared to deposition without recirculation. For HFC-based interaction at larger length-scales, as needed in diagnostics, we further developed multi-layered vertical probe heads enabling novel aperture geometries and arrangements. These allow the homogeneous and multiplexed incubation of tissue sections with primary antibody solutions at processing times of a few minutes. Horizontal probe head were used to implement a multi-step protocol for immunohistochemical analysis of samples with an optimized trade-off between incubation time, signal levels and signal contrast.

Another key aspect in the translation of HFC-based liquid scanning probes is to counter two main failure modes impeding their long-term operation: 1) obstructions of apertures and channels by debris and, 2) deviations from the ideal probe-sample distance. Both these failure modes can be addressed via a simple design element, a microfluidic bypass channel. A liquid-filled, resistive bypass in the case of an obstruction intrinsically re-routes flow-paths and avoids spills. An air-filled, capacitive bypass allows to track the probe-sample distance up to 25 μm by observing the phase shift in transduced pressure pulses.

Towards enabling interactive microfluidic experimentation, we propose an HFC-based approach to form and re-configure flow trajectories of reagents, so-called virtual channels. Provided enough degrees of freedom in flow control, i.e. independently controllable injection and aspiration channels, user defined reagent-flow paths can be matched at high fidelity in real-time. We demonstrate the concept by using virtual channels to form patterns of proteins on a glass slide and by local lysis and staining of cell block sections.

The concepts, methods and devices presented in this dissertation contribute to the development of hydrodynamic confinements in the "open space" and, we think, are critical elements in the translation of HFC-based liquid scanning probes to applications in the life-sciences.

Keywords

Open-space microfluidics, liquid scanning probes, microfluidic probe, biological interfaces, hydrodynamic confinement, surface processing

Zusammenfassung

Im Gegensatz zur konventionellen Mikrofluidik, welche meist auf Flüssigkeitstransport innerhalb geschlossener Kanäle beruht, hat sich die «Open-Space-Mikrofluidik» als eine Klasse neuer Techniken etabliert, welche sich gut für die dynamische Interaktion mit biologischen Substraten eignen. Insbesondere nicht-kontaktbasierte Technologien, sogenannte Flüssigkeitsrastersonden, ermöglichen die Unterteilung von Flüssigkeitsvolumen oberhalb benetzter Oberflächen und finden zunehmend Anwendung in kommerziellen Produkten. Eine Klasse von Flüssigkeitsrastersonden ermöglicht die Lokalisierung von ansonsten mischbaren Reagenzien mittels hydrodynamischem Flusseinschluss (HFE). Die HFE-basierten Flüssigkeitsrastersonden ermöglichen eine präzise Kontrolle der physikalisch-chemischen Umgebungsbedingungen benetzter biologischer Oberflächen und eignen sich daher sehr gut für die additive und subtraktive Strukturierung solcher Oberflächen sowie für die Interaktion mit auf Oberflächen anhaftenden Zellen. Diese Dissertation präsentiert eine Skalierungsanalyse HFE-basierter Flüssigkeitsrastersonden am Beispiel eines repräsentativen Vertreters, der mikrofluidischen Sonde (MFS). Entlang jeder Skalierungsdimension basiert die Analyse auf ab-initio Modellen und umfasst eine Validierung im Kontext von aussagekräftigen Anwendungsbeispielen.

Um die Effizienz in der Verwendung kostspieliger Reagenzien zu verbessern, wurde eine Methode zur Rezirkulation von Flüssigkeitsvolumen im μl -Bereich innerhalb eines HFE entwickelt. Das Konzept wurde durch die Erzeugung eines Protein-Bioarrays validiert, wobei 170 einzelne Proteinpunkte mit insgesamt $1.7 \mu\text{l}$ Proteinlösung erzeugt wurden. Der Verbrauch von Proteinen wurde im Vergleich zu HFE-basierter Strukturierung ohne Rezirkulation um einen Faktor von 10 verringert. Für HFE-basierte Interaktionen mit grösseren Interaktionsflächen, zum Beispiel für Anwendungen in der Diagnostik, entwickelten wir mehrlagige Sondenköpfe, welche die Implementierung neuartiger Öffnungsformen und -anordnungen erlauben. Dies ermöglicht sowohl homogene, als auch simultane Mehrfachinkubation von histologischen Gewebeschnitten mit primären Antikörpern innerhalb weniger Minuten. Ein weiterer Typ von Sondenköpfen wurde für die Implementierung mehrerer sequentieller Prozessschritte von immunohistochemischen Analysen entwickelt und ermöglicht die Durchführung einer Analyse mit einem optimalen Kompromiss zwischen Prozessierungszeit, Signalintensität und Signalkontrast.

Ein weiterer zentraler Aspekt bei der Überführung von HFE-basierten Flüssigkeitsrastersonden hin zur Anwendung ist die Beseitigung zweier Hauptfehlermechanismen, welche längere Betriebsdauern erschweren: 1) Die Blockierung von Öffnungen und Kanälen durch Verunreinigungen und 2) Abweichungen vom idealen Sonden-Proben-Abstand. Diese beiden Hauptfehlermechanismen lassen sich mit einem simplem mikrofluidischen Designelement, einem Bypasskanal, beheben. Ein mit Flüssigkeit gefüllter Bypasskanal wirkt im Kanalnetzwerk als herkömmlicher Flusswiderstand und führt im Falle einer Blockade zu einer automatischen Umlenkung der Flusspfade, wodurch sich eine Leckage von Reagenzien verhindern lässt. Ein mit Luft gefüllter Bypasskanal wirkt im Kanalnetzwerk wie ein Kondensator und induziert eine Phasenverschiebung bei der Übertragung von Druckpulsen. Durch Messung dieser Phasenverschiebung lassen sich Sonden-Proben-Abstände bis zu $25 \mu\text{m}$ messen.

Um interaktive und dynamische mikrofluidische Abläufe zu ermöglichen, haben wir eine HFE basierte Methode zur Ausbildung und Umformung von Flusspfaden, sogenannter virtueller Kanäle, entwickelt. Lassen

sich die Flusspfade mit einer ausreichend hohen Anzahl an Freiheitsgraden, also durch genügend unabhängige Injektions- und Absaugöffnungen steuern, können nutzerdefinierte Flusspfade in Echtzeit experimentell dargestellt werden. Wir demonstrieren die Methode durch die gezielte Ablagerung von Proteinen auf Oberflächen, sowie die gezielte lokale Lyse von Zellblockschnitten.

Die Konzepte, Methoden und Geräte, welche in dieser Dissertation präsentiert werden tragen wesentlich zur Weiterentwicklung von HFEs bei und stellen kritische Elemente in der Überführung HFE-basierter Flüssigkeitsrastersonden hin zu Anwendungen in den Lebenswissenschaften dar.

Stichwörter

Open-Space-Mikrofluidik, Flüssigkeitsrastersonde, Mikrofluidische Sonde, biologische Interfaces, hydrodynamische Fokussierung, Oberflächenprozessierung

Contents

Acknowledgements	i
Abstract	iii
Zusammenfassung	v
Contents	vii
List of Figures	x
Chapter 1 Introduction	1
1.1 Open-space microfluidics	2
1.2 HFC-based liquid scanning probes	4
1.3 Structure and content of the thesis	7
Chapter 2 Hydrodynamic confinement of convected species across length-scales	11
2.1 Introduction	11
2.1.1 Basic principles of hydrodynamic confinement – Re and Pe	13
2.2 Hydrodynamic confinement in closed conduits	14
2.2.1 Stokes flow-based confinements	14
2.3 Confinements based on inertial effects	17
2.3.1 Confinements in non-Newtonian liquids	18
2.4 Hydrodynamic confinement between parallel plates	19
2.5 Hydrodynamic confinement in the open volume	22
2.6 Conclusion and outlook	23
Chapter 3 Biopatterning with recirculation of hydrodynamically confined nanoliter volumes of reagents	25
3.1 Abstract	25
3.2 Introduction	26
3.3 Efficient bio-patterning using the MFP	28
3.3.1 Diffusive transport between two laminar flows within the HFC	29
3.3.2 Convective transport and deposition of analytes on a surface	30
3.3.3 Results and discussion	32
3.4 Conclusion	35
3.5 Materials and Methods	36
3.5.1 Experimental section	36
3.5.2 Analyte consumption in a microchannel.	37

3.5.3	Operation of the microfabricated MFP head for liquid recirculation.....	37
3.5.4	Diffusive transport between two laminar flows within the HFC.....	38
3.5.5	Experimental validation of modelled loss per recirculation	40
3.5.6	Deposition of analytes on a surface using the MFP.....	42
Chapter 4	Surface interactions at the mm- and cm-scale using hydrodynamic flow confinements.....	45
4.1	Abstract	45
4.2	Introduction	46
4.3	Results and discussion.....	48
4.3.1	Vertical probe design and operating conditions for mm-scale HFCs.....	48
4.3.2	Slit-aperture probes.....	49
4.3.3	Aperture array probes	51
4.3.4	Immunohistochemistry on tissue sections	52
4.4	Horizontal probe heads for rapid μ IHC	54
4.5	Conclusion	57
4.6	Materials and Methods.....	58
4.6.1	Experimental section – vertical probe heads.....	58
4.6.2	Localized IgG assay on a PDMS-surface	60
4.6.3	Setup for localized processing of immersed surfaces.....	61
4.6.4	Reagent loading platform for multiplexing using aperture array designs	62
4.6.5	Experimental section –rapid μ IHC	62
Chapter 5	Fluidic bypass structures for improving the robustness of liquid scanning probes	65
5.1	Abstract	65
5.2	Introduction	65
5.3	Failure modes of liquid scanning probes and strategies to avoid them	67
5.3.1	Obstruction of apertures	67
5.3.2	Variations of the gap distance between probe and sample	68
5.4	Theory	69
5.4.1	Resistive bypass – dc mode.....	69
5.4.2	Capacitive bypass – ac mode	70
5.5	Results and Discussion	72
5.5.1	Resistive bypass for compensation of obstructions of apertures.....	72
5.5.2	Capacitive bypass for continuous distance sensing	73
5.6	Conclusion and Outlook	75
5.7	Materials and Methods.....	76
5.7.1	Experimental section	76

5.7.2	Estimation of parameters of flow-path elements.....	77
5.7.3	Nodal analysis - systems of linear equations	78
5.7.4	Optimization routines for definition of adequate input parameters.....	79
5.7.5	Measurement of relative phase shifts	80
5.7.6	Calculation of the relative movement amplitude of the rear interface.....	81
5.7.7	Modification of the model to fit the experimental data.....	82
Chapter 6	Reconfigurable microfluidics: real-time shaping of virtual channels through hydrodynamic forces	85
6.1	Abstract	85
6.2	Introduction	85
6.3	Results and discussion.....	86
6.3.1	Formation of virtual channels.....	86
6.3.2	Implementing key microfluidic functionalities using virtual channels.....	88
6.3.3	Dynamic flow patterns.....	89
6.3.4	Surface assays through virtual channels.....	90
6.3.5	Conclusion.....	91
6.4	Materials and Methods.....	93
6.4.1	Experimental section	93
6.4.2	Analytical description of 2D flow patterns.....	94
6.4.3	Reproduction of user designed flow patterns	95
6.4.4	Setup.....	96
6.4.5	In-situ polymerization	97
Chapter 7	Conclusions and outlook	99
7.1	Summary of results	101
7.2	Future directions	103
	References.....	106
	Curriculum Vitae.....	117

List of Figures

Figure 1.1: Timeline illustrating main advances in microfluidics.	1
Figure 1.2: Microfluidic techniques for localized interaction with immersed bio- interfaces.	3
Figure 1.3: Working principle of the microfluidic probe (MFP).	5
Figure 1.4: Dependencies in HFCs.	6
Figure 1.5: Analytical modelling of HFCs.	7
Figure 1.6: Structure of this thesis.	8
Figure 2.1: Stokes flow confinements in closed conduits.	15
Figure 2.2: Confinement through inertial forces.	18
Figure 2.3: Elasto-inertial confinements.	19
Figure 2.4: Stokes flow confinements between parallel plates.	21
Figure 2.5: Stokes flow confinements in the open volume.	22
Figure 3.1: Overview of biopatterning methods.	27
Figure 3.2: Scheme for liquid recirculation using pressure switching.	28
Figure 3.3: Scheme for analytical model of analyte transport in a hierarchical HFC.	29
Figure 3.4: Deposition efficiency using the MFP with different concentration of reagents.	31
Figure 3.5: Deposition of goat anti-IgG on IgG-coated polystyrene surface.	32
Figure 3.6: Multispot deposition of goat anti-IgG using recirculation with the MFP.	34
Figure 3.7: Microfabricated MFP head generating a hydrodynamic flow confinement.	38
Figure 3.8: Factors impacting the dilution of the processing liquid.	41
Figure 4.1: Strategies for HFC-based interaction on the cm-scale using vertical probe heads.	48
Figure 4.2: Design of slit-aperture and aperture array probes.	49
Figure 4.3: Optimization of slit-aperture probe designs and operating parameters.	51
Figure 4.4: Optimization of aperture-array designs.	52
Figure 4.5: Processing of tissue sections in a tissue microarray (TMA) on the cm-scale using HFC.	54
Figure 4.6: Current generation of horizontal probe heads.	55
Figure 4.7: Rapid μ IHC-analysis of tissue sections.	56
Figure 4.8: Characterization of reagents for rapid μ IHC.	57

Figure 4.9: Localized patterning of a substrate using mm-scale HFC.	60
Figure 4.10: Schematic illustration of the setup.	61
Figure 4.11: Sample loading and interfacing for probes with aperture-array designs.	62
Figure 5.1: Liquid scanning probes enable interfacing with immersed biological samples.	66
Figure 5.2: Failure mode caused by obstruction and solution based on a resistive bypass.	68
Figure 5.3: Failure mode caused by wrong gap distance and solution based on a capacitive bypass.	68
Figure 5.4: Analysis of microfluidic probe heads with resistive or capacitive bypass structures.	71
Figure 5.5: Resistive bypass for dc configuration.	73
Figure 5.6: Capacitive bypass for continuous monitoring of the gap distance.	74
Figure 5.7: Setup for tracking the gap distance via monitoring the motion of liquid-gas interfaces.	81
Figure 5.8: Motion of the interfaces in the coupling cavity due to the pressure modulation.	82
Figure 5.9: Adjusted model for ac configuration.	83
Figure 6.1: Formation of virtual channels inside a microfluidic flow cell.	87
Figure 6.2: Implementing basic microfluidic functionality with virtual channels.	88
Figure 6.3: Temporal control of flow patterns.	89
Figure 6.4: Localized immuno-patterning.	90
Figure 6.5: Targeted sequential sample processing.	91
Figure 6.6: Flow cell assembly for generation of reconfigurable flow patterns.	96
Figure 6.7: Array of syringe pumps for actuation of flow.	97
Figure 6.8: In-situ formation of alginate walls.	97
Figure 7.1: Developments presented herein and potential next steps.	99
Figure 7.2 Integrated MFP system.	100

Chapter 1 Introduction

Microfluidics stands as a summation of the characteristic properties that liquids reveal when confined within microscale boundaries, and of the use of these properties in miniaturized, fluid handling systems. In micro-scale flows, several physical processes, most notably mass transport, significantly differ from the macro-scale. In the micro-regime, effects such as viscous stresses, surface tension and wettability have a significant impact on the fluid behavior. From a technology perspective, microfluidics has strongly benefited from advances in the areas of microelectronics, microfabrication and microtechnology - key milestones of the field are illustrated in Figure 1.

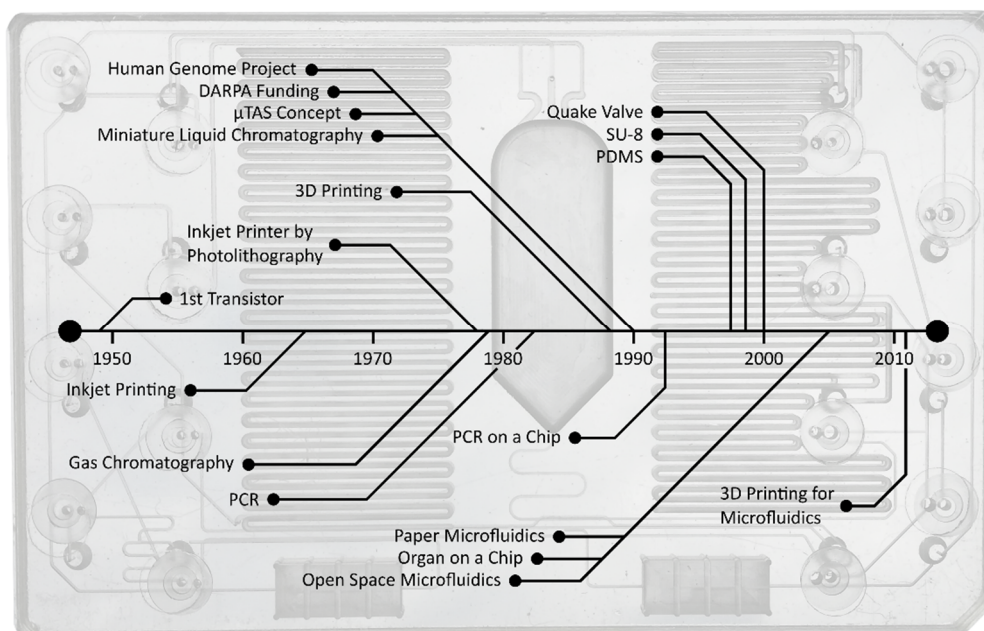


Figure 1.1: Timeline illustrating main advances in microfluidics. Initially enabled by advances made in microelectronics, microfluidics developed to a diverse and independent field with several sub-fields, using a variety of materials and fabrication approaches. Figure adapted from [1]. Background: Photograph of a microfluidic chip for the synthesis of radioactively labelled diagnostic tracers [2].

Photolithography, which was developed for the fabrication of micro-electronic structures, enabled the fabrication of the first more complex microfluidic devices in the 1970's, notably a gas-chromatography device developed by Terry and co-workers [3]. Subsequent research efforts significantly intensified only in the 1990's when microfluidic technologies were recognized as relevant for e.g. bio-defense and highly parallelized genomic analysis [1], [4]. In the following 30 years, a wide range of fabrication processes, materials and device concepts were developed, ranging from PDMS devices made by soft-lithography and paper microfluidics to 3D printed microfluidic structures.

There is a strong push in applying microfluidic methods and technologies in medicine and the life-sciences. While basic and applied research in the microfluidic field continuous to advance, several microfluidic techniques are nowadays in the transition towards industrial and diagnostic applications with increasing impact

and potential, as e.g. illustrated by commercial qPCR technology, wearable point-of-care devices for blood glucose monitoring and capillary electrophoresis devices for proteomics applications [5].

In the life sciences and in medical diagnostics there is a growing demand for methods enabling localized interaction with immersed biological surfaces without making mechanical contact [6]. As such, numerous biological interfaces are not compatible with traditional channel-based microfluidics. For this reason, “open space” microfluidics (see Figure 1.1) is emerging that allows for interaction with standard biological substrates such as Petri dishes, microtiter plates and glass slides [7]. This has enabled novel approaches and workflows involving multiplexed interaction with complex or scarce samples, e.g. surface-adherent cells [8]–[10], or the local analysis of spatially heterogeneous samples, such as sections of progressing tumor fronts [11]–[13].

1.1 Open-space microfluidics for interaction with bio-interfaces

The terms “biological surfaces” or “bio-interfaces” refer to surfaces on which biochemical and biophysical processes are implemented as part of *in-vitro* workflows in the life sciences and diagnostics. Bio-interfaces, which can be artificially created (e.g. DNA- or protein arrays), grown (e.g. surface-adherent cells), or sampled (e.g. tissue sections) (see Figure 1.2 bottom row), are central to a wide range of methods. Multiplexing and the resolution of spatial heterogeneity in such methods is often problematic, as bio-interfaces in most cases need to be kept in a liquid environment to prevent e.g. denaturation of proteins of interest, and spatially applied reagents would diffuse through the buffer medium and contaminate the remainder surface.

To address the incompatibility of conventional microfluidic closed-channel systems with several commonly used biological surfaces, the methods of open-space microfluidics have been proposed to enable localized, multiplexed interaction with such surfaces, as highlighted in Figure 1.2. At first, open-top channel systems were proposed [14]–[17]. Corresponding devices feature channel structures which are left open on one side and are brought in mechanical contact with an immersed biological surface to seal the off the channels and mechanically confine reagents to well-defined regions of interaction. Related techniques have successfully been applied to perform local sampling and multiplexing. Nonetheless, their versatility and applicability are limited, as the geometry of the area of interaction is pre-defined by fabricated channel structures and large sections of the probed bio-interfaces are destroyed through the required mechanical contact.

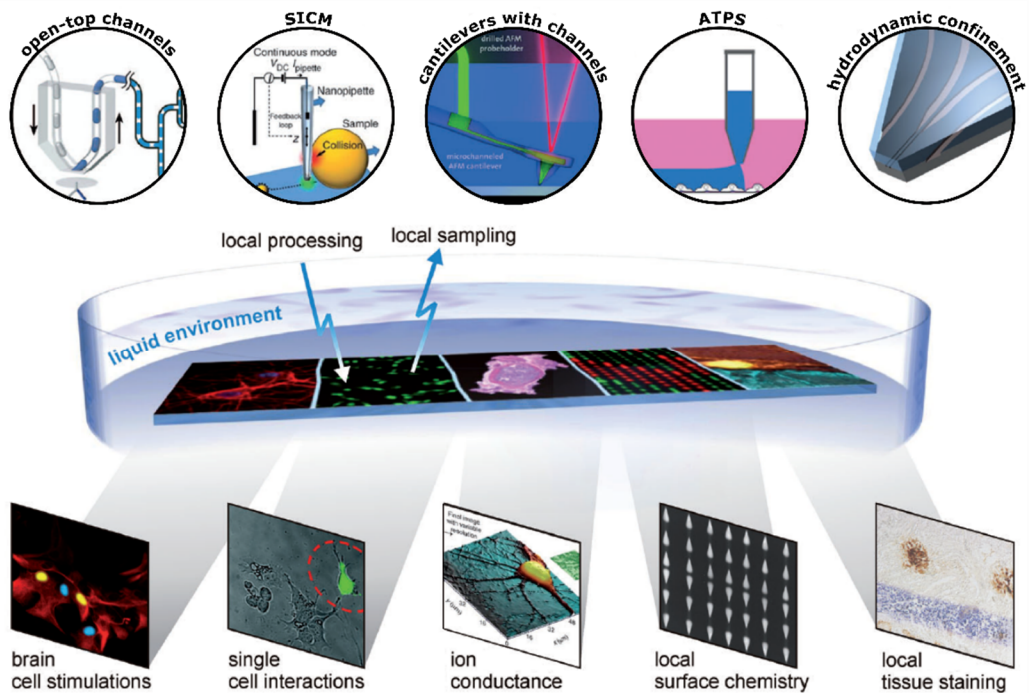


Figure 1.2: Microfluidic techniques for localized interaction with immersed bio-interfaces. Interfacing techniques are symbolically presented in the top row. While the first symbol represents open-channel approaches, which rely on mechanical contact, the remaining four symbols refer to the class of open-space microfluidics. The row in the bottom highlights some demonstrated applications, such as the stimulation of single cells, the formation of bio-arrays or the staining of samples in a diagnostic context. Figure adapted from [6].

So-called liquid scanning probes belonging to the class of open-space microfluidics take the concept of local interaction with immersed bio-interfaces further by dropping the requirement of mechanical contact: these methods enable to scan across bio-interfaces while confining interactions to specific locations. Attributes of such a technology are (adapted from [6]):

1. **Compartmentalization**
Enabling the confinement of reagents to well-defined regions of a bio-interface
2. **Non-invasive**
Avoiding direct contact with the substrates allows minimal perturbation of the sample.
3. **Immersed**
A liquid environment (water, buffer solution) prevents denaturation of the sample due to drying artifacts.
4. **Biocompatible**
Absence of toxic material and operating parameters such as pH and temperature should be compatible with the biological sample.
5. **Flexible**
Compatibility with different topographies, length-scales and materials.
6. **Interactive**
Real-time feedback (optical signal, electrical current, force) should be provided during operation.

Liquid scanning probes follow one of the following means of compartmentalization of liquids on top of immersed surfaces:

- Release of only minute amounts of reagents and transport of species via diffusion
Several groups have developed atomic force microscope (AFM) cantilevers with microfluidic structures, which allow high precision scanning of bio-interfaces and the release of tiny amounts of reagents at specific locations to e.g. stimulate a specific cell [9], [18]. The released volumes of reagents are so minute, that no significant contamination of neighboring regions occurs even though the reagent can freely diffuse through the buffer medium. Similarly, scanning ion conductance microscopy (SICM) allows for high resolution analysis of bio-interfaces while releasing minute amounts of ions [19], [20].
- Multiphase systems
Specifically, aqueous two-phase systems (ATPS) have been demonstrated as a useful approach to impede the free diffusion and confine reagents to specific areas of interaction [21], [22].
- Hydrodynamic flow confinement (HFC)
By formation of laminar, deterministic flow patterns on top of bio-interfaces by injection and re-aspiration of liquids at apertures in the head of a liquid scanning probe, the flow of reagents can be confined to well-defined regions [23]–[25].

In contrast to other approaches, HFC-based techniques rely on continuous flow of liquid in deterministic patterns to focus the flow of a processing within the flow of an immersion liquid. The processing and the immersion liquid are miscible, eliminating complications arising from effects related to surface tension and local changes in wetting properties of the scanned surfaces. Corresponding methods are well-suited for complex, sequential interactions with biological surfaces at length scales starting from a few μm up to a few hundred μm . Main representatives of this family of liquid scanning probes are the picoliter fountain pen [23], the multifunctional pipette [24] and the microfluidic probe [25].

1.2 HFC-based liquid scanning probes

The microfluidic probe (MFP) is a representative implementation of an HFC-based liquid scanning probe, which can be fabricated from a range of different materials such as silicon and glass, PDMS, SU8, COC and others [26]–[28]. Characteristic for the MFP is a probe head with a flat apex, about $1\text{ mm} \times 1\text{ mm}$ in size, with at least two apertures at its center. These apertures are linked to microfluidic channels within the probe head and can be used to inject and aspirate liquids (see Figure 1.3a). The MFP allows to form a hydrodynamic flow confinement (HFC) of a liquid reagent on immersed bio-interfaces. To this end, a bio-interface of interest is placed in an xy -scanning system on the stage of an inverted microscope (see Figure 1.3b). The substrate supporting the bio-interface and the bio-interface itself should be semi-transparent (such as tissue sections, surface adherent cells, protein arrays, etc.) to enable a proper set-up of the probe head and a monitoring of the flow confinement. The probe head, mounted on a z -stage and aligned with the optical path of the microscope, is immersed in the buffer liquid covering the bio-surface of interest. After an alignment ensuring that the apex is oriented parallel to the bio-interface, the gap between the apex and the bio-interface is set to about $20\ \mu\text{m}$ (varies for specific cases). Now immersion buffer is aspirated towards one of the apertures at a flow rate Q_a , forming a laminar, radial pattern of inward flow towards the aspiration aperture. If now a

reagent is injected from a second neighboring aperture at a much lower flow rate Q_i (usually lower by a factor of 3), this flow of reagent is confined in an HFC, bounded by the surrounding flow of immersion buffer.

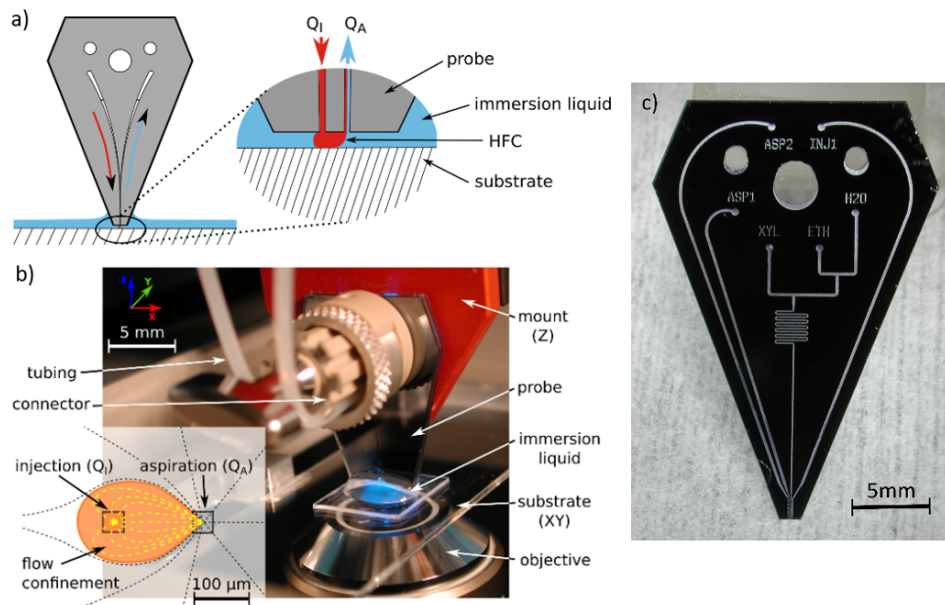


Figure 1.3: Working principle of the microfluidic probe (MFP). a) a probe head with microfluidic channels connected to apertures at the apex is positioned at about $20\mu\text{m}$ from a biological surface. A reagent is injected and simultaneously re-aspirated at a higher flow rate together with some of the surrounding immersion liquid to form a hydrodynamic flow confinement (HFC). b) Photograph of an actual MFP setup on the stage of an inverted microscope. The inset shows a sketch of the HFC as it would be seen through the microscope. c) Representative Si-glass probe head with four apertures (one of the injection apertures is linked to three inlets to allow a fast exchange of the processing liquid). The channel structures are etched into a silicon substrate and closed off by anodic bonding to glass [26].

The shape of the HFC can be tuned by variation of the flow rates Q_i and Q_A and the gap distance between probe head and bio-interface d , but it also depends on the design of the probe and the platform, such as the area of the apertures A_i and A_A , the spacing L between them, as illustrated in Figure 1.1. Usually a dye is added to the reagent, so the HFC can be monitored and adjusted in real-time while it is scanned across the bio-interface.

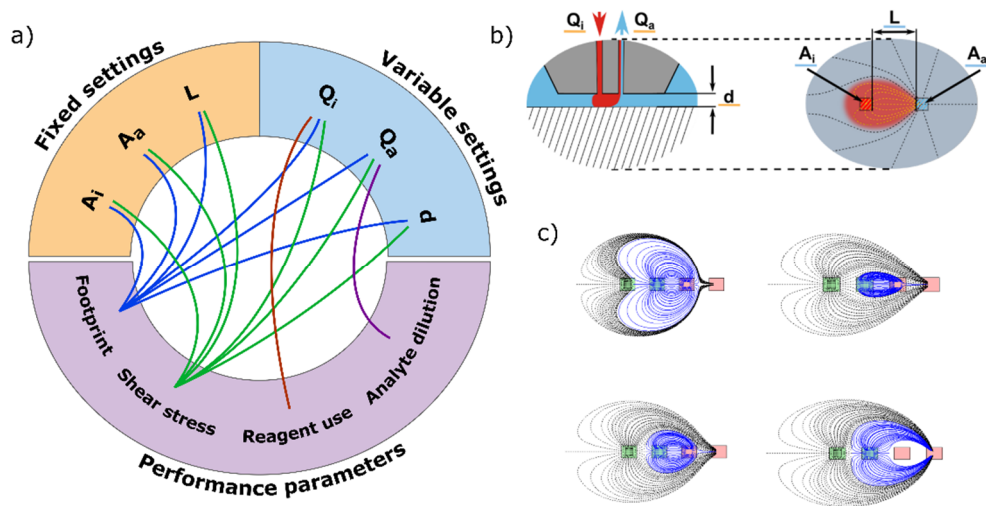


Figure 1.4: Dependencies of HFCs. a) The performance parameters of an HFC depend on several parameters, of which some are given by design and others can be varied dynamically. b) Illustration of key settings influencing the HFC. c) Exemplary illustration of nested HFCs formed by application of different flow rates at four apertures.

When formed between a probe head and a bio-interface, the flow patterns of an HFC can be modelled using the Hele-Shaw approximation for flow between two parallel surfaces. This allows to establish comprehensive analytical models of the transport and flow phenomena occurring in HFCs to predict and analyze for example the shape of the HFC, the resulting shear stresses, the area of interaction, or the residence time of fluid volumes along the interface between co-flowing streams to e.g. determine diffusive fluxes (see Figure 1.5). Such models can further be combined with models for reactions at surfaces to analytically analyze deposition processes. We grouped several such models in an analytical Matlab-toolbox (see Figure 1.5a), which was a highly valuable first resource to validate the concepts presented in this thesis and was specifically used for the work described in Chapter 3.

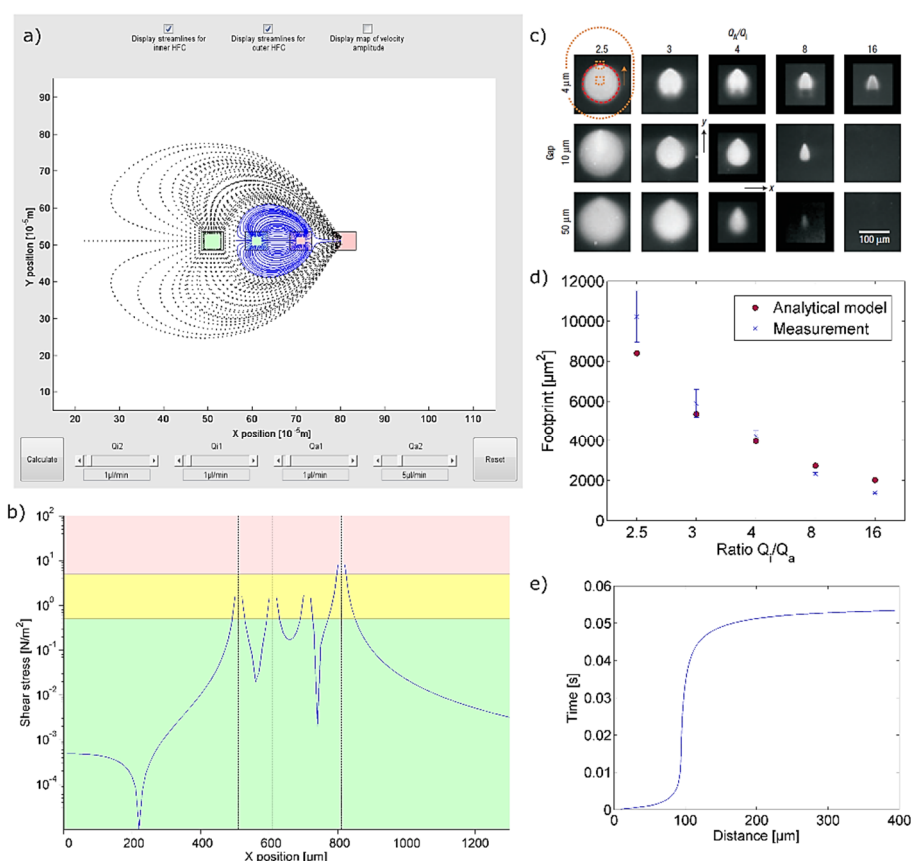


Figure 1.5: Analytical modelling of HFCs. a) Analytical modelling toolbox for shape-prediction of HFCs in Hele-Shaw configuration. b) Shear stress plot corresponding to the flow pattern depicted in a). c) Experimental demonstration of the dependency between HFC footprint, ratio of flow rates and gap distance (adapted from [25]). d) Area of the HFC footprint predicted by the analytical toolbox compared to experimental data. e) analytical, z-averaged plot of time versus travelled distance of a control volume of fluid moving along the interface within a nested HFC (interface between blue and black flow pattern in a)).

The MFP allows to treat well-defined areas of an immersed bio-interface at the scale of tens of μm up to hundreds of μm with sequences of reagents, while avoiding cross-contamination between individual areas of interaction. This opens a range of new opportunities grounding on multiplexed interaction with immersed bio-interfaces. The MFP has successfully been employed for relevant processes, such as localized immunohistochemistry of tissue sections, the local treatment of surface-adherent cells, local cell lysis for downstream DNA- and RNA- analysis, characterization of reaction constants, and the formation of protein-arrays [8], [29]–[31].

1.3 Structure and content of the thesis

This thesis seeks to further extend the applicability of HFC-based liquid scanning probes for interaction with bio-interfaces to explore the limits of corresponding techniques and to facilitate their adoption in the real-world.

To this end, Chapter 2 presents the theoretical basis and an overview of the state-of-the-art of hydrodynamic flow confinement and is based on a review article which is currently being composed for submission in fall 2019:

David P. Taylor, Prerit Mathur, Todd M. Squires, Philippe Renaud, Govind V. Kaigala, "Hydrodynamic confinement of convected species across length-scales," *manuscript under preparation*

Chapters 3-6 present a scaling analysis in the context of the MFP along four strategic dimensions (see Figure 1.6):

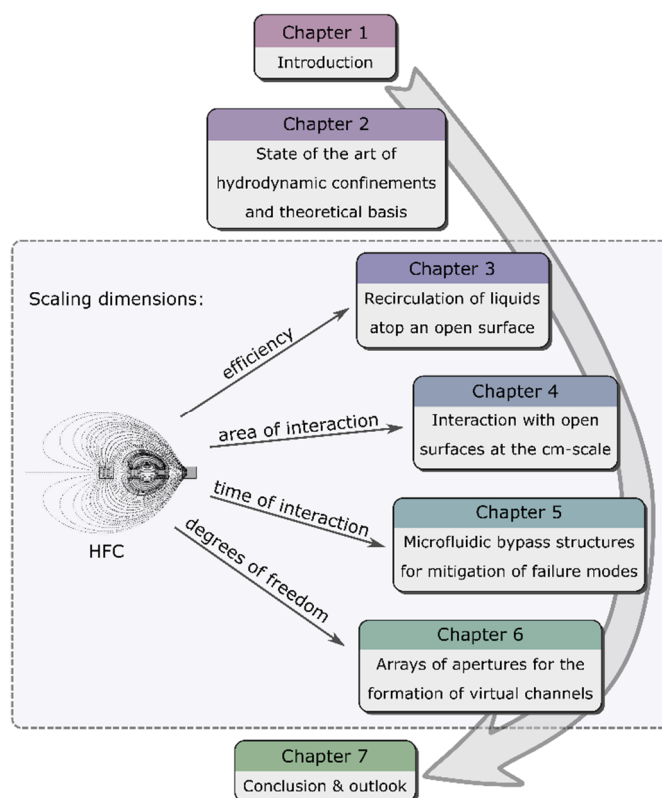


Figure 1.6: Structure of this thesis. At its core, this thesis is a scaling analysis of the techniques based on hydrodynamic flow confinement (HFC) along four strategic dimensions (chapters 3 – 6). The framework of the scaling analysis put forth in chapter 1.

Chapter 3 – Efficiency:

On account of the need to maintain a continuous flow of the processing liquid to confine the liquid, HFC-based liquid scanning probes can consume high amounts of reagents while interacting with a bio-interface. In the case of interaction times of several minutes, this leads to a consumption of several μl per interaction area, which, considering the exorbitant costs of many bio-reagents, can make this approach very expensive. In order to minimize the consumption of reagents without compromising other performance parameters, we developed a method to recirculate a given volume of reagent within the HFC to re-use it on several areas of interaction. This method was published in *Analytical Chemistry*, where it was highlighted on the front cover of the corresponding issue, and as a textbook chapter:

J. Autebert, J. F. Cors, D. P. Taylor, G. V. Kaigala. "Convection-enhanced biopatterning with recirculation of hydrodynamically confined nanoliter volumes of reagents." *Analytical chemistry*, **2015**, *88*(6), 3235-3242.

J. F. Cors, J. Autebert, A. Kashyap, D. P. Taylor, R. D. Lovchik, E. Delamarche, G. V. Kaigala. "Hierarchical Hydrodynamic Flow Confinement (hHFC) and Recirculation for performing Microscale

Chemistry on Surfaces,” *Open-Space Microfluidics: Concepts, Implementations, Applications*. Wiley-VCH Verlag GmbH, **2018** (ISBN: 978-3-527-34038-5)

Chapter 4 – Area of interaction

The ability to interact with only a single area at the scale of about 100 μ m to 200 μ m can limit the applicability of HFCs. For example, in the case of tumor tissue sections it is a requirement to analyze areas on a surface large enough for the results to be statistically relevant. It would be desirable to treat a cm-scale sample by little or no scanning motion of a liquid scanning probe. Based on analytical and numerical models, we developed strategies to enable the efficient processing of bio-interfaces at the mm- to cm-scale using probe heads with adapted aperture geometries. The models, scaling considerations, designs and a proof-of-concept were published in *Langmuir* and as a textbook chapter, while a complementary manuscript is currently being prepared for submission in fall 2019:

D. P. Taylor, I. Zeaf, R. D. Lovchik, G. V. Kaigala, “Centimeter-Scale Surface Interactions Using Hydrodynamic Flow Confinements,” *Langmuir*, **2016**, 32(41), pp. 10537–10544.

Lovchik, R. D.; Taylor, D. P.; Zeaf, I.; Delamarche, E.; Kaigala, G. V. “Hydrodynamic flow confinement-assisted immunohistochemistry from micrometer to millimeter-scale,” *Open-Space Microfluidics: Concepts, Implementations, Applications*. Wiley-VCH Verlag GmbH, **2018** (ISBN: 978-3-527-34038-5)

R. D. Lovchik, D. P. Taylor, G. V. Kaigala, “Rapid μ -IHC,” *manuscript under preparation*

Chapter 5 – Time of interaction

When testing HFC-based interactions in real-world applications, we identified two main failure modes. The first failure mode is triggered by an obstruction of the flow path of reagent. As liquid scanning probes are usually not set up in a clean-room environment, the concentration of dust particles in the immersion liquid naturally increases over time. Such particles can aggregate and clog the aspiration aperture, which can result in a breakdown of the HFC and a leakage of the reagent into the immersion liquid. The second failure mode is the deviation from the desired gap distance between probe head and bio-interface. This can occur when interfacing with surfaces, which either have an unknown surface topography or are not perfectly aligned with the scanning plane of the probe head. A too large gap distance results in insufficient interaction between HFC and bio-interface, a too small gap distance can result in mechanical contact and a damaging of probe head and bio-interface. When interacting with cm-scale samples in a routine manner, it is only a question of time when one of the named failure modes occurs. We make use of a simple, passive design element – a microfluidic bypass channel – which can be used in resistive mode when filled with liquid to intrinsically re-route the flow of reagent in the case of an obstruction, or in capacitive mode when filled with gas to continuously monitor the gap distance. This concept, along with corresponding analytical models and a proof of concept for either operational mode was published in *IEEE Transactions on Biomedical Engineering* and selected as a feature article for the 2019 September issue:

D. P. Taylor and G. V. Kaigala, "Fluidic bypass structures for improving the robustness of liquid scanning probes," *IEEE Transactions on Biomedical Engineering*, **2019**, doi: 10.1109/TBME.2018.2890602

Chapter 6 – Degrees of freedom in flow control

In this chapter we investigated how a significant increase of the degrees of freedom in flow control, that is individually controllable injection- and aspiration-flows, would impact the characteristics of the HFC. Along these lines, we increased the number of individually controllable injection- and aspiration-flows from two (standard MFP probe head) to 18. The prototype device featuring a corresponding array of apertures was not built as a liquid scanning probe, but the apertures are kept static relative to the bio-interface. It showed that providing enough degrees of freedom might make the need for scanning the HFC across a bio-interface obsolete in many cases: the flow of reagent can be re-shaped in real-time to address different regions of a bio-interface based on graphical user-input. The HFC can be set to take on the shape of conventional microfluidic channels, with the difference that the HFC-based “virtual channels” are not bounded by physical walls and can be dynamically re-configured. This concept is very well suited for the dynamic interaction with bio-interfaces, as the setup is comparably simple and robust and enables highly dynamic interaction across length scales. Virtual channels might also be interesting for the manipulation of suspended objects or sorting and fractionation processes. This concept together with the corresponding theoretical framework and several experimental implementations is currently being reviewed for publication in *Small* and was accepted for an oral presentation at the 2019 μ TAS-conference in Basel.

D. P. Taylor and G. V. Kaigala, "Reconfigurable Microfluidics: Real-time Shaping of Virtual Channels through Hydrodynamic Forces," *Small*, **2019**, under review (smll.201902854).

D. P. Taylor and G. V. Kaigala, "Reconfigurable Microfluidics: Real-time Shaping of Virtual Channels through Hydrodynamic Forces," *μ TAS conference proceedings*, **2019**.

Chapter 7 concludes this work presented in this dissertation by summarizing key findings and providing a view on potential further directions.

Chapter 2 Hydrodynamic confinement of convected species across length-scales

The content of this chapter is based on a draft version of a tutorial article on the topic of hydrodynamic confinements. We plan to submit the final article for publication in fall 2019.

David P. Taylor, Prerit Mathur, Todd M. Squires, Philippe Renaud, Govind V. Kaigala, “Hydrodynamic confinement of convected species across length-scales,” *manuscript under preparation*

To this work, I contributed following aspects:

- Outline and conceptualization
- Drafting of text and figures
- Theory for sections for 2.4 and 2.5

2.1 Introduction

Microfluidics has brought forward methods and devices for the precise manipulation of minute volumes of liquid, which allow to miniaturize established “on-bench” methods, while boosting efficiency, time-to-result, multiplexing and sensitivity – with wide-reaching impact in the life sciences and related industry [1]. In its very essence, “precise manipulation of fluids” refers to controlling the position and trajectory of one or several species of interest, which might be the molecular constituents of a pure homogeneous fluid itself, or entities contained within the matrix of a host fluid. Common examples for the first case are water and alcohol, which serve as reactants in a wide range of biochemical processes. The latter case on the lower end of the scale refers to small molecular species in a host liquid, such as ions setting a specific pH level with sizes in the Å-range, to molecules in solution, e.g. IgGs, with sizes around 15nm, and at the upper end of the scale also includes suspended objects, such as cells or beads with sizes in the range of up to 10 μm – 100 μm .

The precise manipulation of entities – be it the bulk of a fluid or an advected species – in a microfluidic setting is usually needed to either:

1. perform an interaction, e.g. a chemical reaction, in well-defined volume, or on a well-defined surface
2. sort entities based on specific properties to analyze or further process a population of interest
3. increase the local concentration of entities to boost signal levels or to speed up reaction kinetics

or combinations thereof. To enable precise manipulation of fluids and advected species, a wide range of approaches to confine fluids has been established (approaches for the confinement of bulk fluids are marked with \diamond , approaches for confinement of advected species are marked with \bullet):

- Physical boundaries $\diamond\bullet$

The formation of physical boundaries is the most traditional and straightforward approach to set up a confinement of fluids together with advected species to a desired volume. Some special implementations also allow to direct the diffusive motion of contained species by means of special wall-geometries in nano-scale cavities [32], [33]. Physical boundaries may be implemented in the form of solid walls or membranes (e.g. gel, paper, polymers) [3], [34]–[36], interfaces of immiscible phases [29], [37]–[39], transitions in the wetting properties (i.e. hydrophobic patches on surfaces) [40] and combinations thereof. Advantages of physical boundaries are their potential to fully suppress convection while often being permeable to the diffusion of specific species of interest [36]. On the downside, physical walls often have pre-configured geometries and, once formed, are difficult to reconfigure or remove. Further, the properties of semi-permeable physical boundaries often can be varied in only very narrow ranges and are thus unsuited for separating specific species.

- Gravity/centrifugal force ◊●

To confine a species of interest within a bulk fluid, gravitational and centrifugal forces might be used to spatially sort contained entities based on their relative density and counter the diffusive motion [41], [42].

- Chemical gradients ●

Chemical gradients can be set up to induce solvophoretic, or diffusiophoretic motion of a species of interest within a bulk fluid [36], [43]–[45].

- Thermal gradients ●

As the extent of diffusive motion increases with temperature, species contained in a fluid undergo thermophoresis and move downwards temperature gradients [46], [47].

- Magnetic fields ●

Magnetophoresis of ferro- and paramagnetic beads, molecules and even native cells allows the confinement of species contained within a fluid [48]–[50].

- Acoustic fields ◊●

Directed, acoustophoretic motion of species contained in a fluid can be induced by coupling ultrasonic acoustic waves into a fluid [51]–[53].

- Electromagnetic fields ●

Single particles, e.g. cells or beads, can be confined and manipulated by the means of focused laser light, so-called optical tweezers [54]–[56].

- Electrophoresis ●

The migration of species contained in a fluid along the gradient of an electric field, electrophoresis, is one of the most accessible and controllable methods for focusing and sorting of analytes of interest [57]–[59].

- Electroosmosis \diamond

The use of electroosmosis to confine the bulk motion of a fluid through the formation of by-design flow patterns has only recently been studied and demonstrated [60], [61].

- Hydrodynamic forces $\diamond\bullet$

The use of hydrodynamic forces in some variants allows to confine the motion of a bulk fluid together with all contained species, as well as the independent confinement of contained species in other variants. Compared to other methods, approaches based on hydrodynamic confinement are usually simple, as they make use of flow actuation infrastructure, which is common to most microfluidic applications. Further, hydrodynamic confinements are dynamically adjustable, versatile and scalable and allow high-throughput processing of samples, as corresponding methods inherently rely on the continuous flow of liquid [62], [63].

Each of these strategies naturally has its strength in specific scenarios. In the following sections we will discuss different forms of hydrodynamic focusing and highlight its strengths and limitations along with some practical examples. We structured the discussion based on the basic morphology of the discussed flow patterns: hydrodynamic confinement in fully closed conduits (section 2.2), hydrodynamic confinement between parallel plates (section 2.4) and hydrodynamic confinement in the open volume (section 2.5).

2.1.1 Basic principles of hydrodynamic confinement – Re and Pe

In the absence of other fields and forces, the motion of fluid molecules and dissolved and suspended species is a superposition of the directed, advective motion of the bulk fluid and the random diffusive motion of each individual entity. A precise manipulation of the location of a specific species by means of hydrodynamic forces therefore bases on two requirements: 1.) high spatio-temporal control of the flow pattern, i.e. the motion of the bulk, which 2.) significantly dominates the diffusive motion of single entities:

1. In contrast to mostly turbulent flow occurring in nature, flow fields need to be in the laminar regime to be deterministic and allow precise control of the bulk motion of the fluid. The laminar regime is characterized by a low Reynolds number $Re \ll 1$. The Reynolds number is the dimensionless ratio between inertial and viscous forces in a fluid, which moves at non-uniform velocity [64]:

$$Re = \frac{\rho u_0 L_0}{\mu} \quad (2.1)$$

Here, ρ is the density, μ the dynamic viscosity and u_0 the mean velocity of the moving fluid. L_0 is the characteristic length scale of a flow pattern, i.e. the inner diameter for flow in a pipe. The lower the flow velocity, or the higher the viscosity of a fluid, the smaller is Re and thus the likeliness to observe turbulence. For flows through circular ducts, the regime where the flow transitions from laminar to turbulent start at $Re = 2300$. In microfluidic devices, Re is most often smaller than 1, i.e. the bulk motion of fluid is laminar and deterministic.

2. A second dimensionless number, the Péclet number Pe indicates the relative significance of flow- and diffusion-based motion of a species of interest [64]:

$$Pe = \frac{u_0 L_0}{D} \quad (2.2)$$

Here, D is the diffusion constant of a species of interest and Pe thus is the ratio between convective, flow-based transport rates and diffusion-based transport rates. As hydrodynamic confinement requires convection to significantly outplay diffusion, large Pe numbers are required. It is therefore much more challenging to hydrodynamically confine small molecule and ions with diffusion coefficients at the scale of $10^{-3} \text{ mm}^2/\text{s}$, compared to suspended $10\mu\text{m}$ beads with diffusion coefficients at the scale of $10^{-16} \text{ mm}^2/\text{s}$. Nonetheless, it is well feasible to form microfluidic hydrodynamic confinements of small molecules with $Pe \gg 1000$.

2.2 Hydrodynamic confinement in closed conduits

Different strategies have been proposed to set up hydrodynamic confinements in closed conduits:

- Purely Stokes flow-based confinements
- Confinements based on inertial effects
- Confinement based on viscoelastic effects

2.2.1 Stokes flow-based confinements

Of all these strategies, purely Stokes flow-based focusing has been demonstrated first in devices for cell counting and is still used to line up cells one after another in fluorescence-activated cell sorting (FACS) [62]. Even though the overall flow is geometrically confined in a closed conduit, the flow of a fluid of interest can be confined in-plane, when sandwiched between two lateral sheath flows (see Figure 2.1a), or in 3D, when sandwiched between four sheath flows (see Figure 2.1b) [65]–[67]. In FACS, 3D confinement is often achieved by concentrically injecting the fluid to be focused from a round nozzle into the sheath flow, which is conceptually simpler, but not easily compatible with planar microfabrication technologies.

As Stokes flow classically is in the regime of $Re \ll 1$, the compressibility of the involved fluids and body forces, such as gravity or buoyancy, can be neglected, the Navier-Stokes equations describing the general motion of fluids in this case collapse to two linear, time-invariant equations [68]. Namely the Stokes equation describing the response of a bulk volume of fluid to a pressure gradient

$$-\nabla p + \mu \nabla^2 \mathbf{u} = 0 \quad (2.3)$$

and the corresponding expression for the conservation of mass, stating that the sum of all inflow and all outflow for any considered domain is equal zero

$$\nabla \cdot \mathbf{u} = 0 \quad (2.4)$$

Here p stand for the scalar pressure field, \mathbf{u} for the velocity vector field and μ for the dynamic viscosity of the fluid. As not dependent on time, Stokes flow is fully reversible. Above equations can be solved analytically to determine the flow field in a microfluidic cavity by applying the corresponding boundary conditions (position of walls and pressure, respectively flow at openings) [69]. For confinements as depicted in Figure 2.1a and b, analytical solutions are available also for sheath and sample liquids of different viscosity [67].

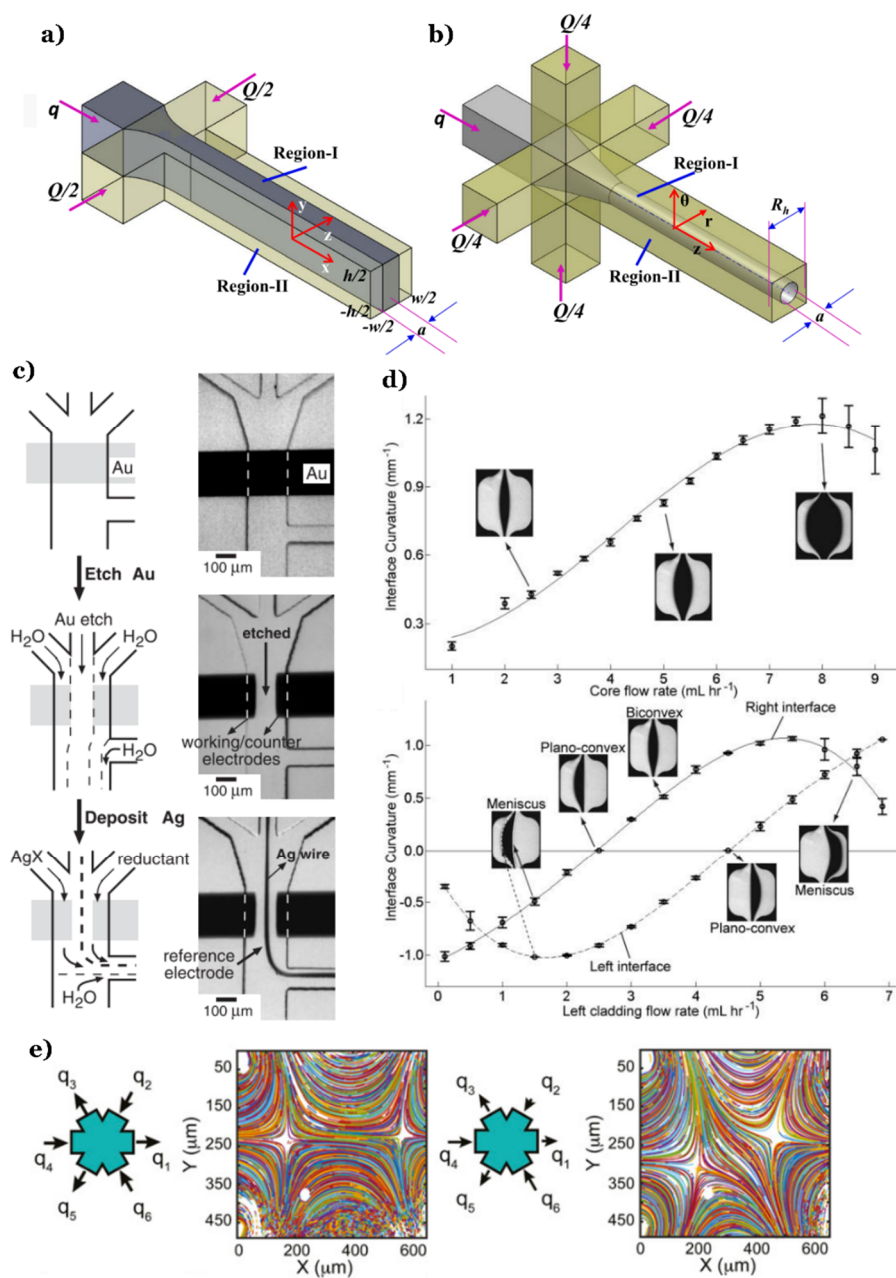


Figure 2.1: Stokes flow confinements in closed conduits. a) 2D focusing of a sample stream between two sheath streams. b) 3D focusing of a sample stream between four sheath streams, adapted from [67]. c) Localized deposition and removal of materials inside microchannels, adapted from [70]. d) formation of liquid-core-liquid-cladding lenses via hydrodynamic focusing of a liquid with higher refractive index, adapted from [71]. Formation of dynamically controllable stagnation points for the simultaneous position control of suspended objects, adapted from [72].

Besides the linear arrangement of cells on FACS; Stokes flow hydrodynamic confinements have been used for the localized deposition and removal of materials in specific areas of the walls of microfluidic channels, to e.g. pattern electrodes (see Figure 2.1d) [70]. Further, the formation of reconfigurable liquid-core-liquid-cladding lenses, bases on the confinement of a liquid with a high refractive index than the surrounding sheath liquid (see Figure 2.1e) [71], [73]. As highlighted in Figure 2.1b, stagnation points can be formed by appropriately setting the flow boundary conditions at the openings of a microfluidic chamber. Though the flow velocity at a stagnation point is zero, a particle will not remain stable at this position: any slight, diffusion-induced motion away from the stagnation point would result in unbalanced forces on the particle and its advection away from the stagnation point. In the case the flow boundary conditions are controlled in a closed loop based on the optically measured particle position, deviations of the particle away from the stagnation point

Tutorial 1 – Diffusion across an interface

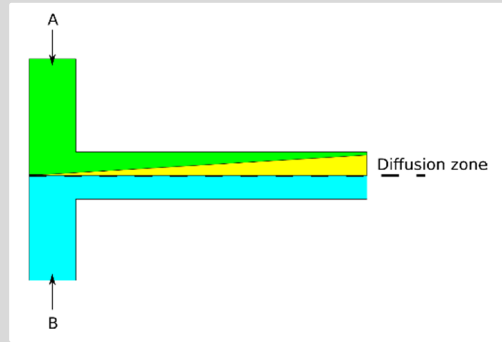
Strictly speaking, two laminarly co-flowing streams also hydrodynamically confine each other to either side of the microfluidic channel they share. This maybe simplest form of hydrodynamic confinement, the T sensor, is a good object of study to demonstrate how to estimate the role of diffusion in Stokes flow-based confinements.

The transient 1D diffusion equation has the form:

$$\frac{\partial C}{\partial t} = D \frac{\partial^2 C}{\partial y^2} \quad (2.5)$$

Assuming a step function as initial condition, the analytical solution is already known as

$$C(y, t) = \frac{C_0}{2} \left[1 - \operatorname{erf} \left(\frac{y}{2\sqrt{Dt}} \right) \right] \quad (2.6)$$



In the described case, the transport of advected species in the region of the interface between the two streams, where the flow velocity is u , can be described as a superposition of advection and diffusion:

$$\frac{\partial C}{\partial t} + u \frac{\partial C}{\partial x} = D \frac{\partial^2 C}{\partial y^2} + D \frac{\partial^2 C}{\partial x^2} \quad (2.7)$$

As the situation is in steady state with the assumption that $\frac{\partial^2 C}{\partial y^2} \gg \frac{\partial^2 C}{\partial x^2}$, above equation becomes

$$u \frac{\partial C}{\partial x} = D \frac{\partial^2 C}{\partial y^2} \quad (2.8)$$

Now, choosing the variable x/v as a time like coordinate, a T sensor has the same analytical solution as the 1D diffusion equation. Thus here, the concentration field along the interface is:

$$C(x, y) = \frac{C_0}{2} \left[1 - \operatorname{erf} \left(\frac{y}{2\sqrt{D \frac{x}{u}}} \right) \right] \quad (2.9)$$

can be actively countered and Stokes flow can be used to simultaneously control the positions of several suspended objects with sizes between 2 μm and 20 μm [72], [74].

2.3 Confinements based on inertial effects

Approaches relying on inertial hydrodynamic effects for the confinement of fluid flow or of advected species, usually have characteristic Reynolds number between 10 and 100 [75]. In this regime, the flow is mostly laminar, but flow patterns are usually not reversible anymore: e.g. region of flow circulation forming in the wake of obstacles induce asymmetrical deformation of flow, which would not be observable in the Stokes regime. In the inertial regime, so-called secondary flows arise, which act on the bulk fluid when flowing in curved channels, or in curved lines around an obstacle, such as a pillar (see Figure 2.1a and c) [76]–[78]: in curved channels, the fluid in the channel center flows faster than the fluid close to the walls and thus experiences a larger centrifugal force pointing away from the center of curvature. This results in a secondary flow, perpendicular to the main flow direction. In curved channels, this secondary flow is called Dean flow (see Figure 2.2d). Significant secondary flow arises in flows through curved channels for Dean numbers $De > 54$ [78]. The dean number is defined as

$$De = Re \cdot \sqrt{\frac{d}{2r}} \quad (2.10)$$

Here, r is the curvature radius of the channel and d is the diameter of the channel. Secondary flows in curved channels have been used to focus the flow of a sample fluid within another fluid. In analogy, customized arrays of pillars or chevrons allow to focus the flow of a sample liquid to specific regions of a microchannel.

Also advected particles experience forces, which only arise in the inertial regime (see Figure 2.2g) [79]–[81]:

- A drag force F_D resulting from Dean flows introduced above
- A wall-effect lift-force F_{WL} arising in vicinity of walls, which is directed away from the nearest wall
- A shear gradient lift force (also called Saffman lift force) F_{SL} directed downwards shear gradients

In the inertial regime, particles flowing within microchannels will adapt positions in the channel cross-section where the named forces equilibrate. As F_{WL} and F_{SL} scale with $\sim a^4$, where a is the characteristic dimension of the advected particles, inertial forces are well suited to separate particles based on their size [82]. Demonstrated application include the purification of circulating tumor cells, as well as the separation of red blood cells from other entities [83]–[86].

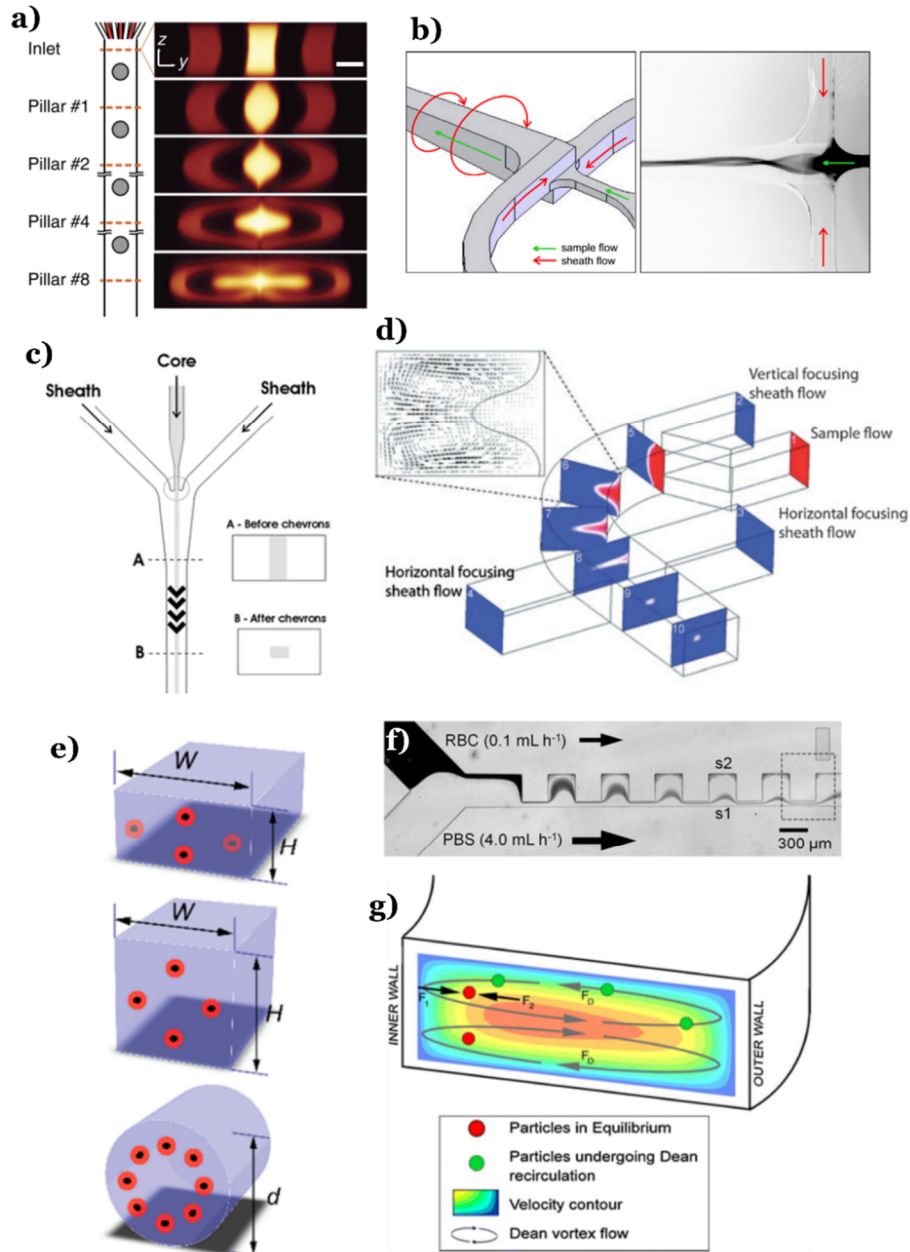


Figure 2.2: Confinement through inertial forces. a) Sequences of pillars for the manipulation of the cross-sectional position and morphology of co-flowing streams, adapted from [87]. b) 3D focusing of a sample stream using only two sheath streams with the help of inertial effects, adapted from [88]. c) manipulation of the cross-sectional position and morphology of co-flowing streams using sequences of grooves, adapted from [89]. d) manipulation of the position of sample streams using Dean flow, adapted from [90]. e) Equilibrium position of particles advected in inertial flow for different channel geometries, adapted from [63]. f) Inertial purification of red blood cells, adapted from [83]. (g) Equilibrium positions in curved inertial flow, $F_1 = F_D + F_{WL}$, $F_2 = F_{SL}$, adapted from [81].

2.3.1 Confinements in non-Newtonian liquids

The use of non-Newtonian liquids gives rise to additional forces acting on particles travelling in the fluid in parallel and perpendicular to the main flow direction. This opens further possibilities to focus particles to either specific cross-sectional regions, or to separate entities along the direction of flow.

Leshansky et al. demonstrated in 2007 that microparticles can be ‘tuned’ to follow specific flow paths in a microchannel due to elastic forces of polymer chains and further provide analytical expressions for particle trajectories based on a Poiseuille flow profile in rectangular microchannels [91].

Combination of viscoelastic and inertial forces can be leveraged to separate and confine advected species with unprecedented resolution and efficiency (see Figure 2.3) [92].

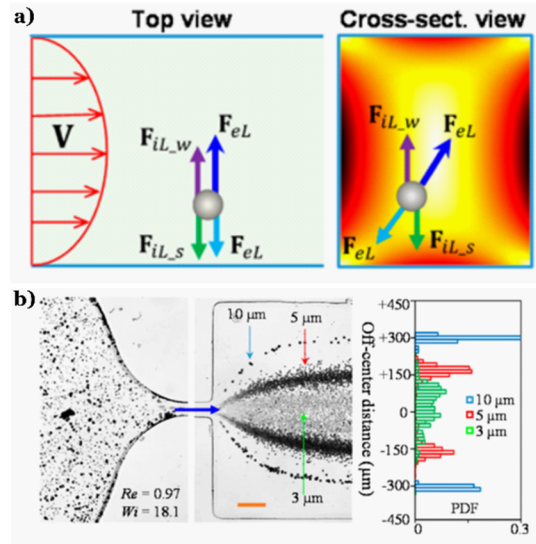


Figure 2.3: Elasto-inertial confinements. a) Analysis of forces on a particle in a viscoelastic fluid flowing in a straight rectangular microchannel: the fluid elasticity-induced lift F_{eL} directs the particle toward the channel center and four corners, the wall-induced inertial lift $F_{iL,w}$ and the shear gradient-induced inertial lift $F_{iL,s}$ direct the particle toward the channel center and wall, respectively ($F_{iL,w}$ and $F_{iL,s}$ are indicated only for the closest lateral wall). b) Experimental demonstration of particle separation in a straight channel (the orange scale bar represents 100 μ m), both adapted from [92].

2.4 Hydrodynamic confinement between parallel plates

Hydrodynamic confinements between parallel plates are of increasing importance in research and technology, as they are employed by liquid scanning probes to form a hydrodynamic flow confinement of a reagent on top of open biological surfaces [6], [25], [93]. This enables the localized and multiplexed processing of biological surfaces, such as surface-adherent cell cultures or tissue sections from biopsies, which could only be processed globally in conventional workflows.

While flow between parallel plates is often assumed in theoretical studies for e.g. analyzing inertial forces acting on suspended particles [79], experimentally demonstrated methods of hydrodynamic confinement between parallel plates to the best of our knowledge all rely on pure Stokes flow.

For flow between parallel plates, lateral walls, if present, are spaced far apart compared to the distance between the bottom and top confining surfaces and their impact on the flow pattern can be neglected. Further, for flat parallel plates, the flow pattern in z-direction (perpendicular to the parallel plates) is known to be parabolic. Flow patterns of Newtonian liquids with uniform viscosity can therefore be treated as two-dimensional, inviscid flow and be conveniently analyzed by means of potential flow theory [94]. Distant and straight lateral walls can be directly implemented as slip-boundaries using the method of images. The method can also be applied to more complex boundary geometries by conformal mapping to a geometry with known

solution. As the notation is more convenient, 2D potential flow problems are often analyzed in the complex plane.

The position of the m^{th} source on a corresponding complex plane is therefore given by a complex number $c_m = x_m + i \cdot y_m$. The complex potential Ω_m created by this source at any position $c = x + i \cdot y$ is

$$\Omega_m(c) = \phi + i\psi = \frac{Q_m}{2\pi} \cdot \ln(c - c_m) \quad (2.11)$$

The real part of the complex potential is the velocity potential ϕ , whereas the complex part is the stream function ψ . The complex potential is created by a set of n sources and can be directly written as linear superposition of the single contributions $\Omega = \Omega_1 + \dots + \Omega_n$.

Tutorial 2 – Potential flow

Let us assume a source at $s=1+i \cdot 1$ between two perpendicular walls, which coincide at the (inwards facing) corner $c=0+i \cdot 0$.

Walls (i.e. frictionless, no-flow boundary conditions) can be implemented through mirroring (the flow velocity along line perpendicular to axis connecting two sources of same strength and sign as zero):

Mirror sources: $m_1=-1+i \cdot 1$, $m_2 = -1-i \cdot 1$ and $m_3=1-i \cdot 1$

Mirror images are treated as regular sources in all following operations:

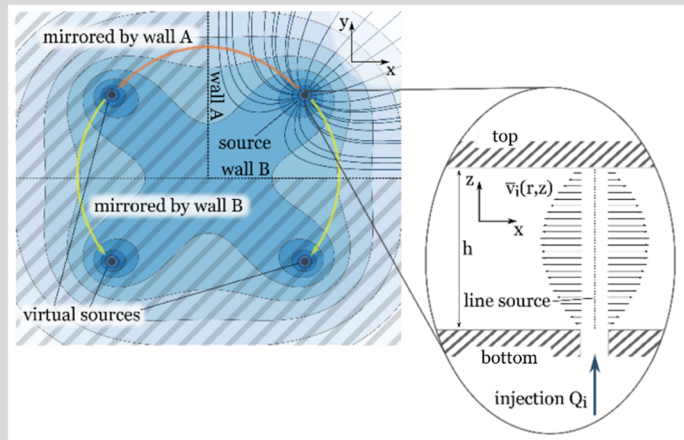
$$\begin{aligned} \Omega(c) = \frac{Q}{2\pi} \cdot \left(\ln(c - (1 + i \cdot 1)) + \ln(c - (-1 + i \cdot 1)) + \ln(c - (-1 - i \cdot 1)) \right. \\ \left. + \ln(c - (1 - i \cdot 1)) \right) = \frac{Q}{2\pi} \cdot \ln(c^4 + 4) \end{aligned} \quad (2.12)$$

And:

$$\vec{v}(c) = u(c) + i \cdot w(c) = \frac{d}{dc^*} \left(\frac{Q}{2\pi} \cdot \ln(c^4 + 4) \right) \quad (2.13)$$

Zero pressure boundaries (boundaries open to the environment) are implemented through mirroring sources with opposite sign.

Two parallel walls would result in an infinite number of mirror images. For such a case, a far field approximation may be used after a finite number of mirror images.



The complex flow velocity vector $\vec{v}(c)$ at a given position c can be conveniently derived from the complex potential $\Omega(c)$ by differentiation:

$$\vec{v}(c) = u(c) + i \cdot w(c) = \frac{d\Omega(c)}{dc^*} = \frac{d}{dc^*} \sum_{m=1}^n \frac{Q_m}{2\pi} \cdot \ln(c - c_m) \quad (2.14)$$

Here, $*$ denotes the complex conjugate and u and w are the velocity components along the real and the imaginary axes, respectively.

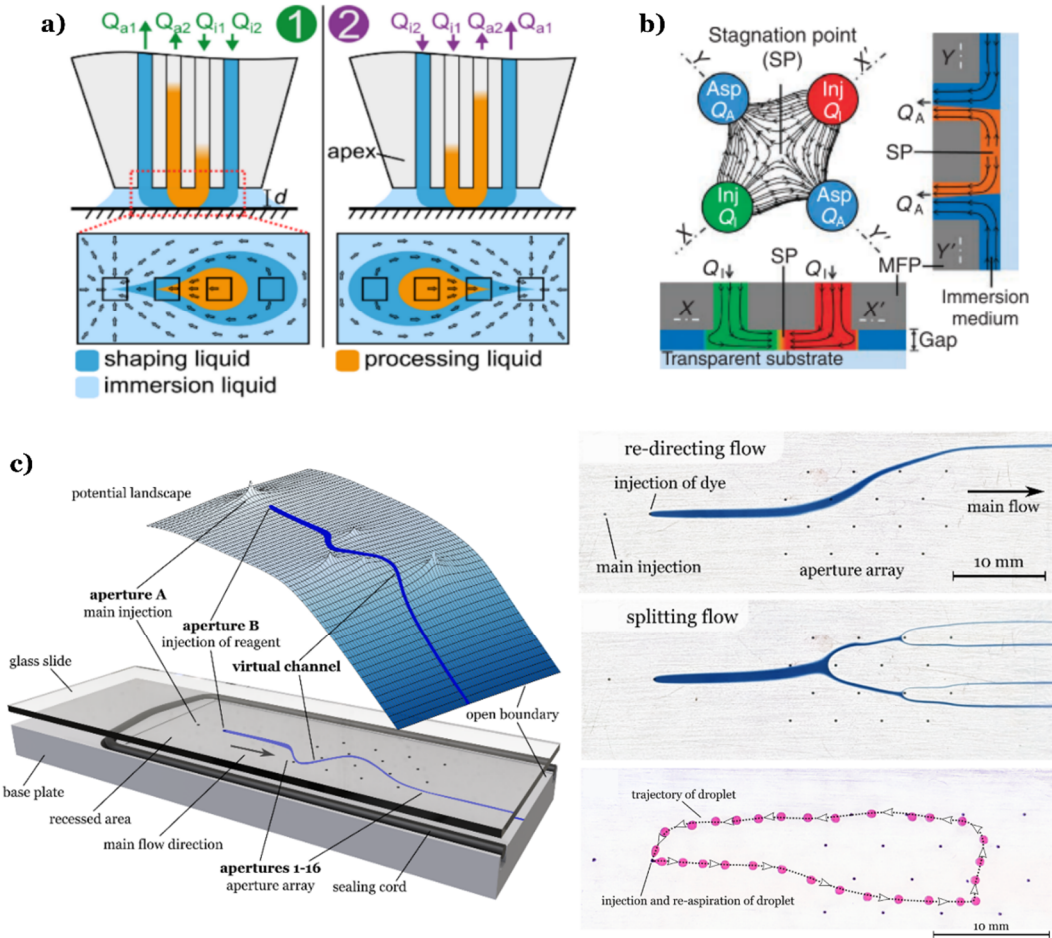


Figure 2.4: Stokes flow confinements between parallel plates. a) A nested flow confinement enabling the re-circulation of a reagent atop a surface, adapted from [30]. b) A microfluidic quadrupole for the formation of concentration gradients, adapted from [93]. c) Microfluidic multipoles enabling the formation of channel-like flow patterns and e.g. dynamic splitting, or the positioning of suspended objects.

For localized interaction with immersed biological surfaces, a liquid scanning probe with the flat apex, which is the top confining surface, is brought close (about 20-100 μm) to the sample of interest, which is the bottom confining surface. In the simplest configuration, a processing liquid is injected from an aperture in the probe head and simultaneously aspirated back at a higher flow rate into a second aperture together with some of the surrounding immersion liquid, to hydrodynamically confine the processing liquid. Demonstrated applications include the analysis of biopsies, analysis of surface-adherent cells and efficient formation and screening of bio-libraries in the form of protein arrays [8], [26], [30].

Lately, probe heads with many apertures, or even more generalized, mechanically fixed surfaces with arrays of holes, have been used to form more complex flow patterns atop biological surfaces [95]. In combination with above introduced complex potential flow model, such a device enables the direct implementation of user-designed flow patterns to form reconfigurable “virtual channels”, which enables dynamic and interactive experimental workflows, alleviating many complications linked to the tedious design and manufacturing process of microfluidic devices. Furthermore, these approaches can be applied to perform other established microfluidic functions in a highly versatile and dynamic way, such as splitting microfluidic flows to e.g. implement sorting or fractionation functionality, or the motion and positioning of suspended objects by hydrodynamic forces.

2.5 Hydrodynamic confinement in the open volume

Only few demonstrated microfluidic techniques rely on the formation of hydrodynamic flow confinements in un-bounded, open volumes (see Figure 2.5) [23], [24]. As even these implementations were conceived for the interaction with immersed surfaces, as there currently is little practical need for the formation of microfluidic hydrodynamic flow confinements in the open volume. To the best of our knowledge, demonstrated implementations of hydrodynamic confinements in open volumes all base on Stokes flow.

Assuming a homogeneous viscosity and Newtonian behavior, three-dimensional flow can also be analyzed via potential flow theory. Here, it is often practical to work in a spherical coordinate system. A source of strength Q located at $r=0$ causes a velocity potential ϕ :

$$\phi = -\frac{Q}{4\pi r} \quad (2.15)$$

And the resulting velocity field is

$$V_r = \frac{\partial \phi}{\partial r} = \frac{Q}{4\pi r^2}, V_\theta = V_\varphi = 0 \quad (2.16)$$

As for the 2D-case, flow fields formed by several sources can be superimposed to compute the resulting net flow field.

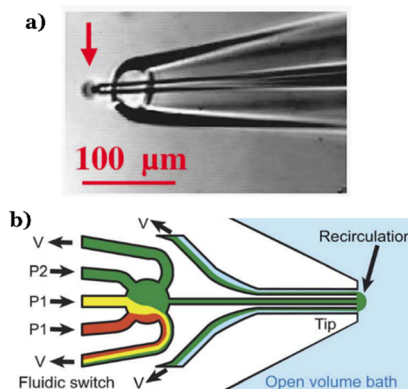


Figure 2.5: Stokes flow confinements in the open volume. a) co-axial glass pipettes (inner pipette for injection, outer pipette for aspiration) forming a hydrodynamic flow confinement in the open volume, adapted from [23]. b) when applying proper flow boundary conditions (i.e. sufficient aspiration) most probe heads of HFC-based liquid scanning probes allow to confine flow in the open volume, adapted from [24].

2.6 Conclusion and outlook

This chapter presents a tutorial on techniques for the hydrodynamic confinement of either bulk volumes of fluid or advected species in fully closed conduits, between parallel plates and in the open volume. Confining sample streams within sheath streams in closed microfluidic conduits has had great relevance since the early days of FACS. Over time, more sophisticated techniques were established, especially in the context of inertial flows and viscoelastic liquids. These advances have been shown useful e.g. for sized-based high-throughput sorting of entities, which would not be achievable with other methods of sorting or confinement.

Hydrodynamic confinements between parallel plates enable new approaches in the interaction with immersed biological interfaces and have been demonstrated in several relevant applications. Nonetheless, the variety of techniques available to form hydrodynamic confinements between parallel plates and especially in the open volume is far less compared to closed conduits. Even though relevant applications might not be obvious, we think it would be of interest to apply techniques from the realms of inertial and viscoelastic focusing to form confinements between parallel plates and in the open volume: advected species could e.g. be lined up in a flow confinement on a biological interface to perform interactions only along single lines, or to perform multiplexed interactions within a single larger flow confinement. In the open volume liquids of high refractive index could be confined in analogy to [71] to form spherical optical resonators for bio-sensing applications.

Chapter 3 Biopatterning with recirculation of hydrodynamically confined nanoliter volumes of reagents

The content of this chapter is based on the pre-print version of below listed research article, which was published in 2015 in *Analytical Chemistry* and featured on the cover of the corresponding issue and is reproduced here with minor modifications with permission from the American Chemical Society.

J. Autebert, J. F. Cors, D. P. Taylor, G. V. Kaigala. "Convection-enhanced biopatterning with recirculation of hydrodynamically confined nanoliter volumes of reagents." *Analytical chemistry*, **2015**, *88*(6), 3235-3242.

To this work, I contributed following aspects:

- Theoretical background and modelling (sections 3.3.1, 3.3.2 as well as 3.5.4 and 3.5.6)
- Experimental work pertaining to the validation of the predicted relative dilution γ (section 3.5.5)
- Creation of figures (I contributed content to figures 3, 4, 5, 6 and 8)
- Discussions on the concept and content of the paper with co-authors

3.1 Abstract

We present a new methodology for efficient and high-quality patterning of biological reagents for surface-based biological assays. The method relies on hydrodynamically confined nanoliter volumes of reagents to interact with the substrate at the micrometer-length scale. We study the interplay between diffusion, advection and surface chemistry, and present the design of a non-contact scanning microfluidic device to efficiently present reagents on surfaces. By leveraging convective flows, recirculation and mixing of a processing liquid, this device overcomes limitations of existing biopatterning approaches, such as passive diffusion of analytes, uncontrolled wetting and drying artefacts. We demonstrate the deposition of analytes, showing a 2- to 5-fold increase in deposition rate together with a 10-fold reduction in analyte consumption while ensuring less than 6% variation in pattern homogeneity on a standard biological substrate. In addition, we demonstrate the recirculation of a processing liquid using a microfluidic probe (MFP) in the context of a surface assay for (i) probing 12 independent areas with a single microliter of processing liquid, and (ii) processing a 2 mm² surface to create 170 antibody spots of 50 × 100 μm² area using 1.6 μL of liquid. We observe high pattern quality, conservative usage of reagents, micrometer precision of localization and convection-enhanced fast deposition. Such a device and method may facilitate quantitative biological assays and spur the development of the next generation of protein microarrays.

3.2 Introduction

Patterning and immobilization of chemicals, proteins or biomolecules on surfaces are central to surface biological assays [96]–[100] and have applications in cell-substrate studies, cell microenvironment modulation, chemical gradients on surfaces for motility assays, protein-protein interaction studies, creation of diverse libraries for drug screening and toxicology studies, screening of multiple biomarkers in point-of-care personalized medicine, for example. Established biopatterning methods locally deposit analytes using minute volumes (picoliter to microliter) of reagents and can broadly be classified into two categories. The first one uses inkjet technologies, where nanoliter volumes are spotted onto surfaces [101]–[103]. The second category requires a gentle contact between a pin and a substrate [104] to transfer a small volume of processing liquid onto a surface. Both approaches (Figure 3.1a) are widespread in research labs and industrial facilities as they enable high-throughput processing and precise (nm to μm accuracy) deposition [105], [106] of biochemicals. However, these approaches are limited by uncontrolled wetting and evaporation [107], which affect the homogeneity and repeatability of deposition [101], [108]. More generally, to abate evaporation, oil has been used as an immersion liquid [109], but in the context of biopatterning, the surface requires a rigorous wash step to remove the oil prior to downstream analytical tests. Such rinsing involves solvents and surfactants that will likely cause degradation of the patterned receptors. In contrast, several research groups developed microfluidic-based biopatterning techniques focusing on deposition quality [110] in which closed channels prevent evaporation. For example, Delamarche *et al.* developed microfluidic networks (MFN, Figure 3.1c) to deliver proteins to surfaces by placing and sealing elastomeric materials on the substrate [14], and a variant thereof, a stencil-based method [111] to spatially localize the processing liquid on surfaces (Figure 3.1b). These microfluidic methods resulted in high-quality biopatterns confined to specific areas on a surface, but suffered from either a large volume consumption or a low deposition rate. Moreover, MFNs are not compatible with high-density discrete unit patterns, such as microarrays, and any variations of the pattern would need a redesign of the network. Other examples of contact-based microfluidic implementations, such as chemistries [17], fountain pens [23], [112] and continuous-flow printing [16], also impose constraints on the type of surface and the ability to scan and are subject to cross-contamination as well. Non-contact implementations using electric fields, such as electrohydrodynamic jet printing [113] and scanning ion-conductance microscopy [19], demonstrated patterns in the hundreds of nm range with large inter- and intra-spot variations [114], but require conductive substrates.

Thus, versatile and high-quality patterning of biochemicals on surfaces remains elusive, but microfluidic implementations have paved the way towards convection-enhanced deposition. In general, continuous-flow methods (Figure 3.1 c to f) result in a reduction of the deposition time compared with diffusion-driven processes [115], but are very inefficient in terms of reagent consumption for two key reasons. First, continuous flow implies the use of larger volumes than in diffusion-based deposition, and second, the actual usage of analytes from the solution is very low. For example, a typical convection-based surface reaction in a 100- μm -deep channel would consume less than 1.5% of the sample flowing over the surface, resulting in tremendous waste of analytes. This inefficient reagent usage is problematic, particularly in biopatterning, where biochemicals such as antibodies and DNA probes are expensive. Circulating the processing liquid multiple times over the deposition zone (Figure 3.1d) provides a way to improve reagent utilization [116], [117]. In microchannels, however, laminar flows will hinder homogenization of the recirculated volume, and mixing would therefore be necessary to enable a more efficient usage of the processing liquid (Fig 1.e) [118], [119]. With this in mind, we envision six attributes for an ideal implementation of a versatile biopatterning device (Figure 3.1g): low reagent consumption, high deposition rate, efficient reagent usage, low variation in the spots deposited,

high throughput, and micrometer-scale precision in deposition. Such a device should leverage continuous flow deposition together with mixing and recirculation of the processing liquid (Figure 3.1f). On the one hand, this ideal implementation would retain the advantages of inkjet and pin-spotting devices, namely, low reagent consumption, high throughput and precise localization. On the other hand, processing of the surface with continuous flows would provide efficient use of analytes, reduced deposition time and homogeneity of the pattern deposited.

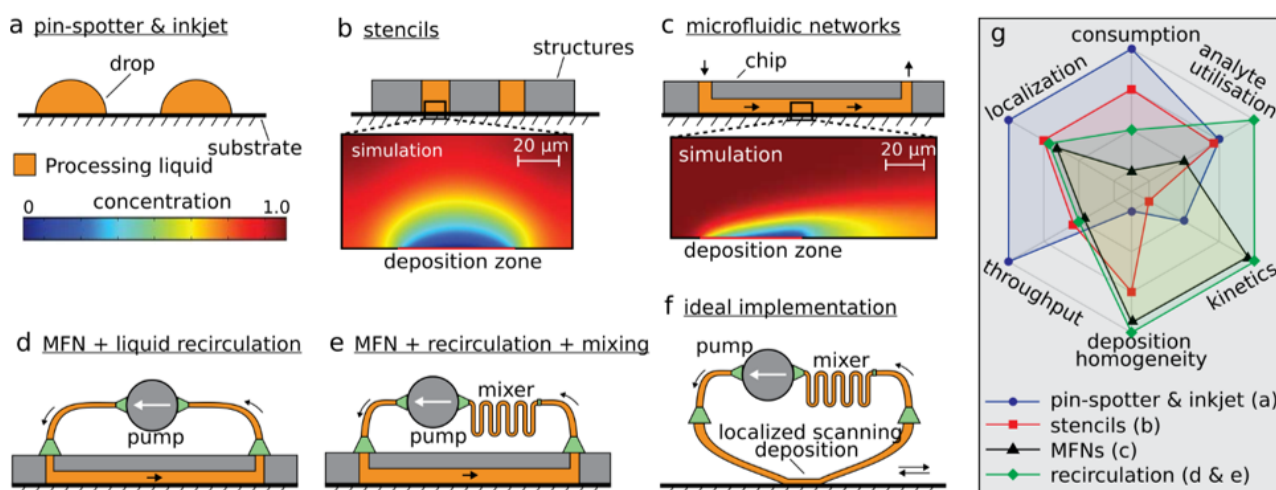


Figure 3.1: Overview of biopatterning methods. a) Pin-spotter and inkjet deposit small volumes of processing liquid on substrates. b) Stencils use structures that are physically placed on a substrate to localize the processing liquid with micrometer precision. The simulation shows the diffusion profile above the deposition zone. c) Microfluidic networks (MFN) use convection-enhanced deposition to decrease deposition time and a microchannel for spatial localization. The simulation illustrates the diffusion profile along the flow path. d) Using a pump to recirculate the processing liquid enables a more efficient usage of the processing liquid. e) Mixing of the recirculated liquid is important to increase usage efficiency in microfluidics, where flows typically are laminar. f) The ideal implementation of biopatterning takes advantage of convection-enhanced deposition, high-resolution scanning, recirculation and mixing while ensuring a localized, non-contact deposition. g) Empirical graph highlighting six important attributes of biopatterning methods.

In this paper, we report a scanning, non-contact microfluidic device for high-quality, versatile biopatterning. This approach makes use of a vertically-oriented microfluidic probe (MFP) [25], [26] to confine nanoliter volumes of processing liquid on top of a substrate in a wet environment, ensuring non-contact operation and convection-enhanced deposition. MFPs belong to a class of devices termed “open-space microfluidics” that relies on hydrodynamic flow confinement (HFC) of the liquid [7]. Here, we leveraged hierarchical HFC [120] to dilute the aspirated processing liquid minimally, and show that biochemicals can be efficiently recirculated back and forth on a surface. We developed analytical models to investigate diffusion, advection and surface reactions in the context of HFC and, with this, defined the MFP operational parameters for efficient biopatterning (see Figure 3.7). We demonstrate the deposition of analytes in the context of the deposition and detection of IgG, showing a 2- to 5-fold increase in deposition rate together with a 10-fold reduction in analyte consumption while ensuring less than 6% variation in pattern homogeneity on a standard biological substrate. IgG antibodies are macromolecules of about 150 kDa and play a key role in the immune system as they react with receptors present on the surfaces of macrophages, neutrophils and natural killer cells. They are used as a diagnostic marker for several autoimmune diseases and as a measure of the immune response to pathogens, for example, the serologic immunity to measure measles, mumps, rubella, hepatitis B, varicella. IgGs extracted from donated plasma are also used in therapy to treat immune deficiencies, autoimmune disorders and infections [121].

In addition, we demonstrate recirculation of a processing liquid using the MFP in the context of a surface assay: (i) for probing 12 independent areas with a single microliter of processing liquid, which is relevant when multiple assays have to be performed with a limited volume budget, and (ii) for processing a 2 mm² surface to create 170 antibody spots of 50 × 100 μm² area using 1.6 μL of liquid.

3.3 Efficient bio-patterning using the MFP

For efficient usage of the processing liquid, we circulate this liquid back and forth while ensuring homogenization through mixing in the serpentine channels of the MFP head [119]. The implementation of this circulation in the device has two states, in which the direction of flow is different. In state 1, the liquid is injected via the two apertures on the right and aspirated through the two apertures on the left (see Figure 3.2a). After switching to state 2, all flow directions of the liquids are inverted.

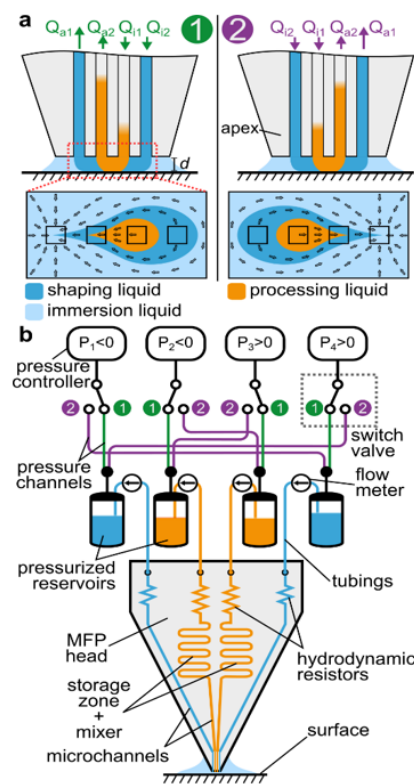


Figure 3.2: Scheme for liquid recirculation using pressure switching. a) A hierarchical flow confinement is generated in state 1 to ensure minimal dilution of the processing liquid. When switching the valves to state 2, the direction of the flows is reversed. b) Scheme of low-dead-volume pressure switching for liquid recirculation.

Such liquid switching would typically be performed with 2-position valves, but they generally have a large dead volume (tens of microliters) and involve a displacement of the liquid that would disrupt the HFC temporarily. To address these two important issues, we developed a low-dead-volume fluidic system in which the liquid reservoirs are placed close to the MFP head (see Figure 3.2b). We used the valves to redirect positive and negative pressures towards the appropriate reservoirs. The advantages of using valves to switch pressure instead of liquids are: (i) the absence of liquid displacement in the HFC when switching; (ii) valves can be placed away from the microfluidic system without increasing dead volumes, and (iii) switching is fast (within few milliseconds), with the pressure stabilizing within 1 s. Flow rates are generated using external

pressure controllers and hydrodynamic resistors (see Figure 3.2) integrated in the MFP head and monitored in real-time.

3.3.1 Diffusive transport between two laminar flows within the HFC

In a single HFC, dilution of the processing liquid is driven primarily by its aspiration together with the surrounding liquid. In the hierarchical HFC, because $Q_{i1} = |Q_{a2}|$, the dilution of the processing liquid is strongly reduced. There are three main loss-mechanisms contributing to the dilution of the processing liquid: 1) diffusion of analytes from the processing liquid to the shaping liquid, 2) dilution due to mismatched injection and aspiration flow rates in the inner confinement, and, 3) dilution in the Taylor-dispersed interface between the recirculated volume and other liquid filling the remainder channels. As the deviation between the desired and the actual occurring flow rates can be minimized by means of choosing appropriate hardware and flow regimes, and Taylor dispersion could be suppressed using oil droplets to separate the recirculated volume from other liquid in the channel, diffusive losses remain the only fundamental loss channel, which cannot be avoided. We therefore in the following discussion focus on the analysis of diffusive losses.

For efficient recirculation of the processing liquid, this loss of analyte should be minimized. We developed a model to investigate the dilution γ of the processing liquid as a function of two key parameters, namely, the apex-to-surface distance d and the flow rate of the processing liquid Q_{i1} (see Figure 3.3 a and b).

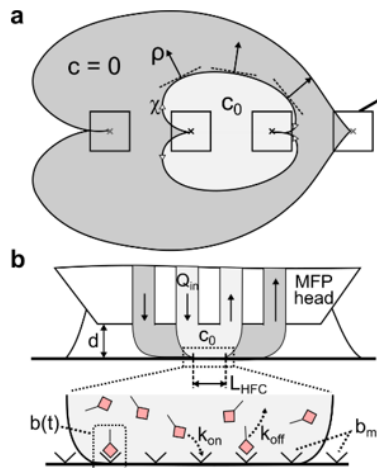


Figure 3.3: Scheme for analytical model of analyte transport in a hierarchical HFC. a) Bottom view of a hierarchical HFC with corresponding coordinate system. b) Schematic side view of a hierarchical HFC.

The apex of the MFP head and the surface to be processed are considered as two parallel surfaces, with an apex-to-surface distance ranging from $10\ \mu\text{m}$ to $50\ \mu\text{m}$. Given these boundary conditions, we apply the Hele-Shaw approximation and model the liquid flow between apex and surface as a potential flow (see S3). Each of the four apertures creates a static, radial velocity field of liquid flow. The resulting velocity field represents the superimposition of the radial velocity fields from the individual apertures. Because the resulting velocity field is symmetric, transport across the interface can be described by considering only one-half of the interface. We define a curvilinear coordinate system, with χ the coordinate axis tangential to the interface and ρ the coordinate axis perpendicular to the interface (see Fig 3.a). The analyte in the processing liquid has a diffusion coefficient D , and the initial analyte concentrations are c_0 and $c = 0$ for the processing liquid and the shaping liquid, respectively. The initial concentration profile $c(\chi = 0, \rho)$ across the interface can thus be approximated with a Heaviside step function.

The dilution γ is expressed as the ratio of the rate with which analytes diffuse from the processing liquid into the shaping liquid to the total rate of analytes transported through the confined liquids:

$$\gamma = \frac{\frac{\partial n_D}{\partial t}}{\frac{\partial n_{in}}{\partial t}} = \frac{2d}{Q_{i1}} \int_0^{x_{\max}} \sqrt{\frac{D \cdot \hat{v}_x}{4\pi \cdot u}} du \quad (3.1)$$

Theoretical values for γ and the development of equations are presented and compared with experimental dilution values in section 3.5.4. According to both analytical and experimental dilution values, efficient recirculation is favored at higher flow rates and when the head is in proximity of the surface. We note however that the flow rate will influence the amount of processing liquid used per circulation cycle.

This implies that for a finite volume of processing liquid, there is a trade-off between the flow rate of the processing liquid and the number of circulation cycles per minute. Depending on the application, parameters such as apex-to-surface distance and flow rates need to be adjusted to ensure proper surface processing and minimal loss of processing liquid.

3.3.2 Convective transport and deposition of analytes on a surface

This model describes a metric $\varepsilon(t)$ that quantifies the benefit of convective transport as compared to diffusion-driven transport for surface biopatterning. While it is clearly established [115] that convection will enhance the deposition rate, this gain largely depends on the working regime and parameters such as analyte concentration in the processing liquid, flow rates and surface processing duration. We developed an analytical model that describes convection-enhanced deposition of analytes on a surface using the hierarchical HFC. This model accounts for the transport of IgG molecules from the HFC to the surface and for the kinetics of the reaction between analytes and receptors on the surface.

We investigate the deposition of an analyte with a diffusion coefficient D_A and a concentration c_0 on a surface presenting binding sites with a surface density b_m . Binding of analytes is assumed to follow first-order Langmuir kinetics and can therefore be characterized with the association and dissociation constants k_{on} and k_{off} . Because of the binding of analytes to receptors on the surface, the concentration of analytes in the processing liquid directly above the surface reduces, and a depletion zone is formed. Despite strong advective transport, analytes can travel across the depletion zone only by means of diffusion. For operation of the MFP, this depletion zone is steady and on the order of a tenth of a micrometer, which is small relative to the apex-to-surface distance and to the HFC footprint, which is typically $50 \times 100 \mu\text{m}^2$. We apply models for transport through a thin depletion zone and first-order binding of analytes to a surface as summarized by Squires *et al.* [115]. Central to this analysis is a Damköhler number Da defined as the ratio of the rate of reaction at the surface to the rate of convective transport of analytes.

$$Da = \frac{c_0 \cdot k_{on} \cdot b_m}{N \cdot \mathcal{F} \cdot D} \quad (3.2)$$

In (2), N is Avogadro's number and \mathcal{F} is the non-dimensionalized flux of analytes through the depletion zone [122]. For MFP-based deposition of an IgG, the binding of analytes to the surface is neither transport nor reaction limited, because Da is in the range of 1 (see section 3.5.6). The ratio $\varepsilon(t)$ of analyte bound with the MFP to that of pipette deposition can be evaluated as (see section 3.5.6)

$$\varepsilon(t) = \frac{\left(1 - e^{-\frac{k_{\text{on}}c_0 + k_{\text{off}}}{Da} \cdot t}\right)}{\left(1 - e^{-\frac{(k_{\text{on}}c_0 + k_{\text{off}}) \cdot 40D_{\text{Ig}} \cdot N}{k_{\text{on}}b_m L_{\text{HFC}} \cdot \sqrt{t}}}\right)} \quad (3.3)$$

Here $\varepsilon(t)$ expresses the ratio of MFP-deposited IgG to pipette-deposited IgG as a function of time. This metric quantifies the benefit of convective transport when compared with diffusion-driven surface patterning. Figure 1.2Figure 3.4a shows $\varepsilon(t)$ for four concentrations of IgG in the processing liquid, with standard parameters for MFP surface processing. The graph suggests that deposition using the MFP is more efficient for times shorter than 10 min and strongly depends on the analyte concentration. Once saturation of the surface with the MFP has been reached, the pipette deposition efficiency will slowly converge to the MFP-based deposition efficiency, thus $\varepsilon(t)$ converges to 1. Interestingly, the lower the concentration, the better the MFP will perform in comparison to pipette deposition, which implies that convective deposition is particularly favorable for low concentrations. As an example, for a concentration of 50 $\mu\text{g}/\text{mL}$, the amount of analyte deposited with the MFP after 40 s will be 1.5-fold higher than with pipette deposition. Longer deposition times will result in identical deposition efficiencies for both approaches after 6 min. In contrast, for a 10-fold lower concentration (5 $\mu\text{g}/\text{mL}$), the number of analytes deposited with the MFP after 5 min will be 3.5-fold higher than with pipette deposition. The pipette deposition will require more than an hour to reach the MFP-based deposition efficiency. This analysis clearly highlights the advantage of using MFP deposition for low concentrations of analyte, and that there is an optimal range of processing durations in which the MFP is particularly relevant.

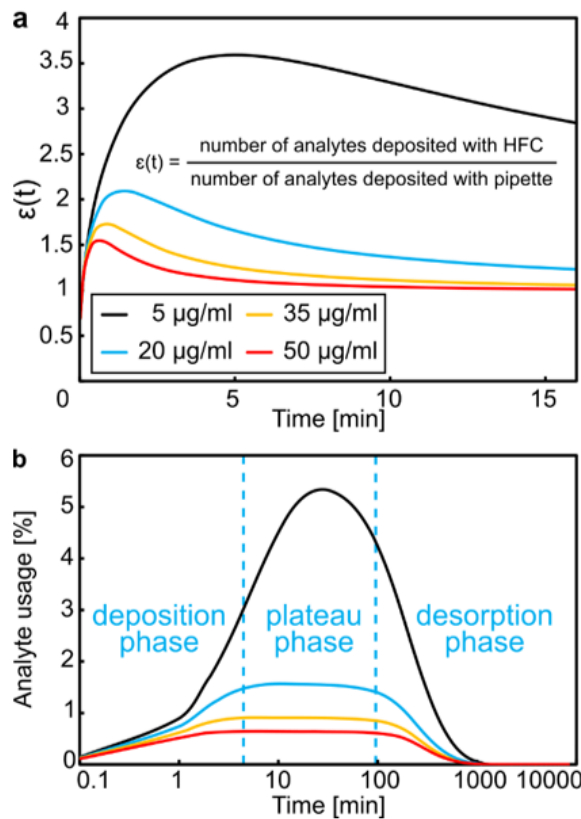


Figure 3.4: Deposition efficiency using the MFP with different concentration of reagents. a) Ratio of deposited analytes with the MFP compared with pipette-based

deposition for concentrations of 5, 20, 35 and 50 $\mu\text{g}/\text{mL}$. b) Ratio of analytes deposited over the total amount of analytes in the processing volume. Both values were calculated numerically for four concentrations of an IgG molecule.

From this model, we also derived the analyte usage as a function of time (see Figure 3.4b), which corresponds to the ratio of analytes bound to the surface to the initial number of analytes in the processing liquid. Consequently, analyte usage is first marked by a strong increase in the number of bound analytes, and we term this the deposition regime. The decrease of available free binding sites on the surface over time leads to a reduction of the association rate, and analyte usage enters a plateau regime when the association rate and the dissociation rate balance each other. Through successive dilution of the processing liquid in every circulation cycle, the concentration of analytes decreases to the extent that dissociation of analytes from the surface becomes predominant in the desorption regime. The model allows us to estimate the number of recirculation cycles (or time) after which the processing liquid is depleted because of deposition on the surface and diffusive transport to the outer flow confinement. The processing liquid can then be replenished before entering the “desorption phase”, thus preventing deposition issues. Figure 3.4b further implies that analyte usage depends on the initial concentration and remains below 6% for the four concentrations investigated. An important implication of this result is that a unit volume of processing liquid can be circulated multiple times for multi-spot deposition or for long incubation times.

3.3.3 Results and discussion

To implement an MFP-based antibody/antigen assay, we used a standard polystyrene Petri dish as substrate. After incubation of IgG, we processed the surface with the MFP using a solution of fluorescently labelled anti-IgG for different durations with a constant flow rate (1 $\mu\text{L}/\text{min}$) and an apex-to-surface distance $d = 30 \mu\text{m}$. The results of these assays ($n = 5$ experiments per deposition time) are presented in Figure 3.5. The experiments were performed both with and without recirculation of the processing liquid, along with a reference experiment using pipette deposition. The fluorescence intensity of deposited anti-IgG was used to assess the deposition efficiency and quality. Deposition using the MFP (Figure 3.5, black squares and red dots) showed a higher efficiency than pipette deposition (Figure 3.5, blue diamonds).

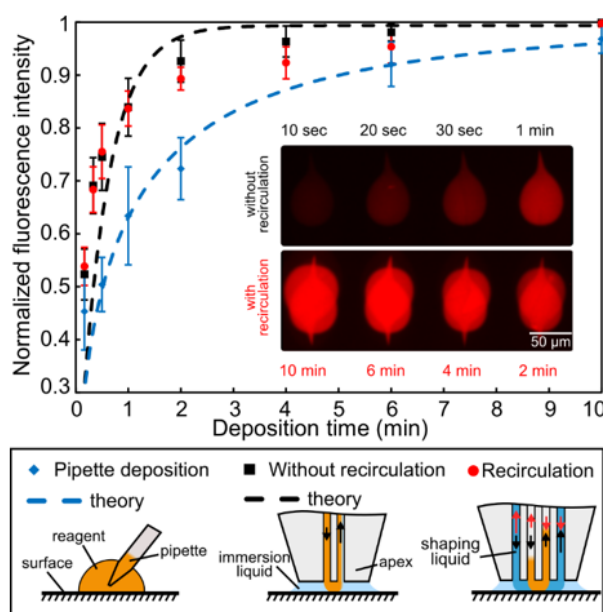


Figure 3.5: Deposition of goat anti-IgG on IgG-coated polystyrene surface. Normalized fluorescence intensity of deposited anti-IgG ($n = 5$) and corresponding trends from the analytical model (theory). Error bars represent the standard

deviation for five experiments. The fluorescence intensity is measured in the center ($5\ \mu\text{m} \times 5\ \mu\text{m}$) of the teardrop-shaped HFC footprint.

With an antigen concentration of $50\ \mu\text{g}/\text{mL}$, we saturated the surface in less than three minutes with the MFP and in six minutes with the pipette. Interestingly, we observed no significant difference between deposition with and without recirculation, as both methods use convection-enhanced deposition. However, the model for convective deposition predicts saturation to occur faster than what we observed in the experiments. We hypothesize that these discrepancies arise from: (i) three-dimensional effects that are not accounted for in the model, resulting in a reduction of the effective flow velocity and therefore a reduction of advective transport to the surface, and (ii) the fact that k_{on} , k_{off} and the binding sites surface density b_m were derived from the diffusion-driven deposition experiments (see Figure 3.5, blue line and symbols) and may be different for the MFP-based deposition experiments. A striking example of the benefits of recirculation using the MFP is that the total volume used after 10 min with recirculation ($1\ \mu\text{L}$) was one order of magnitude lower than without recirculation ($10\ \mu\text{L}$), while reaching an identical density of captured antigens. Ultimately, this approach would lead to either a drastic reduction of antigens needed for the assay or, conversely, a reduction of the assay time if a pre-concentration of the analyte is done prior to recirculation. Moreover, when using recirculation, the total volume of analyte needed is largely independent of the reaction duration. This result is particularly relevant in the case of low-concentration analytes, where the reaction time can be in the range of hours. Recirculation therefore enables enhanced kinetics as the result of convection, while improving reagent usage through multiple circulations of the same volume.

Most biopatterning applications require deposition on multiple zones with high spatial resolution, typically in the micrometer range. A key advantage of the MFP is its capacity to interact locally with a surface and to scan large areas rapidly [123]. Leveraging this capacity, we investigated the recirculation of a given volume of liquid on multiple positions on a substrate. Multi-zones deposition can be used for localized capture of antigens from a sample, and using a single microliter, recirculation allows multiple independent capture zones to be probed. Similarly, an unknown concentration of antigen can be recirculated for different lengths of times on multiple areas on an antibody-coated surface. This can be leveraged to determine the adequate deposition time on the surface to prevent over- and under-exposure of the sample of interest in the capture zone. We demonstrated these two aspects by recirculating different concentrations of a fluorescently labeled IgG on an anti-IgG-coated surface (see Figure 3.6a) and checked the deposition density after different deposition times (see Figure 3.6b).

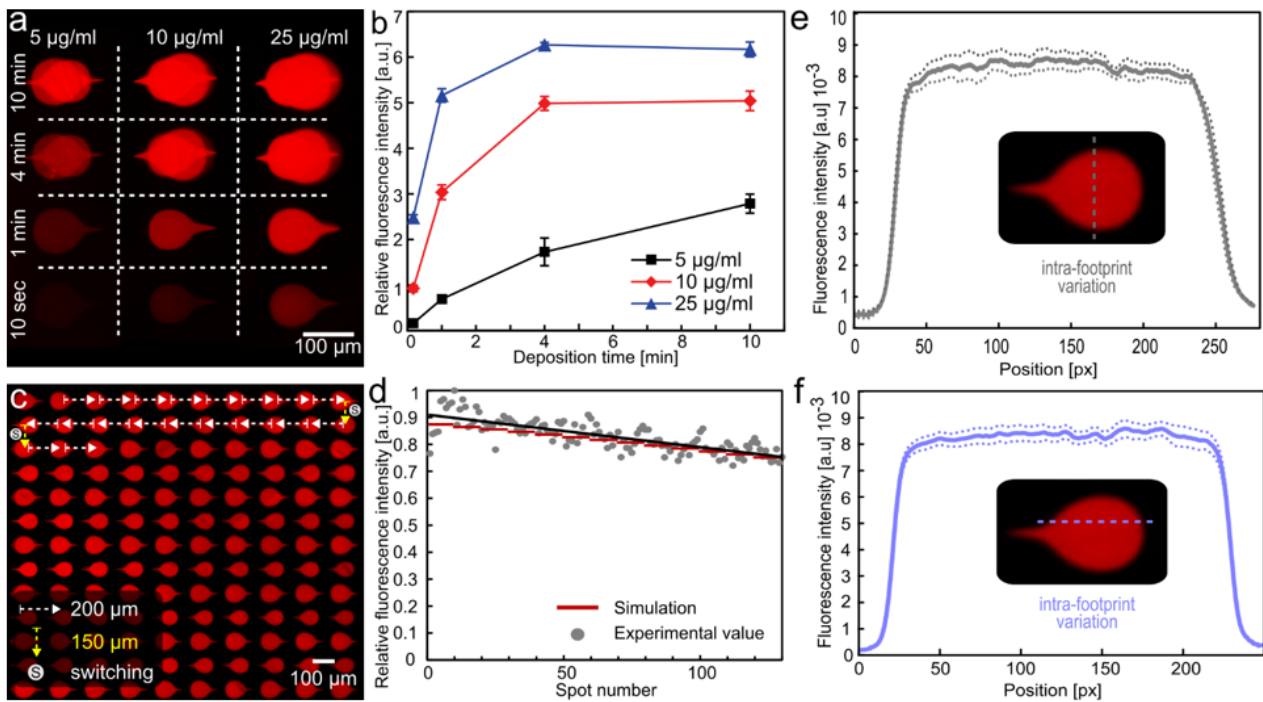


Figure 3.6: Multispot deposition of goat anti-IgG using recirculation with the MFP. a) Image of the deposition of anti-IgG solution using $1.6 \mu\text{l}$ with concentrations of 5, 10 and $25 \mu\text{g/ml}$ and incubation times of 10 s, 1, 4, and 10 min. b) Fluorescence intensity of zones shown in a). c) Photograph of 130 spots deposited with $1 \mu\text{l}$ of solution (170 spots in total). The flow direction was switched every ten spots. d) Average fluorescence intensity measured on each spot compared with the predictions of our models. (e and f) Intra-footprint variation within one spot ($< 6\%$ variation).

These results indicate that an adequate deposition time (signal intensity detectable and no saturation) for the highest concentration was obtained in under 1 min, whereas the lowest one would require 10 min to yield a signal sufficient for analysis. This use of recirculation is a unique implementation of a “reverse assay” in which the sample is processed successively on multiple zones. These independent zones may contain different capture antibodies, giving access to multiple assays with a minimal volume, or, for a single antibody, enable better control of the capture density and, ultimately, quantification of antigens concentration through multiple deposition durations.

We also investigated the possibility of using a limited and small volume of processing liquid in the MFP head to deposit a large number of spots on the surface. We deposited 170 spots (see Figure 3.6c), switching the flow direction every ten spots, with the probe staying 10 s on top of each spot. Working close to the surface ($10 \mu\text{m}$), we limited the dilution to the extent that only a minimal decrease in fluorescence was observed between the first and the last spot (Figure 3.6d). This decrease in fluorescence was predicted by combining the two analytical models describing dilution during recirculation and binding to the surface. The models exhibited very good correlation with the experimental values. $1.66 \mu\text{l}$ of fluorescently labeled IgG were used to perform deposition of these 170 spots, so each spot corresponds to a “used” volume of 9.7 nL .

Finally, we investigated the quality of the spots deposited and found intra- and inter-footprint variations of 5.8% and 3.4% , respectively (see Figure 3.6 e and f), confirming the advantages of “wet” methods for presenting an antibody to a surface in terms of deposition quality. We hypothesize these relatively small deposition variations to be due to the type of substrate used (standard, untreated polystyrene Petri dish) and that the deposition quality could be further increased by using engineered substrates.

3.4 Conclusion

We described, characterized and validated a new method for surface processing and biopatterning. This method exploits the hierarchical implementation of the HFC to efficiently present micro- to nanoliter volumes of analytes on surfaces. The analytical models we present provide guidelines on minimizing the dilution of the processing liquid and enhancing the deposition kinetics by controlling parameters such as the apex-to-surface distance, the flow rates and the deposition time. This enables the rapid processing of areas ranging from $5 \times 5 \mu\text{m}^2$ to $1 \times 1 \text{cm}^2$ in large substrates, such as Petri dishes and glass slides, with volumes in the microliter range. As an example, we deposited 170 antibody-antigen spots with a per-spot volume of 9.7 nL and with a variation in deposition homogeneity below 6%. In comparison, state-of-the-art inkjet tools would require a comparable volume per spot, but achieve limited deposition homogeneity. Importantly, the high quality of the patterns deposited with our method is compatible with the needs of quantitative surface assays. Experiments comparing the deposition efficiency showed a 3-fold improvement of the deposition speed and a 10-fold decrease of the total volume needed for a surface assay when using convection-enhanced deposition and liquid recirculation in the MFP. Such outcomes are particularly relevant in the case of expensive biochemicals or when the concentration of analytes is so low that it would impede deposition efficiency. In addition, we demonstrated that this tool can probe multiple capture areas independently with a single limited volume of a biological (clinical) sample.

For efficient biopatterning, we leveraged the strengths of the MFP and the underlying physics of HFC. First, the hydrodynamic confinement of the processing liquid with the MFP eliminates the need for microfluidic networks and channels or multiphase systems for localization and compartmentalization. The MFP provides a dynamic and highly versatile means of localizing and presenting the processing liquid on a surface immersed in an aqueous environment. This method is compatible with Petri dishes, glass slides as well as more challenging substrates with varying topologies, such as cell cultures and tissues sections. Second, this method can be scaled to form larger or smaller footprints by changing the aperture size, aperture spacing and flow rates with dimensions ranging from hundreds of nanometers to a few millimeters. The scanning capability of the probe [123] allows the patterning on large surfaces, typically in the centimeter range, with the possibility of creating arrays of up to 30,000 spots/ cm^2 with a spot size of $10 \times 10 \mu\text{m}^2$. Third, the capacity of the MFP to rapidly switch liquids [124] on top of the substrate makes it a relevant tool for implementing complex biochemistries requiring multiple consecutive chemicals to be dispensed on the surface, or even for manufacturing protein microarrays.

A current limitation of the device is its throughput. In this paper, a single spot is patterned at a given time, but we foresee processing multiple positions on the surface in parallel by leveraging standard microfluidic channel bifurcations implemented on the probe. We believe that the MFP might not be the preferred tool when the incubation or reaction time is in the range of tens of hours. However, as discussed in this paper, most surface chemistries will be accelerated by convective transport, and thus long overnight incubation will likely not be required. For specific applications, increasing the recirculated volume is readily feasible, but working with processing liquid volumes below 100 nL is challenging to implement in the current probe configuration. However, we believe that the microliter to milliliter range is appropriate for most biopatterning applications, as it is compatible with standard volumes used in industrial methods, such as inkjets and pin-spotters. Finally, the asymmetric teardrop shape of the deposition area can be altered by using different aperture spacings and geometries. The method presented in this paper combines five of the six attributes of an ideal biopatterning approach, namely, low reagent consumption, high deposition rate (kinetics), efficient reagent usage, low variation in the spots deposited, and micrometer-scale precision in deposition. We

strongly believe that this combination of advantages creates a powerful tool for an efficient and high-quality patterning of receptors on surfaces and thus will enable quantitative assays in discovery research, point-of-care devices, large-scale surface patterning and reverse immunoassays, and will catalyze the manufacturing of protein microarrays. This method will be a unique facilitator in quantitative biology and precision diagnostics.

3.5 Materials and Methods

3.5.1 Experimental section

Microfluidic probe platform. The MFP platform consists of three linear stages (Lang GmbH, Hüttenberg, Germany) for the positioning of the head relative to the surface. The sample is placed on a custom arm of the stages that is placed above an inverted microscope (Eclipse TI-E, Nikon, Japan). The head can be positioned on the surface with an accuracy of 100 nm. Images were acquired using an ORCA-Flash 4.0 camera (Hamamatsu Photonics K.K., Hamamatsu, Japan) and using LED lamp illumination (Sola, Lumencore Inc., Beaverton, OR). The MFP head is mounted on a holder vertical to the microscope objective, and aligned to the surface using manual rotation stages. A detailed description of the set-up, alignment procedure and standard operation of the MFP head can be found elsewhere [120].

Set-up to implement liquid recirculation. Four independent reservoirs were connected to the MFP head using 1/16 PEEK tubing (IDEX H&S, Oak Harbor, WA) and linear connectors (Dolomite Microfluidics, Charlestown, MA). The reservoirs were pressurized using pressure control devices (MFCS, Fluigent, Paris, France) with a working range of ± 200 mbar per channel. Pressure was switched in the four reservoirs simultaneously using two-way switch valves (2-switch, Fluigent, Paris, France). Pressures would typically stabilize within hundreds of milliseconds, resulting in the stabilization of the flow confinement within one second. Flow rates were measured using flow sensors (Fluigent, Paris, France). Hydrodynamic resistances in the MFP head were designed to provide a suitable working range of pressures to generate the flows.

MFP head microfabrication. The MFP head is a microfabricated silicon-glass device. The head comprises four apertures, hydrodynamic resistors, and two storage and mixing zones of 1 μL volume for circulation of the processing liquid. Channels ($50 \times 50 \mu\text{m}$) in silicon were defined photolithographically and etched using deep reactive-ion etching (DRIE). Subsequently, they were sealed by anodic bonding (1.3 kV, 475° C) with glass. The fabrication process has been described in detail elsewhere [26].

Measuring the concentration of processing liquid. We used a solution of 50 μM Rhodamine B as the reference for concentration measurements. The fluorescence intensity of the flow confinement was acquired using a camera. We measured the average fluorescence value on a region of interest (ROI). To obtain the relative drop in concentration after each circulation cycle, the same ROI was used to measure the fluorescence of the confined solution. For measurements requiring precise apex-to-surface distance control, we performed a z-axis reference to zero height prior to each experiment.

Rabbit IgG antibody-antigen assay. A test surface was prepared starting with a clean polystyrene Petri dish that was incubated 30 min at room temperature with 100 μL of a 50 $\mu\text{g}/\text{mL}$ rabbit IgG solution (Sigma-Aldrich, Saint Louis, MO). After three rinsing steps (PBS + Tween-20 0.05, PBS, and DI water), the surface was blocked for 30 min with BSA (1% in PBS) and rinsed. Fluorescently labelled rabbit anti-IgG was deposited on the surface with the MFP for different deposition times.

Automated deposition of antigens on a surface with the MFP. After priming the fluidic tubing with the appropriate solutions (fluorescent anti-IgG in the inner injection, PBS everywhere else), a Matlab script was used for automating the sequential surface processing steps: stage movement for precise spotting, and valve switching for recirculation and pressure control. Pressure controllers and switch valves were controlled by the manufacturer's API, and the stages with a standard serial protocol.

FEM modelling. Steady-state 2D transport simulations were performed using COMSOL Multiphysics version 4.2. We used incompressible fluids, open boundaries, and nonslip conditions on surfaces as parameters. The model couples the solution of the Navier–Stokes equation and the convection-diffusion equations. All liquids were chosen to be water (incompressible Newtonian fluid with a density of 998 kg/m^3 and a dynamic viscosity of $0.001 \text{ N}\cdot\text{s/m}^2$). The diffusion constant of the analyte was set to $D = 3.8 \times 10^{-7} \text{ cm}^2/\text{s}$, which corresponds to the diffusion constant of an IgG molecule.

Image analysis. Time-lapse images were analyzed using ImageJ and NIS Elements Basic Research software suite (Nikon). Scale bars were calculated from bright-field images. To account for a potentially uneven illumination pattern, each image was divided by a control image taken on an empty zone of the slide. After removal of the background, the processed image was used to calculate the fluorescence intensity.

Statistical analysis. Error bars represent the standard deviation. If no error bars are visible, the standard deviation is smaller than the symbol representing the mean value. ' n ' refers to the number of data points unless specified otherwise.

3.5.2 Analyte consumption in a microchannel.

We consider deposition of immunoglobulin (IgG) on a deposition zone with a length of $100 \text{ }\mu\text{m}$ within a $100 \text{ }\mu\text{m}$ deep channel and a flow rate of $1 \text{ }\mu\text{l}/\text{min}$. IgGs in solution that flow over the deposition zone can find a binding partner within the deposition zone. This leads to formation of a depletion zone that extends to about $1.5 \text{ }\mu\text{m}$ (based on Squires *et al.* [115]) of the $100 \text{ }\mu\text{m}$ deep channel. All IgGs flowing through the remaining $98.5 \text{ }\mu\text{m}$ of the channel depth are not available for the binding reaction at the surface and thus the overall usage of available analytes is well below 1.5%.

3.5.3 Operation of the microfabricated MFP head for liquid recirculation.

We fabricated a glass/silicon head comprising hydrodynamic resistors, storage and mixing zones and fluidic vias for connection to the reservoirs (see Figure 3.7). We used a hierarchical flow confinement, with the flow rates following three rules: both injections are identical, $Q_{i1} = Q_{i2}$; total aspiration is sufficiently high to ensure a stable HFC, $|Q_{a1} + Q_{a2}| = 3(Q_{i1} + Q_{i2})$; and dilution must be minimal, $Q_{i1} = |Q_{a2}|$. We observed a stable and well defined HFC (Figure 3.7b, state 1). Upon switching the four pressures in the reservoirs, we observed a rapid ($< 1 \text{ s}$) establishment of the HFC with reversed flow direction (see Figure 3.7b, state 2).

Two serpentine zones, of $1 \text{ }\mu\text{l}$ volume each, ensure in-head storage and homogenization of the processing liquid (see Figure 3.7a). Further reduction of this volume is feasible to the extent that the total volume of the recirculated liquid must be large compared to the fraction of processing liquid lost to the outer aspiration during switching, typically below 1 nl per cycle at a flow rate of $1 \text{ }\mu\text{l}/\text{min}$.

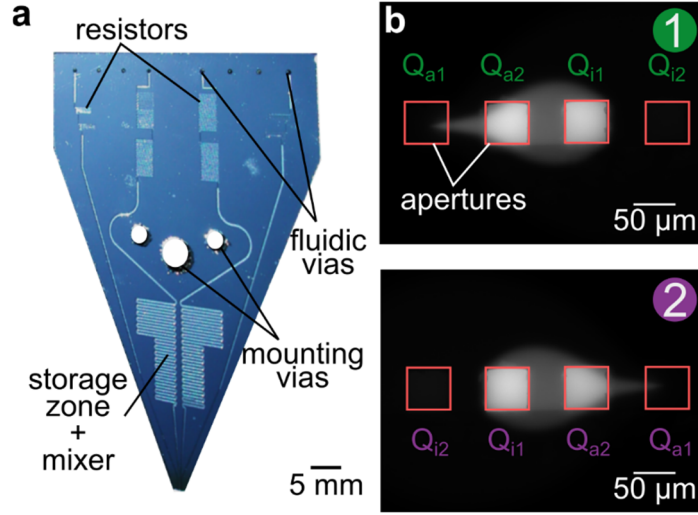


Figure 3.7: Microfabricated MFP head generating a hydrodynamic flow confinement. a) MFP head with hydrodynamic resistors, two $1 \mu\text{l}$ storage zones, two mixers, fluidic vias, and mounting vias. b) Micrographs of a hydrodynamic flow confinement between the apex and the surface ($d = 30 \mu\text{m}$). Switching from state 1 to state 2 occurs within 1 s.

3.5.4 Diffusive transport between two laminar flows within the HFC.

For the evaluation of the velocity vector field between apex and surface, we assume that the fluid flow from and to the apertures of the MFP head can be described with the Hele-Shaw approximation. The apex-to-surface distance d is in the order of $10 \mu\text{m}$, while the lateral dimension of the apex is in the range of 1 mm . Movement of liquid perpendicular to the apex is therefore significant up to a distance of approximately $10 \mu\text{m}$ from each aperture. In this model, we neglect any movement of liquid perpendicular to the apex and do a far field analysis by considering the apertures as line sources, stretching between the apex of the MFP and the surface.

Each source individually produces a radial field of liquid flow and is assumed as the center of a cylindrical coordinate system. The velocity vector field $\vec{u}(r, z)$ of liquid flow depends on the distance from the source r and the vertical position z between the apex and the surface. The surface is at $z = 0$, while the apex is at $z = d$. The net flow through a cylindrical boundary around the source has to equal the flow Q_s effected by the source:

$$Q_s = \int_0^h \int_0^{2\pi} \vec{u}(r, z) \cdot r d\theta dz \quad (3.4)$$

Integration and solving for the velocity vector field $\vec{u}(r, z)$ for the respective source leads to:

$$\vec{u}(\vec{r}, z) = \frac{3Q_s}{\pi h^3 |\vec{r}|} \cdot z(d - z) \vec{e}_r \quad (3.5)$$

The magnitude of velocity varies in z -direction according to the classic parabolic flow profile. We therefore reduce the problem to two dimensions by averaging the velocity in the z -direction:

$$\langle \vec{u} \rangle(\vec{r}) = \frac{1}{h} \int_0^h \frac{3Q_s}{\pi d^3 r} \cdot z(d - z) \vec{e}_r dz = \frac{Q_s}{2\pi d |\vec{r}|} \vec{e}_r \quad (3.6)$$

By shifting sources to positions \vec{r}_i and superimposing their respective averaged velocity vector fields, the resulting velocity vector field $\vec{U}(\vec{r})$ for any arbitrary combination of sources can be evaluated as:

$$\vec{U}(\vec{r}) = \sum_{i=1}^n \frac{Q_{s,i} \cdot (\vec{r} - \vec{r}_i)}{2\pi d \cdot |\vec{r} - \vec{r}_i|^2} \quad (3.7)$$

The vector field $\vec{U}(\vec{r})$ contains the 2D information of liquid flow paths in the entire domain between the apex and the surface. The geometrical properties of potentially resulting HFC, such as size, shape and footprint area can be evaluated on the basis of this vector field.

In a single HFC, dilution of the processing liquid is driven primarily by its aspiration together with the surrounding liquid. In the hierarchical HFC, since $Q_{i1} = |Q_{a2}|$ dilution is solely due to diffusion of analytes from the processing liquid to the shaping liquid and is therefore limited. For efficient recirculation of the processing liquid, this loss of analytes should however be minimized. We developed a model to investigate the dilution γ of the processing liquid as a function of two key parameters, namely the apex-to-surface distance d and the flow rate of the processing liquid Q_{i1} .

We apply the advection-diffusion equation to study the transport of analytes. Here, v_χ and v_ρ denote the tangential and perpendicular components of the flow velocity.

$$\frac{\partial c}{\partial t} + v_\chi \frac{\partial c}{\partial \chi} + v_\rho \frac{\partial c}{\partial \rho} = D \cdot \left(\frac{\partial^2 c}{\partial \chi^2} + \frac{\partial^2 c}{\partial \rho^2} \right) \quad (3.8)$$

The velocity field of liquid flow between the apex and the surface as well as the boundary conditions for concentration are static, therefore above equation can be analyzed in steady-state. As $v_\rho = 0$ and $\frac{\partial^2 c}{\partial \rho^2} \gg \frac{\partial^2 c}{\partial \chi^2}$ equation (3.7 becomes:

$$\frac{\partial c}{\partial \chi} = \frac{D}{\hat{v}_\chi} \cdot \frac{\partial^2 c}{\partial \rho^2} \quad (3.9)$$

where $\hat{v}_\chi = \frac{1}{\chi} \int_0^\chi \hat{v}(u) du$ is the average tangential velocity along the interface up to a position χ along the interface. Since we consider the initial concentration profile being a Heaviside step function, equation (S6) is solved by:

$$c(\chi, \rho) = c_0 \cdot \left(\frac{1}{2} + \frac{1}{2} \cdot \operatorname{erf} \left(-\frac{\sqrt{\hat{v}_\chi} \cdot \rho}{\sqrt{4D \cdot \chi}} \right) \right) \quad (3.10)$$

The flux $J(\chi)$ of analytes across the interface at a specific point χ along the interface is given by the gradient of the concentration in direction of ρ at χ :

$$J(\chi) = -D \cdot \frac{\partial c(\chi, 0)}{\partial \rho} = c_0 \cdot \sqrt{\frac{D \cdot \hat{v}_\chi}{4\pi \cdot \chi}} \quad (3.11)$$

To obtain the rate $\partial n_D / \partial t$ of analytes diffusing across the interface, we integrate $J(\chi)$ along one-half of the interface and account for the apex-to-surface distance d , Avogadro's number N and a factor two for symmetry:

$$\frac{\partial n_D}{\partial t} = 2d \cdot N \cdot c_0 \cdot \int_0^{\chi_{max}} \sqrt{\frac{D \cdot \hat{v}_\chi}{4\pi \cdot u}} du \quad (3.12)$$

The injection flow rate of processing liquid, Q_{i1} , defines the total rate of analytes transported through the confined liquids that can be evaluated as $\partial n_{in} / \partial t = N \cdot c_0 \cdot Q_{i1}$.

The dilution γ is expressed as the ratio between the rate of analytes diffusing from the processing liquid into the shaping liquid and the total rate of analytes transported through the confined liquids:

$$\gamma = \frac{\frac{\partial n_D}{\partial t}}{\frac{\partial n_{in}}{\partial t}} = \frac{2d}{Q_{i1}} \int_0^{\chi_{max}} \sqrt{\frac{D \cdot \hat{v}_\chi}{4\pi \cdot u}} du \quad (3.13)$$

3.5.5 Experimental validation of modelled loss per recirculation

To obtain a numerical value for γ , we developed a Matlab routine to calculate \hat{v}_χ for any position χ along the interface and to numerically evaluate the integral in equation (10). Theoretical values for γ are presented and compared to experimental dilution values in the following section.

The analyte concentration in the processing liquid will reduce for each circulation cycle. To experimentally measure this reduction in concentration, we recirculated a fluorescent dye (Rhodamine B) back and forth (cycles) and observed the drop in fluorescence. Using the hierarchical HFC with an injection flow rate $Q_{i1} = 1 \mu\text{l}/\text{min}$, we measured an average drop in fluorescence of $10.67 \pm 1.05 \%$ per cycle, corresponding to 36.2 % of the initial concentration after 10 cycles (Figure 3.8a, black). For a second injection flow rate, $Q_{i1} = 2 \mu\text{l}/\text{min}$, the fluorescence reduces by $4.75 \pm 0.38 \%$ per cycle, which corresponds to 64.5 % of the initial concentration after 10 cycles (Figure 3.8a, red). In comparison, the use of a single flow confinement resulted in a fluorescence reduction of 66 % after only one cycle, and a concentration as low as 0.09 % after 10 cycles (Figure 3.8a, dashed line). These results suggest that during recirculation the hierarchical HFC has the significant advantage of minimizing the dilution of the processing liquid compared with single HFC.

We also investigated the dilution of the processing liquid as a function of d for flow rates $Q_{i1} = 1, 2$ and $3 \mu\text{l}/\text{min}$, which are commonly used when operating the MFP (Figure 3.8b) and made two important observations. First, dilution in the inner flow confinement increases with the apex-to-surface distance. Indeed, when d increases, the boundary surface between the inner and outer flow confinements increases. In addition, for a given flow rate, the apex-to-surface distance will have an impact on the flow velocity at the interface, and therefore on the amount of analytes that can diffuse through the boundary prior to being reaspirated. Second, dilution is lower at higher flow rates: an increase of the flow rate results in an increase of the flow velocity along the boundary. This implies that both the net flux of analytes diffusing to the surface, $\partial n_D / \partial t$, and the total amount of analytes injected through the aperture $\partial n_{in} / \partial t$ will increase, the former less than

the latter, resulting in increased dilution as $\gamma = \frac{\frac{\partial n_D}{\partial t}}{\frac{\partial n_{in}}{\partial t}}$.

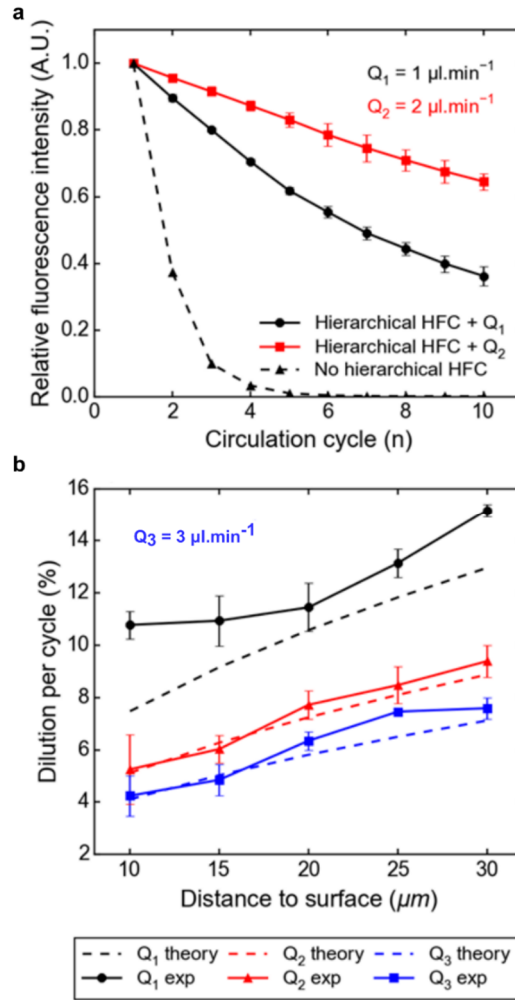


Figure 3.8: Factors impacting the dilution of the processing liquid. a) For a fixed apex-to-surface distance ($d = 20 \mu\text{m}$), fluorescence measurements ($n = 5$) of the processing liquid show the dilution at each circulation cycle for different flow rates $Q_{o2} = Q_{i1} = 1$ and $2 \mu\text{l}/\text{min}$. b) Comparison of the dilution per circulation cycle between theory and experiments for three flow rates $Q_{o2} = Q_{i1} = 1, 2$ and $3 \mu\text{l}/\text{min}$ ($n = 5$).

Both the experimental results and the analytical model exhibit similar trends and dilution values. As an example, for $Q_3 = 3 \mu\text{l}/\text{min}$, we used our analytical model to calculate the dilution of 4.11 % and measured a dilution of $4.24 \pm 0.78 \%$ for an apex-to-surface distance $d = 10 \mu\text{m}$. This excellent correlation between experiments and theory suggest that dilution is indeed primarily driven by diffusion at the liquid-liquid interface. At low flow rates, for example, $Q_1 = 1 \mu\text{l}/\text{min}$ and for distances below $20 \mu\text{m}$, we observed a minor discrepancy between the model and experimental results. This is potentially due to the change of the three-dimensional shape of the HFC that we noticed experimentally and not accounted for in our model.

Therefore, according to both analytical and experimental dilution values, efficient recirculation is favored at higher flow rates and when the head is in proximity of the surface. We note however that the flow rate will influence the amount of processing liquid used per circulation cycle. This implies that for a finite volume of processing liquid, there is a trade-off between the flow rate of the processing liquid and the number of circulation cycles per minute for a given volume of processing liquid. Depending on the application, parameters such as apex-to-surface distance and flow rates need to be adjusted to ensure proper surface processing and minimal loss of processing liquid.

3.5.6 Deposition of analytes on a surface using the MFP.

Binding of secondary antibodies to the surface results in the formation of a depletion zone within the HFC. This depletion zone significantly limits the flux of antibodies to the surface and is therefore of interest in this analysis. For quantitative description of the influence of the depletion zone on the transport of analyte to the surface, we adapt an analytical approach summarized by Squires *et al.* [115]. The “global” Péclet number Pe_g is a measure for the size of the depletion zone relative to the geometrical boundaries of the HFC and is evaluated as:

$$Pe_g = \frac{Q_{i1}}{D_{Ig} \cdot W_{HFC}} \approx 2 \cdot 10^3 \quad (3.14)$$

where W_{HFC} is the maximum width of the HFC footprint, Q_{i1} is the imposed flow rate in the inner HFC and $D_{Ig} = 3.9 \cdot 10^{-7} \text{ cm}^2/\text{s}$ [125] is the diffusion coefficient of the antibodies to be deposited. We assume an inner HFC with $L_{HFC} = W_{HFC} = 250 \text{ }\mu\text{m}$, an injection and aspiration flow rate $Q_{i1} = 1 \text{ }\mu\text{l}/\text{min}$. Hence, for flow conditions to be expected during MFP operation, $Pe_g \gg 100$ and thus the depletion zone is small compared to the size of the HFC. The “local” Péclet number Pe_l is a measure for the thickness of the depletion zone relative to the length of the deposition area and is given by:

$$Pe_l = 6Pe_g \cdot \left(\frac{L_{HFC}}{d}\right)^2 \approx 2 \cdot 10^6 \quad (3.15)$$

As $Pe_l \gg 100$, the thickness of the depletion zone is small compared to the length of the HFC footprint. While size and shape of the depletion zone obeys the advective transport of analyte, solely diffusive transport enables the analyte to pass through the depletion zone and to eventually interact with the surface. With Pe_g and Pe_l being large, the dimensionless flux \mathcal{F} of analyte molecules through a thin depletion zone as described above can be calculated numerically [115], [122] as:

$$\mathcal{F} \approx 0.81 \cdot Pe_l^{\frac{1}{3}} + 0.71 \cdot Pe_l^{-\frac{1}{6}} - 0.2 \cdot Pe_l^{-\frac{1}{3}} \approx 95 \quad (3.16)$$

After estimating the flux of analyte to the surface, we now focus on the interaction between the primary and secondary antibodies on the surface. We assume this interaction to obey first order Langmuir kinetics. The Damköhler number Da represents the ratio between the consumption of analyte on the surface and transport rate of analytes. For $Da \gg 1$, the deposition process is transport limited, whereas for $Da \ll 1$, the process is reaction limited. For the assumed system geometry, flow conditions and the chosen analyte receptor system, Da can be evaluated as follows

$$Da = \frac{k_{on} \cdot b_m \cdot L_{HFC}}{D_{Ig} \cdot \mathcal{F} \cdot N} \approx 2.8 \quad (3.17)$$

We used a set of parameters typical of MFP operation: a surface area of $250 \text{ }\mu\text{m} \times 250 \text{ }\mu\text{m}$ presenting binding sites at a density of $18000 \text{ sites}/\mu\text{m}^2$ and a processing liquid containing an antibody solution. The molar weight of the dispersed antibodies is 150000 g/mol and their diffusion coefficient is estimated to be $3.8 \times 10^{-7} \text{ cm}^2/\text{s}$. For the binding reaction, we presume first order Langmuir kinetics with $k_{on} = 10^6 \text{ l/mol}\cdot\text{s}$ and $k_{off} = 10^3 \text{ s}^{-1}$ [122].

Advective transport of molecules, as in the MFP, helps to reduce the thickness of the depletion layer and speed up diffusion limited reactions in the domain of $Da \gg 1$. In contrast, reaction limited surface interactions ($Da \ll 1$) can be sped up by using higher concentrations of the analytes. The strength of the MFP in such a scenario lies in the ability to deploy and recirculate small volumes of reagents.

Assuming first order Langmuir kinetics and accounting for the diffusion-limited transport to the surface, the dynamics of the surface density of bound analytes $b_{MFP}(t)$ can therefore be described by:

$$b_{MFP}(t) = \frac{k_{on}c_0b_m}{k_{on}c_0 + k_{off}} \left(1 - e^{-\frac{k_{on}c_0+k_{off}}{Da} \cdot t} \right) \quad (3.18)$$

where the retarding effect of the limited flux through the depletion zone is accounted for by the factor Da^{-1} .

When the processing liquid is pipetted onto a surface coated with a primary antibody, the growth of the depletion zone is not counterbalanced by advective transport and the flux of analytes to the surface reduces continuously. Consequently, the Damköhler number depends on time and thus the surface density of bound analytes for pipette-based deposition $b_{Pipette}(t)$ can be approximated as:

$$b_{Pipette}(t) = \frac{k_{on}c_0b_m}{k_{on}c_0 + k_{off}} \left(1 - e^{-\frac{(k_{on}c_0+k_{off}) \cdot 40D_{Ig} \cdot N}{k_{on}b_m L_{HFC}} \cdot \sqrt{t}} \right) \quad (3.19)$$

The metric $\varepsilon(t)$ that quantifies the benefit of convective transport as compared to diffusion-driven transport for surface biopatterning. The ratio $\varepsilon(t)$ of analyte bound with the MFP compared with that of pipette deposition can be evaluated as:

$$\varepsilon(t) = \frac{\left(1 - e^{-\frac{k_{on}c_0+k_{off}}{Da} \cdot t} \right)}{\left(1 - e^{-\frac{(k_{on}c_0+k_{off}) \cdot 40D_{Ig} \cdot N}{k_{on}b_m L_{HFC}} \cdot \sqrt{t}} \right)} \quad (3.20)$$

Chapter 4 Surface interactions at the mm- and cm-scale using hydrodynamic flow confinements

The content of this chapter is based on the pre-print version of below listed research article, which was published in 2016 in *Langmuir*, and is reproduced here with minor modifications with permission from the American Chemical Society.

D. P. Taylor, I. Zeaf, R. D. Lovchik, G. V. Kaigala, “Centimeter-Scale Surface Interactions Using Hydrodynamic Flow Confinements,” *Langmuir*, **2016**, *32*(41), pp. 10537–10544.

The later part of this chapter presents work on rapid μ IHC, which is currently being drafted as a manuscript and is to be submitted for review in fall 2019.

R. D. Lovchik, D. P. Taylor, G. V. Kaigala, “Rapid micro-immunohistochemistry,” *manuscript under preparation*.

My contributions to this publication were:

- Theoretical, numerical and analytical modelling
- Design and fabrication of the vertical probe heads
- Building the experimental setup
- Experimental work
- Writing of the manuscript and creation of the figures for the paper published in *Langmuir*.

4.1 Abstract

The following chapter covers two complementary packages of work pertaining to mm- to cm-scale interfacing with immersed bio-interfaces.

The first and main package of work focuses on selective chemical interactions with immersed substrates at the cm-scale using **vertical probe heads in scanning mode**: Our implementations enable both sequential and simultaneous delivery of multiple reagents to a substrate as well as the creation of gradients of reagents on surfaces. The method is based on localizing sub-microliter volumes of liquids on an immersed surface with a microfluidic probe (MFP) using a principle termed hydrodynamic flow confinement (HFC). We here show spatially-defined multiplexed surface interactions while benefiting from the probe capabilities such as non-contact scanning operation and convection-enhanced reaction kinetics. Three-layer glass-Si-glass probes were developed to implement slit-aperture and aperture-array designs. Analytical and numerical analysis helped to establish probe designs and operating parameters. Using these probes, we performed

immunohistochemical (IHC) analysis on individual cores of a human breast-cancer tissue microarray. We applied α -p53 primary antibodies on a 2 mm diameter core within 2.5 min using a slit-aperture probe (HFC dimension: 0.3 mm \times 1.2 mm). Further, multiplexed treatment of a tissue core with α -p53 and α - β -actin antibodies was performed using four adjacent HFCs created with an aperture-array probe (HFC dimension: 4 \times 0.3 mm \times 0.25 mm).

The second part of this chapter work focusses on the rapid implementation of sequential interactions with bio-interfaces at the mm-scale using **horizontal probe heads in non-scanning mode**. Horizontal probe heads enable the formation of radial HFCs and thus allow the implementation of homogeneous incubation conditions on top of independent circular sites of a bio-interface. Combined with a fluidic architecture allowing for the rapid exchange of the processing liquid in the HFC, this enables the rapid, spot-wise implementation of sequential bio-chemical protocols and is therefore highly suited for the spot-wise IHC analysis of samples. While each interaction site, measuring about 1mm across, is large enough to allow for the retrieval of statistically significant data, several independent interaction sites can usually be fit on a single sample. We used this to implement an array of 14 interaction sites on a cell block section following a design of experiment to determine the impact of variations in the incubation time of single steps in the protocol. The obtained data can be used to optimize the trade-off between signal intensity, signal contrast and processing time in IHC workflows, or to e.g. characterize batch-to-batch variation of bio-chemicals.

The ability of these devices and methods to perform multiplexed assays, present sequentially different liquids on surfaces and interact with surfaces at the mm- to cm-scale will likely spur new and efficient surface assays.

4.2 Introduction

Compartmentalization is central to studying the effect of various (bio)chemical microenvironments on biological entities. Such testing and analysis of multiple parameters are useful in (bio)chemical screening, analysis, synthesis and characterization with applications, for instance, in drug discovery, studies of cell-to-cell communication, and tumor marker detection [126]–[129]. Microtiter plates are currently one of the most common substrates for compartmentalized assays in both research and diagnostics. To increase the analytical throughput, the trend has been to reduce the footprint and volume of each well of the microtiter plates, with the current footprint of standard wells measuring 1.5 mm \times 1.5 mm (1536 well plates). Further scaling of the microtiter plates is hindered by constraints in fabrication together with requirements for liquid and mechanical interfacing and imaging. These limitations have triggered a drive towards surface-based assays. Such surface formats, called microarrays, use lithographic methods, inkjet printing and pin spotting to produce high-density patterns on surfaces [130]. These surface assays have the potential to enable high-throughput analytical testing while simplifying read-out and detection. However, their lack of physical compartmentalization hinders multiplexing of liquid reagents and indicates the need for a new set of tools to enable targeted interaction with biological samples such as DNA/protein microarrays, tissue sections and cell monolayers. Such a tool should ideally be able to: (i) interact with the substrate on spatially distinct areas at the mm- to cm-scale; (ii) deliver different liquids to a surface in both a parallel and sequential manner; (iii) enable interaction with the surface without physical contact between the tool and the surface, and (iv) operate in a wet environment to avoid drying artefacts. Several techniques have been developed that allow local processing of immersed substrates [13], [21], [24], [25], [131] and fulfill subsets of the above criteria. However, a versatile method to interact efficiently with immersed, cm-scale substrates in a localized manner remains elusive.

Pin spotters and inkjet systems are established technologies primarily used for patterning reagents on a dry surface and are not suitable to implement biological assays on surfaces [102], [132]. Aqueous two-phase systems implemented on immersed substrates by means of an inkjet-like nozzle have been used for patterning mammalian cells and bacteria [21], [133], but the spatial resolution and the limitations imposed by diffusion between the two phases are not favorable for confining molecular reagents. Rapp *et al.* demonstrated cm-scale patterning of antibodies using selective UV irradiation enabled by a digital micromirror device [134]. This method is limited to photo-initiated reactions and does not allow a selective change of the liquid environment on a surface. Local processing was also demonstrated by Kim *et al.* by conformably sealing microchannels on surfaces but without the ability to stain specific regions of interest [12], [13]. In addition, mechanical contact can introduce cross-contamination and adverse mechanical stress on the biological sample, which is also the case for another contact-based device, namely the chemistode [17], a microfluidic device that is sealed to a substrate to localize interactions. Atomic force microscope (AFM)-based methods and their derivatives, such as the FluidFM [9] and dip-pen lithography [135], [136], enable local interaction with biological substrates with high resolution, but their narrow range of operation (which is $\sim 150 \mu\text{m} \times 150 \mu\text{m} \times 20 \mu\text{m}$) is not compatible with cm-scale substrates. Other methods for high-precision interfacing with biological substrates are scanning ion conductance microscopy [10], [20] and scanning electrochemical microscopy [137], [138], both requiring implementation of reference electrodes and maintenance of specific homogeneous buffer conditions. This complicates the application of different processing liquids in (bio)chemical surface-based assays.

A promising technology for local interaction with immersed substrates is the microfluidic probe and its variants (MFP) [24]–[26]. The MFP operates in a non-contact scanning mode and localizes a liquid on a surface by creating a hydrodynamic flow confinement (HFC) (Figure 4.1a). Using the MFP, interactions with surfaces on length scales ranging from single μm to several hundred μm have been demonstrated. The MFP and its variants have been applied for multiplexed immunohistochemical analysis of tissue sections [139], biopatterning [30], and pharmacology on a single-cell level [140]. In the configurations of the probes used thus far, the contact area of the processing liquid with the substrate is smaller than $200 \mu\text{m} \times 200 \mu\text{m}$.

Processing an area of, for instance, 1 cm^2 would require scanning the area of interest for extended periods of time, when sufficient local incubation times are taken into account. Therefore, despite the favorable attributes listed above, excessively long processing times as well as varying processing conditions due to scanning render the probe technology in its current form unsuitable for cm-scale surface assays.

In this chapter, we present novel vertical and horizontal microfluidic probe devices along with a methodology for selective delivery of microliter volumes of processing liquids to immersed substrates on the cm and mm length-scales. This enables new strategies for multiplexed surface-based assays: uniform, localized exposure to a single reagent (Figure 4.1b, left), multiplexed exposure to several reagents (Figure 4.1b, right), and gradients of several reagents (Figure 4.1b, center). We present two families of probes, one with slit-aperture designs for interacting with a surface using a single reagent and creating concentration gradients, and the second one with aperture-array designs for multiplexed interaction and for creating concentration gradients. We demonstrate the efficacy and applicability of our devised designs in the context of surface assays by performing uniform and multiplexed immunohistochemistry on tissue sections and by patterning proteins on a surface (Figure 4.9).

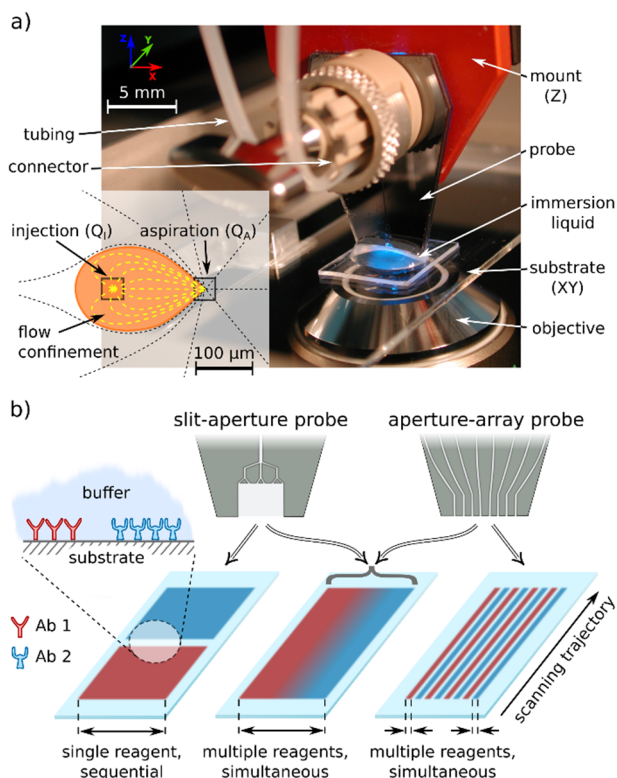


Figure 4.1: Strategies for HFC-based interaction on the cm-scale using vertical probe heads. a) The probe is positioned $\sim 5 \mu\text{m}$ to $50 \mu\text{m}$ above a substrate. Inset: an HFC between the probe and the surface is created by setting the ratio of the injection flow rate (Q_I/Q_I) to the aspiration flow rate (Q_A/Q_A) to $\sim 1:3$. b) Two families of probes, slit-aperture probes and aperture-array probes, enable several strategies of interfacing with surfaces: sequential exposure (left), multiplexed exposure to different reagents on spatially separated regions (right), and creation of gradients (center). Inset: schematic of antibodies patterned on a substrate immersed in physiological buffer.

4.3 Results and discussion

4.3.1 Vertical probe design and operating conditions for mm-scale HFCs

Two-layer Si/glass probes allow the formation of a μm -scale drop-shaped HFC by simultaneously injecting and aspirating a processing liquid between adjacent apertures at the apex (Figure 4.2a) [26]. Extending the HFC in one dimension can potentially enable processing on the cm-scale by scanning in the direction perpendicular to the direction of extension. Intuitively, one would design probes with increased spacing between the two adjacent apertures, resulting in an HFC that is elongated along its main axis. This however is not a viable approach for the following reasons: (i) the resulting HFC would be significantly broad in the proximity of the injection aperture and rather narrow in the proximity of the aspiration aperture (a “stretched” drop shape). This change in width would result in non-uniform incubation times at different positions of the HFC, and would become prominent when scanning the substrate in the direction perpendicular to the direction of extension (main axis of the HFC, Figure 4.2a), (ii) to realize HFC at reasonable flow rates ($Q_I/Q_A \geq 1/5$), the distance between adjacent apertures may not be larger than the shortest distance between an aperture and the edge of the apex. The maximum spacing between the adjacent apertures is therefore limited to the thickness of the glass and Si substrates.

Another approach for enlarging the HFC is to increase the dimensions of the apertures perpendicularly to the main axis of the HFC. In a two-layer probe, this can be done by increasing the etch depth d , which is as well

limited by the thickness of the Si substrate. We note that fabrication techniques with different materials, e.g. plastics, might provide additional options for scaling of the apertures. However, in the context of biological assays, probes in Si and glass offers several advantages, such as (i) high-resolution features and geometries, (ii) chemical inertness, (iii) robust thermo-mechanical properties, (iv) good optical properties, (v) controllable surface properties, and (vi) robust and established protocols for fabrication and quality control [26]. To enable scaling of the apertures while leveraging the advantages of Si/glass probes, we present a three-layer probe design, which allows the main axis of the HFC to be oriented perpendicularly to the Si and glass layers (Figure 4.2b). In such a design configuration, the HFC can be extended homogeneously in one dimension by scaling w . Also, w can be varied independently for each aperture, and scaling is independent of the thicknesses of the Si and glass substrates. This allows the fabrication of probes with adjacent slit apertures (Figure 4.2b) or arrays of adjacent apertures (Figure 4.2c).

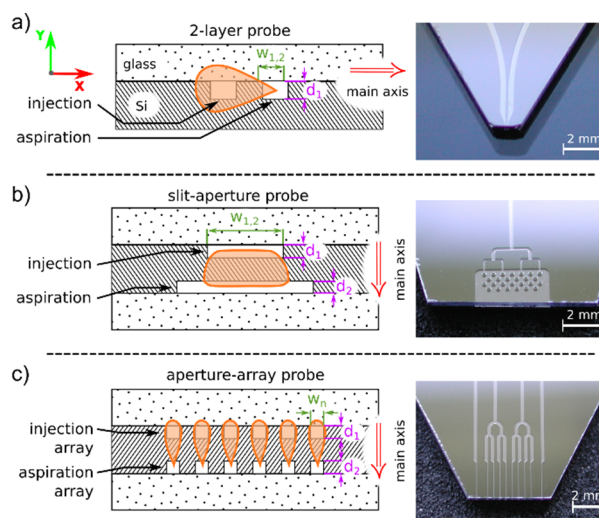


Figure 4.2: Design of slit-aperture and aperture array probes. a) Left: schematic of a two-layer probe with channels etched on the face of the silicon substrate and then covered by glass. Aperture designs are restricted to linear configurations with a common etch depth, d . Right: photograph of a two-layer probe with two channels leading to the apex. b) Left: schematic of a slit-aperture probe for creating a homogeneous HFC, which is scalable in one dimension (along the X-axis). Right: photograph of a slit-aperture probe. Channels connecting to slit apertures are bifurcated to provide a homogeneous distribution of the flow through the aperture. c) Left: schematic of an aperture-array probe for creating parallel HFCs. Right: photograph of the aspiration side of an aperture-array probe. While the injection apertures are addressed independently, the aspiration apertures are grouped to minimize external fluidic interconnects.

4.3.2 Slit-aperture probes

We performed numerical simulations of liquid flow in the gap between the probe and the substrate to study and optimize the flow patterns generated by slit-aperture probes. We fixed the distance between the probe and the substrate at $30\ \mu\text{m}$ and $Q_I/Q_A = 1/5$. Figure 4.3a is a false-color image of the relative amplitude of the flow velocity in the center plane between the probe and the substrate (XY -center plane) for a design with identical slit lengths. The operating condition $Q_I/Q_A = 1/5$ is reflected by high velocity amplitudes in the vicinity of the aspiration aperture. Figure 4.3c (top) highlights the flow path of the processing liquid in the YZ -center plane for slit apertures of identical length and the operating conditions mentioned. The simulation results suggest that under such operating conditions, a sheath flow of immersion liquid prevents the confined processing liquid from contacting the substrate. The sheath flow results from the fact that more liquid is aspirated from the region of the injection aperture, than the injection aperture supplies. Therefore, flow from the injection aperture is complemented with a flow of immersion liquid. To further understand this

failure mode, we developed a simplified analytical model in which we neglect the effects at the edges of the apertures and only consider flow in the Y -direction. In three-layer Si/glass probes with slit apertures, the distance between the aspiration aperture and the closer edge of the apex in the Y -direction (lower edge of the apex) is $500\ \mu\text{m}$, whereas the distance to the farther edge (upper edge of the apex) is $775\ \mu\text{m}$. We assumed that the pressure difference between the aspiration aperture and both the lower and the upper edge is identical. We further assumed that the hydrodynamic resistance between the aspiration aperture and the edges scales linearly with distance. Therefore, the relative aspiration flow supplied from the upper edge of the apex can be calculated as $100\% \times (1 - 775\ \mu\text{m}/(500\ \mu\text{m} + 775\ \mu\text{m})) \approx 40\%$. If the injection flow is lower than this 40% fraction of the aspiration flow, as is the case for $Q_I/Q_A = 1/5$, additional liquid flow is required from the upper edge of the apex. For slit apertures of the same length, this results in a sheath flow of immersion liquid under the flow of processing liquid, thereby hindering interaction of the processing liquid with the substrate. Contact between the processing liquid and the substrate can be enforced by providing an injection flow that exceeds the aspiration flow in the vicinity of the injection aperture. The fraction of the aspiration flow drawn in from the region of the injection aperture would nonetheless remain unchanged and not all of the injected liquid would be recollected by the aspiration aperture. In such a case, the processing liquid would not be confined. Slit apertures of identical length are therefore unsuitable for interacting with a substrate using HFC, as there is no operating range between the two failure modes of (i) no contact between the processing liquid and the substrate, and (ii) the loss of confinement of the processing liquid.

These failure modes however can be avoided by designing the aspiration aperture to be longer than the injection aperture. We performed numerical analysis of the flow conditions for a probe with apertures with a length ratio of $L_I/L_A = 1/4$. With the ratio of flow rates remaining at $Q_I/Q_A = 1/5$, significantly less liquid is aspirated from the direction of the injection aperture (Figure 4.3b), and the injection flow is not smaller than the aspiration flow in the vicinity of the injection aperture. This results in the formation of a stagnation zone between the edge of the apex and the injection aperture, indicating that a screening sheath flow of immersion liquid is not formed and that thus the confined processing liquid gets in contact with the surface (Figure 4.3c, bottom).

A longer aspiration aperture also ensures a stable confinement of the processing liquid over a broader range of Q_I/Q_A values, because on both sides of the injection aperture there is still flow of immersion liquid from the upper edge of the apex. This results in a shielding flow of immersion liquid around the HFC. Before the confinement of the processing fails and the processing liquid streams into the immersion liquid from the upper edge of the apex, the injection flow would have to overcome this shielding flow of immersion liquid. Therefore, in a specific range of Q_I/Q_A , the fraction of the injection flow that exceeds the aspiration requirement in vicinity of the injection aperture is still recollected by the aspiration aperture and, in part, compensates for the flow that would be aspirated from the lower edge of the apex.

As per the model, the minimum Q_I/Q_A ratio required for the processing liquid to contact the substrate scales with L_I/L_A :

$$\frac{Q_I}{Q_A} = 0.4 \cdot \frac{L_I}{L_A} \quad (4.1)$$

Leakage of the processing liquid from the upper edge of the apex occurs when the injection flow saturates the fraction of the aspiration aperture that corresponds to the length of the injection aperture (see Figure 4.3c, hatched area).

An upper threshold for Q_I/Q_A can be therefore defined by

$$\frac{Q_I}{Q_A} = \frac{L_I}{L_A} \quad (4.2)$$

Figure 4.3d illustrates the operating range to be expected based on the above estimations. For choosing the appropriate ratio of lengths of apertures, two general trends have to be considered: a high ratio of L_I/L_A results in a higher ratio of Q_I/Q_A required to ensure contact between the processing liquid and the substrate. This makes the HFC more prone to perturbations caused by scanning movements of the probe. A low ratio of L_I/L_A in turn enables the generation of a more stable HFC, but offers a smaller working range for the ratio of Q_I/Q_A . We experimentally verified the validity of the discussed solution using a design with $L_I/L_A = 1/4$, as this ratio of lengths offers a comfortable working range, while providing good stability during scanning movements. For this design we also analyzed the confinement conditions at different values of Q_I/Q_A with a processing liquid containing fluorescein (Figure 3d, inset). The model predicts a loss of confinement for $Q_I/Q_A > 1/4$. We verified experimentally that at this condition the HFC starts to bend around the edges of the injection aperture and is susceptible to leakage of the processing liquid, in particular during scanning mode of operation (Figure 4.3d, inset II).

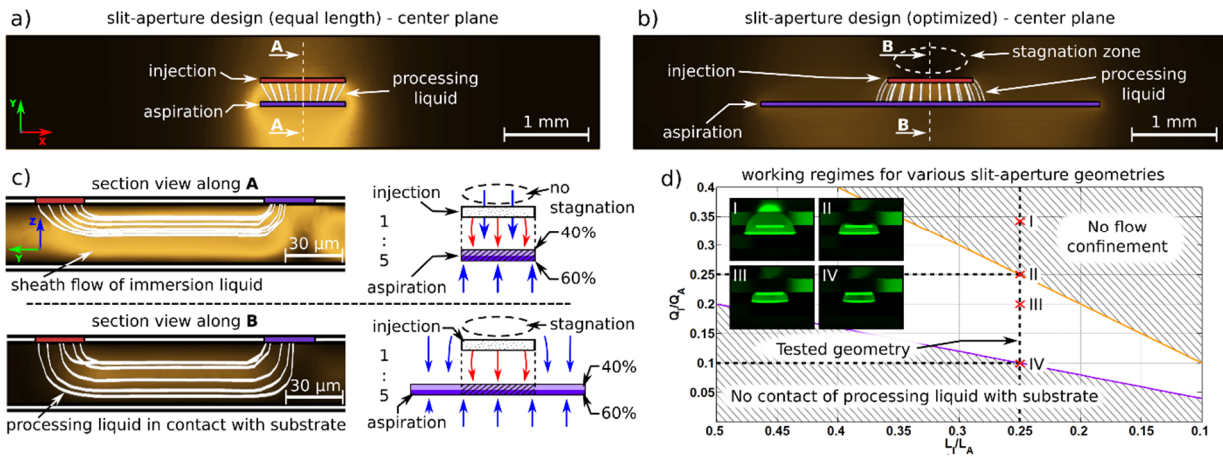


Figure 4.3: Optimization of slit-aperture probe designs and operating parameters. a) Numerical simulation of relative amplitude of flow velocity (zero flow velocity in black regions, high flow velocity in bright regions) and flow pattern of injected processing liquid (white streamlines) in the horizontal middle plane between probe and substrate for a probe design with slit apertures of identical length. b) A probe design with an aspiration aperture that is 4× longer than the injection aperture. c) Relative amplitude of flow velocity in vertical planes along the lines **A** and **B** indicated in a) and b). For slit apertures of same length (top), a sheath flow of immersion liquid screens the confined processing liquid from contacting the surface (see sketch on the right. Read arrows: flow of processing liquid, blue arrows: flow of immersion liquid). In a slit-aperture probe (bottom) with the design illustrated in b), no sheath flow of immersion liquid is formed. d) Working regime of Q_I/Q_A for different values of the aperture length ratio L_I/L_A . Insets: photographs of HFCs of a processing liquid containing fluorescein for an aperture length ratio of 1:4 at different values of Q_I/Q_A .

4.3.3 Aperture array probes

An array of HFCs enables multiplexed and simultaneous processing of a substrate with different reagents. Numerical analysis of the flow patterns in the XY -plane (gap distance 30 μm, $Q_I/Q_A = 1/4$) suggests that in such a probe design there can be cross-talk between the HFCs at the extremities of the array and their adjacent HFCs (Figure 4.4a, top). The aspiration apertures for the HFCs at the extremities of the array can aspirate liquid from the X -direction (Figure 4.4a, bottom). This is not the case for the other aspiration apertures in the array, as there are competing aspiration apertures on both sides in the X -direction, resulting in a stagnation of flow between neighboring apertures. The additional flow to the aspiration apertures at the edges of the

array results in less liquid being aspirated from the direction of the respective injection apertures. A fraction of the processing liquids injected at the extremities of the array is therefore aspirated by the neighboring aspiration apertures, which alters the adjacent HFC, albeit to a lesser extent. One solution to this problem would be to inject only buffer from the outermost injection apertures and only use the HFCs at the center of the array for confining the actual processing liquids. A more general solution however is to create flow conditions for the HFCs at the extremities of the array that mimic the conditions within the array. This can be achieved by including additional aspiration-only apertures beyond the extremities of the array in the X-direction, which we term stabilization apertures. These stabilization apertures suppress flow from the X-direction to the aspiration apertures of the flanking HFCs resulting in stagnation of flow between the stabilization apertures and the aspiration apertures at the extremities of the array. Those aspiration apertures therefore aspirate mainly from the Y-direction, which leads to a stronger aspiration and therefore a better confinement of the respective processing liquids. The further the stabilization apertures are positioned apart from the array, the stronger aspiration to the stabilization apertures has to be to sufficiently stabilize the HFCs. The cross-talk between HFCs and also the efficacy of the stabilization apertures for averting cross-talk were experimentally verified and are in concordance with numerical simulations (Figure 4.4 a and b, insets).

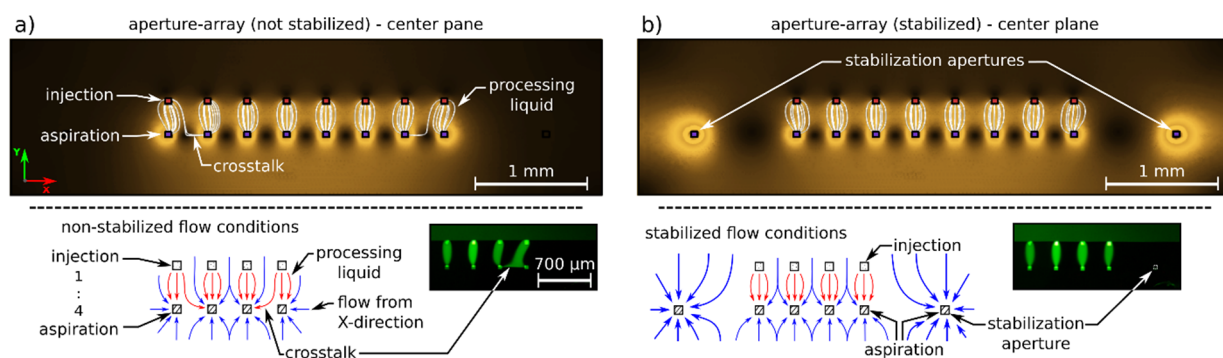


Figure 4.4: Optimization of aperture-array designs. a) Top: numerical simulation of relative amplitude of flow velocity (zero flow velocity in black regions, high flow velocity in bright regions) and the flow pattern of processing liquid (white streamlines) in the middle plane between probe and substrate for an aperture array without stabilization. Bottom: non-symmetric conditions for the aspiration apertures at the extremities of the array lead to cross-talk between HFCs. b) Top: additional stabilization apertures can suppress the cross-talk between single flow confinements. Bottom: stabilization apertures allow the creation of symmetric conditions for the aspiration apertures at the extremities of the array. Insets: photographs of arrays of flow confinements using a fluorescein-containing processing liquid with and without stabilization apertures.

4.3.4 Immunohistochemistry on tissue sections

Using slit-aperture and aperture-array probes, we demonstrated the staining of individual cores of a tissue microarray (TMA). By this we show that the slit aperture and aperture array probes presented in this study (i) allow to generate stable confinement of processing liquids on the mm-scale suited for interaction with standard samples, (ii) short residence times observed in studies with μm -scale HFCs can be transferred to the mm- to cm-range and (iii) the presented devices and methods enable unique strategies to process an immersed, cm-scale sample. Individual cores could be treated with different primary antibodies, or a single core could be exposed to distinct primary antibodies. Importantly, with these new families of probes, it is feasible to stain a core of interest or perform in-depth analysis of a selected core. For uniform mm-scale processing of a single core, we used a design with an injection aperture of $1\text{ mm} \times 0.05\text{ mm}$ and an aspiration aperture of $4\text{ mm} \times 0.05\text{ mm}$ (Figure 4.5a, inset).

This results in an HFC with a width of 1.2 mm, staining an area of about 2.4 mm² when scanned across a tissue core with a diameter of 2 mm. The unprocessed area on this core could be used, for example, to perform analysis with an additional antibody [141]. We performed IHC on a breast-cancer-tissue microarray slide. Here, the primary antibody (Ab) (α -p53, at a concentration of 25 μ g/ml) was delivered with the MFP. We added rhodamine B at a concentration of 10 μ M to visualize the HFC. Rhodamine B binds non-covalently to the tissue and is washed by the flow of immersion liquid during scanning of the probe over the tissue (Figure 4.5a). The HFC extends about 330 μ m in the Y-direction, thus the local incubation time of the primary Ab with the tissue section at the scanning speed of 0.01 mm/s chosen was about 33 s. All other steps of IHC were performed for the entire TMA slide. In contrast to conventional methods, where the primary Ab incubation is in the order of hours, here the incubation is performed within seconds. This is due to the convective transport of the molecules to the substrate, resulting in an enhancement of reaction kinetics, and to the application of higher concentrations of primary Abs. Using the set of parameters given above, we incubated a 2-mm TMA core with primary Abs in 2.5 min, consuming approximately 7.5 μ l of processing liquid. The concentration of primary Abs used in conventional IHC (on the order of 1 μ g/ml) typically is significantly lower compared to the concentrations used in the discussed experiments. We did not focus on minimizing the Ab consumption. However, consumption can be reduced by optimizing the flow rates, incubation times and the Ab concentration. The total time required for processing an entire TMA can be further optimized by using multiple probes, stacked probes, or by creating HFCs with a larger contact area with the substrate.

We also performed multiplexed staining by confining two primary Ab solutions (α -p53 and α - β -actin, both at 25 μ g/ml) in 4 parallel, independent HFCs using an aperture-array probe capable of creating 8 HFCs (Figure 4.5b, inset). The remaining 4 HFCs were run with PBS as processing liquid (processing liquids in the eight adjacent HFCs: PBS – PBS – (α -p53) – (α - β -actin) – PBS – (α -p53) – (α - β -actin) – PBS). The injection flow rate for each HFC was 0.5 μ l/min and $Q_i/Q_A = 1/4$. The area processed with each of the two Ab solutions was about 0.5 mm², which sufficiently provides a measure of the antigen expression within the sample.

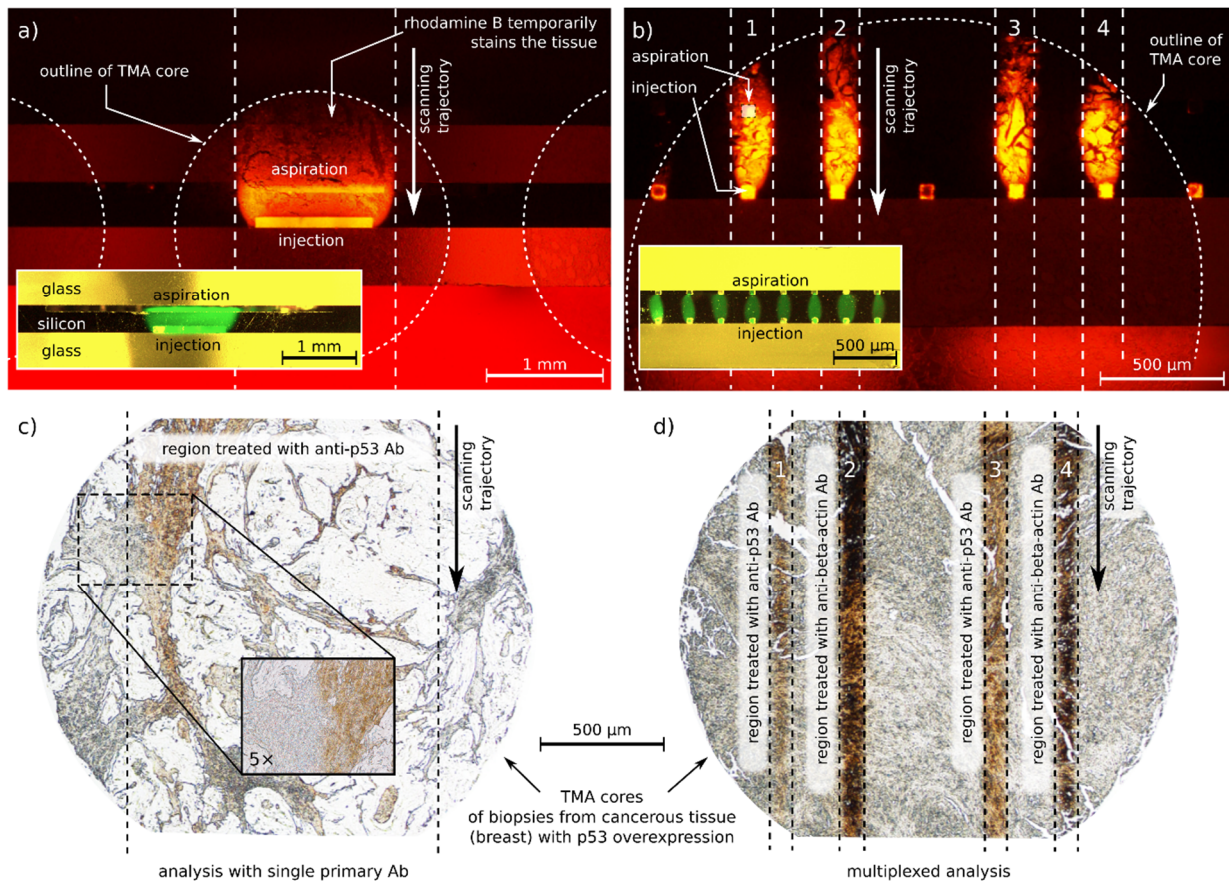


Figure 4.5: Processing of tissue sections in a tissue microarray (TMA) on the cm-scale using HFC. a) Uniform staining of a tissue section overexpressing p53. A slit-aperture probe is used to apply a processing liquid containing α -p53 Abs and rhodamine B. Inset: bright-field image of a slit-aperture probe creating a 1 mm \times 0.3 mm HFC of a processing liquid that contains fluorescein. b) Multiplexed staining of a tissue section overexpressing p53. An aperture-array probe is used to apply processing liquids that contain α -p53 Abs or α - β -actin Abs and rhodamine B. Inset: bright-field image of an aperture-array probe creating eight parallel HFCs of processing liquids containing fluorescein. c) Bright-field image of a tissue section after treatment with α -p53 Abs using a slit-aperture probe and chromogenic visualization. Inset: 5 \times magnification of the edge of treated region. d) Bright-field image of a tissue section after treatment with α -p53 Abs and α - β -actin Abs by means of an aperture-array probe and chromogenic visualization.

4.4 Horizontal probe heads for rapid μ IHC

Above presented slit aperture and aperture array designs enable a fast processing on clinical samples by scanning the HFC across the sample. When evaluating reagents, or classifying samples, it would be nevertheless desirable to implement multi-step reactions on single spots of a statistically relevant area. For this, we developed specific horizontal probe heads (see Figure 4.6) and corresponding holders and interfaces.

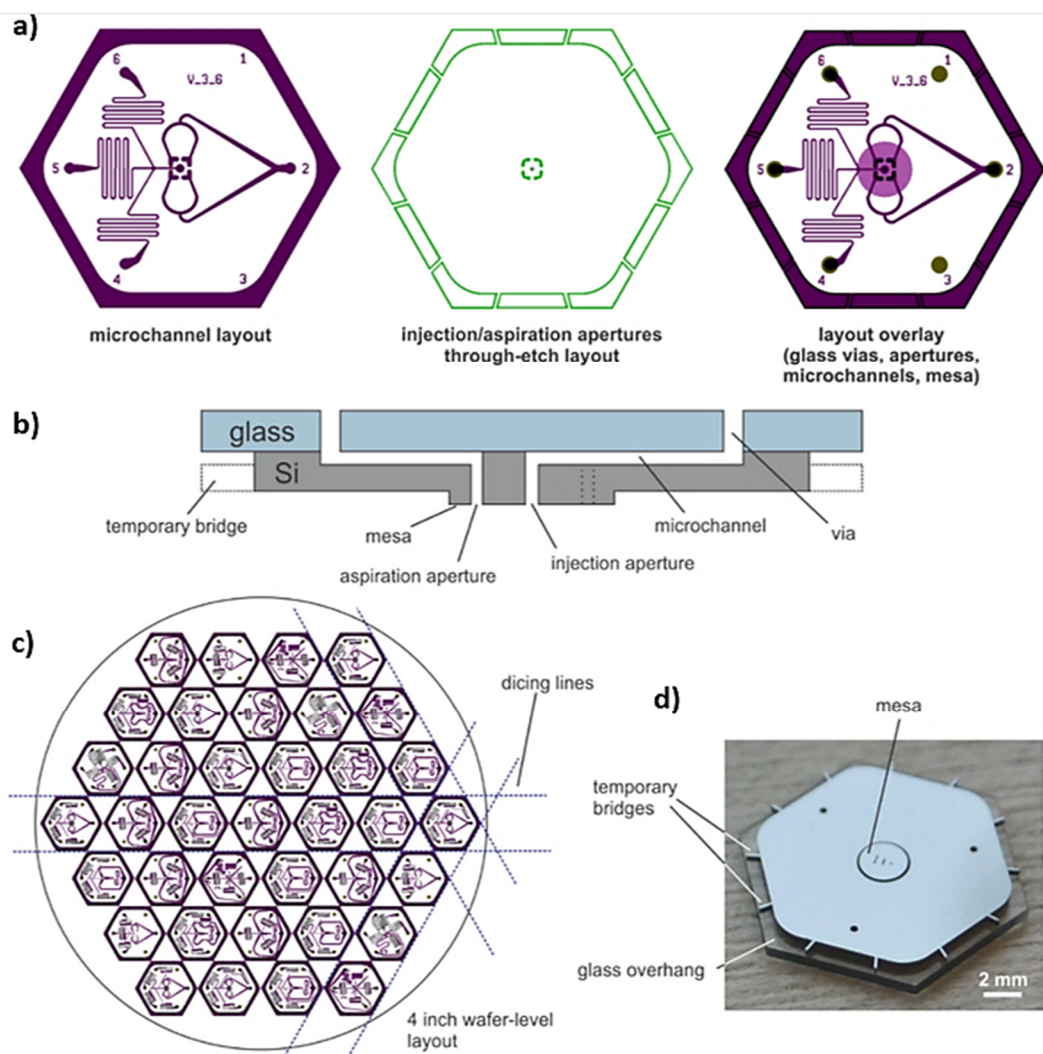


Figure 4.6: Current generation of horizontal probe heads. a) and b) The fluidic routing and the through-holes forming the apertures are implemented on opposing sides of a double-side polished Si-substrate. After etching, the channels are closed off by anodic bonding to a glass substrate with holes for fluidic connection. c) wafer layout with dicing-lines. d) Photograph of horizontal probe head. The temporary silicon bridges are required to keep each probe head in place during processing of the Si-wafers. The bridges are manually removed before a probe head is inserted into the holder.

We make use of a horizontal head design as it enables the implementation of arbitrarily shaped apertures. We designed radial HFCs, which are suited for sequential interactions of liquids on surfaces at the mm-scale. Radial HFCs are formed by central injection of a processing liquid, which is re-aspirated by surrounding, ring-shaped apertures. IHC analysis of tissue sections is a highly sequential process. We decided to locally implement the three core steps of an IHC routine, the application of the primary antibody, the secondary antibody and the streptavidin-peroxidase using horizontal probe heads (see Figure 4.7). These three steps determine the quality of the obtained stain and usually require one up to several hours in on-bench protocols. Due to convection-enhanced deposition and the ability to use higher concentrations without increasing the overall consumption of reagents, the MFP is suited to locally implement the core steps of IHC analysis within minutes. We refer to this method as “rapid μ IHC”.

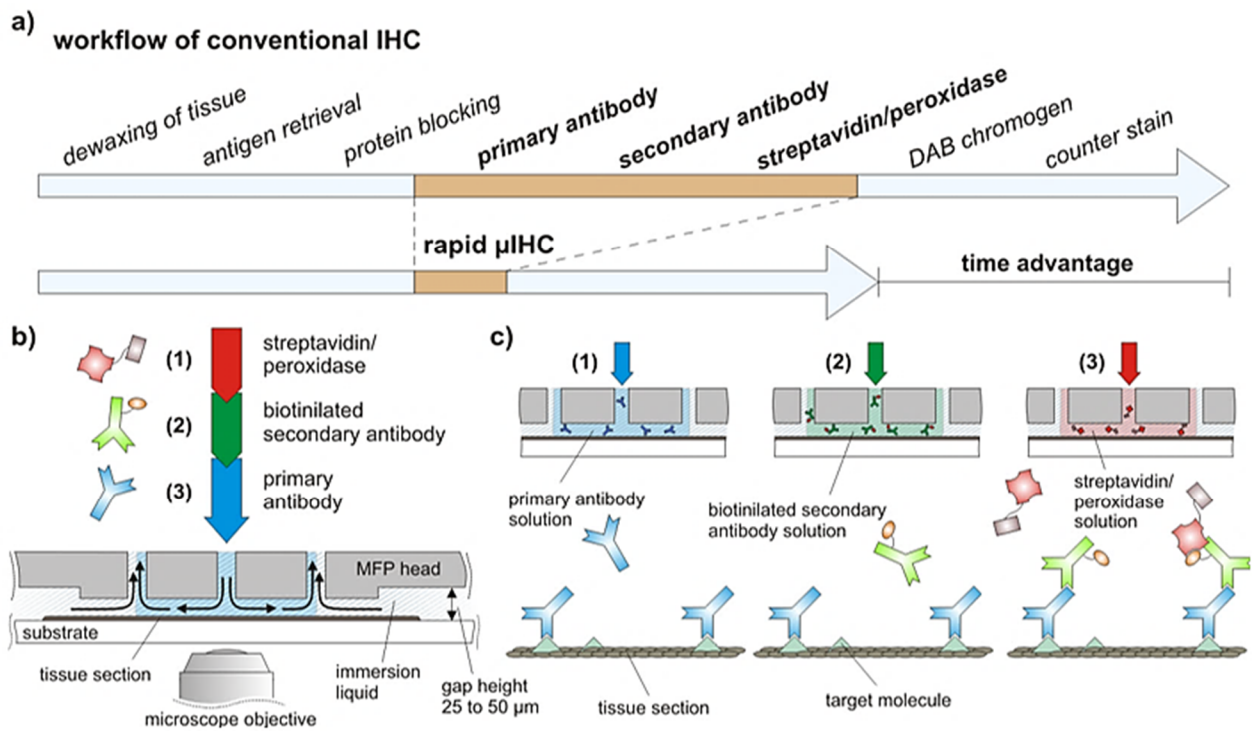


Figure 4.7: Rapid μ IHC-analysis of tissue sections. a) Fast-spot-wise analysis is enabled by implementing the three core steps of an IHC protocol using the MFP and horizontal probe heads. b) The central injection aperture is linked to three channels through which different reagents are injected: the primary antibody binds to a specific target protein of the sample, the biotinylated secondary antibody binds only to the already bound secondary antibody. The streptavidin-peroxidase eventually binds to the biotin-label of the secondary antibody and will affect a local stain upon global application of the DAB chromogen (not displayed).

By linking the central injection aperture to three different channels, the processing liquid in the HFC can be switched with about 2s (see Figure 4.8a). Screening test showed that the impact of the incubation time of the streptavidin-peroxidase has a negligible effect on the signal intensity and contrast. To determine the ideal incubation times for the primary and secondary antibody solutions, we performed a design of experiments (central composite design), in which these two factors were systematically varied (see Figure 4.8b). The implemented design of experiments consisted of independent sequential reaction implemented on 12 spots of the same cell block section. To validate the results, we implemented negative control without primary or secondary antibodies on two additional spots. After spot-wise, sequential incubation, the streptavidin-peroxidase and the DAB chromogen were applied globally. An analysis of the results reveals significant first and second order effects of the incubation time with primary and secondary antibodies. While increasing either of the two incubation times has a positive effect on the signal level, the signal contrast deteriorates for longer incubation with primary antibodies. Our results therefore suggest that an optimized workflow should have a short incubation time for the primary antibody and an about five times longer incubation time for the secondary antibody.

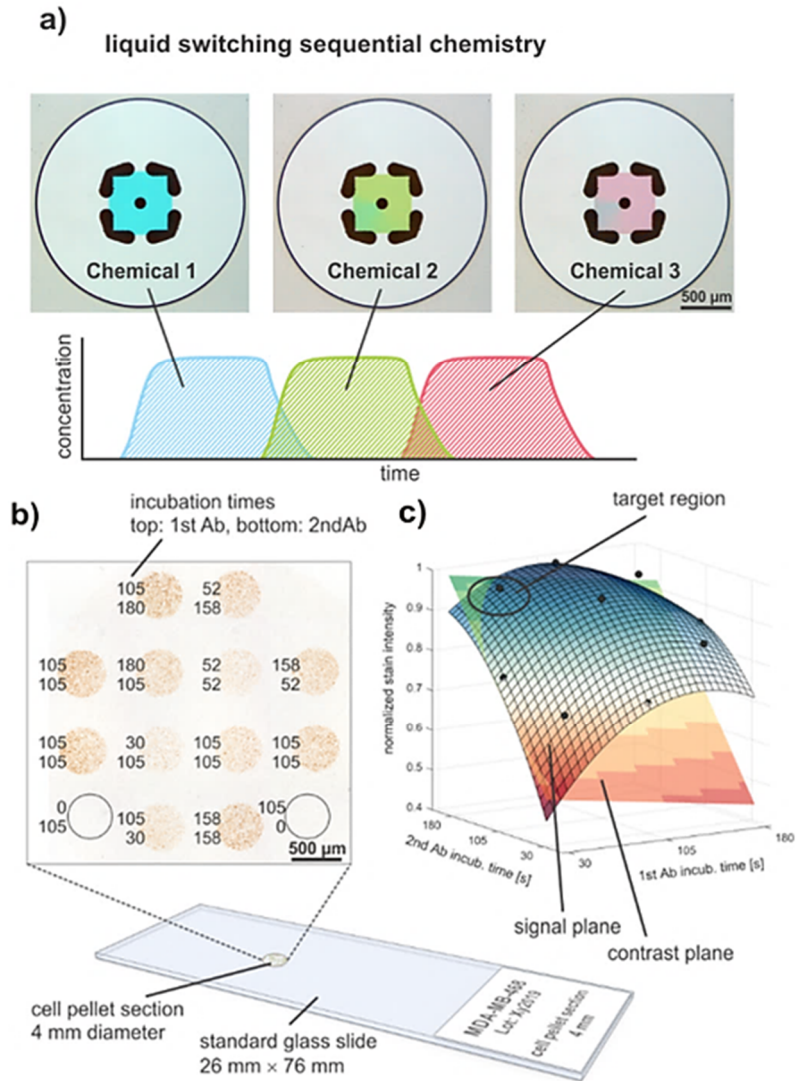


Figure 4.8: Characterization of reagents for rapid μ IHC. a) The processing liquid within the HFC can be switched within about 2s (demonstrated with food dye). b) We implemented a two-factor central composite design together with two negative controls on a single cell block section. Streptavidin-peroxidase and DAB chromogen were applied globally. c) Analysis reveals statistically relevant first and second order effects for both factors. The figure displays the response surfaces for the signal intensity (red-white-blue) and for the signal contrast (red-yellow-blue). The negative curvature of the intensity response surface for long incubation times with primary antibodies does physically not make sense and is considered an artifact, which could be removed by increasing the number of datapoints. As the signal contrast deteriorates for long incubation with primary antibody, relatively short incubation with primary antibodies and relatively long incubation with secondary antibodies results in the best staining results in the analyzed case.

4.5 Conclusion

The devices and methods presented enable versatile and localized interaction of different processing liquids with immersed, mm- to cm-scale substrates. Surface (bio)chemical assays in general would benefit from the ability to sequentially and simultaneously apply different liquids onto a surface. These multiplexing techniques, in combination with the scanning capability of the probe, enable versatile spatio-temporal alterations of selected regions of a substrate.

Slit-aperture probes and aperture-array probes applied in scanning-mode enable the creation of localized gradients on a surface. Using a slit-aperture design, gradients can be created by supplying different liquids to the injection aperture through independent channels. Probes with aperture-array designs allow the creation

of discrete gradients by confining different proportions of two liquids in adjacent HFCs. The width of single HFCs and also the spacing between neighboring HFCs in such an array could be scaled down significantly [26] to provide a higher resolution for creating such gradients. To enable conformal processing of a substrate with parallel HFCs, aperture-array probes could also be scanned over a substrate at an inclined angle (rotation around Z-axis) to enable an overlap between the areas processed with separate HFCs.

We further believe that using the methods presented in this paper, in combination with sequencing different liquids within each injection line, would be helpful for implementing a range of (bio)chemical assays on a surface. This could be done by the controlled insertion and removal of immiscible spacers, thereby minimizing Taylor dispersion [124]. Moreover, we believe it is conceivable to integrate the methods presented with techniques to perform local temperature alterations [142] to assist in performing efficient chemical reactions.

A limitation of the devices and methods presented is the relatively high consumption of reagents compared with that of on-bench protocols. An implementation of the discussed designs in probes made of plastics might allow the distance between the apertures in a slit-aperture design to be increased to several millimeters. This would increase the surface area the processing liquid interacts with before being re-aspirated, which would result in a more efficient usage of the injected reagents. Another approach towards efficient use of the processing liquids would be to create HFC with minimal dilution [120] in combination with liquid recirculation [30].

Horizontal probe heads enable the formation of radial HFCs and were used for rapid and point-wise sequential interactions at the mm-scale. We believe that the concept of rapid μ IHC might be either of direct diagnostic value for the bedside-analysis of tissue sections during surgery or be used to conveniently implement designs of experiments for the characterization of reagents, or for the optimization of larger scale diagnostic workflows.

In a research setting, the key use of the devices and methods presented for mm- to cm-scale interaction with a substrate lies in enabling multiplexing in all steps of an analysis which are performed in liquid environment. In a clinical environment, the short incubation times enabled by HFC of the processing liquids might allow the deployment of e.g. IHC analysis to be done during surgery, while the ability to acquire more detailed information on selected areas of interest can potentially enable a more targeted and more efficient analysis of tissue sections. We believe that the methods proposed here can enable novel, complex and dynamic (bio)chemical processes to be implemented on a range of biological substrates and for many applications.

4.6 Materials and Methods

4.6.1 Experimental section – vertical probe heads

Microfluidic probe platform. The platform comprised a scanning unit, a holder for the sample, a holder for the probe and a flow control unit (Figure S2). The scanning unit held two stages for X-Y positioning of the sample relative to the probe and another stage for Z-positioning of the probe over the sample (Zaber Technologies Inc., Canada). The entire scanning unit was placed on top of an inverted microscope (Eclipse TI-E, Nikon, Japan). The probe itself was mounted on a holder that allowed tilt adjustment of the probe relative to the sample. The flow control unit comprised reservoirs connected to the probe with 1/16 PEEK tubing (IDEX H&S, USA) and fluidic connectors (Dolomite microfluidics, UK). Vacuum or pressure was applied to the reservoirs using a pressure control device (Fluigent, France) (see Figure S3 for details on the simultaneous

injection of multiple reagents). Flow rates were measured in real-time (Fluigent, France), allowing the system to operate in a closed-loop feedback mode with constant flow rates. A detailed description of the platform, alignment procedure and operation can be found elsewhere [26].

Probe fabrication. The probe is a glass-Si-glass device with microchannels defined by photolithography and etched to a depth of 50 μm using deep reactive-ion etching (DRIE) on both sides of a double-side polished Si wafer. The microchannels were sealed by anodic bonding (1.3 kV, 475 $^{\circ}\text{C}$) of the Si wafer with BF33 glass wafers. Details of the fabrication process for two-layer Si/glass probes are described elsewhere [26]. To fabricate the three-layer probes used here, each side of the processed Si substrate was bonded with glass sequentially.

Finite-element modeling. We performed steady-state 3D simulations with COMSOL Multiphysics (version 4.2). Non-slip boundary conditions were defined on all surfaces and a Neumann boundary condition for flows across the virtual interface between the immersion liquid and the liquid underneath the apex of the probe. At each aperture, a Dirichlet boundary condition defined the flow. All fluids were set to be water (incompressible Newtonian fluid with a density of 998 kg/m^3 and a dynamic viscosity of 0.001 $\text{N s}/\text{m}^2$).

Immunohistochemistry protocol. Human breast-cancer tissue microarrays (TMA) (Novus Biologicals LLC, USA) were dried at 60 $^{\circ}\text{C}$ for 45 min, followed by removal of paraffin and gradual rehydration. A hydrogen peroxide block was applied prior to the heat-induced epitope retrieval (target retrieval solution pH 9.0, Dako A/S, Denmark). The TMA was cooled gradually to room temperature in the target retrieval solution, followed by a protein block. With the probe, local areas of the tissue section were exposed to the primary antibody (Ab) solution. The primary Ab solutions used were α -p53 and α - β -actin, both produced in mouse (both Sigma-Aldrich, USA), and were diluted to 25 $\mu\text{g}/\text{ml}$ in PBS. Rhodamine B was added to all antibody solutions at a concentration of 10 μM for flow visualization. For staining, we used enzymatically amplified staining with the chromogen 3,3'-diaminobenzidine (DAB) for bright-field visualization (mouse-specific HRP/DAB IHC Kit, Abcam plc, UK).

Bio-patterning and IgG-anti-IgG assay. A Si stencil (mask) was used to generate the protein patterns on the surface. The surface of the stencil was cleaned with air plasma (200 W, 2 min), then the stencil was placed on a sheet of Polydimethylsiloxane (PDMS) (0.25 mm, HT-6240, Rogers Corp., USA) supported by a microscope glass slide. The channels of the stencil were filled with a solution containing 50 $\mu\text{g}/\text{ml}$ IgG from rabbit serum (Sigma-Aldrich, USA), followed by 30-min incubation. After rinsing with BSA (1% in PBS), the stencil was removed. The PDMS sheet was then incubated with BSA (1% in PBS) for 15 min prior to treatment with the MFP. The liquid applied with the probe as processing liquid contained fluorescently labelled α -rabbit IgG at 25 $\mu\text{g}/\text{ml}$ and BSA (1% in PBS).

4.6.2 Localized IgG assay on a PDMS-surface

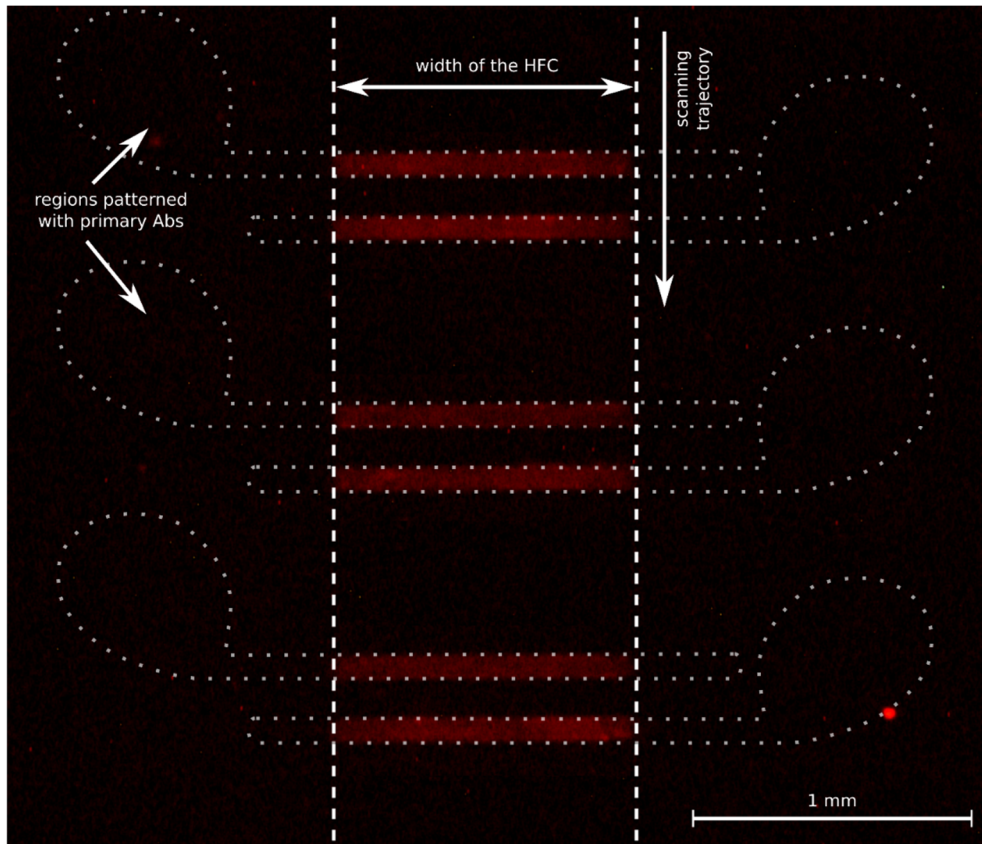


Figure 4.9: Localized patterning of a substrate using mm-scale HFC. A microfluidic stencil [30] was used to create a line-pattern of IgG from rabbit serum on a PDMS surface. A probe with slit-aperture design creating an HFC with a width of 1.2 mm was scanned perpendicularly to the line pattern ($Q_I = 6 \mu\text{l}/\text{min}$, $Q_I/Q_A = 1/5$, speed 0.02 mm/s, gap 40 μm) to expose only the center of the pattern to the processing liquid. The processing liquid in the HFC was PBS containing α -Rabbit IgG labelled with rhodamine B at a concentration of 150 $\mu\text{g}/\text{ml}$ and 1% of BSA.

4.6.3 Setup for localized processing of immersed surfaces

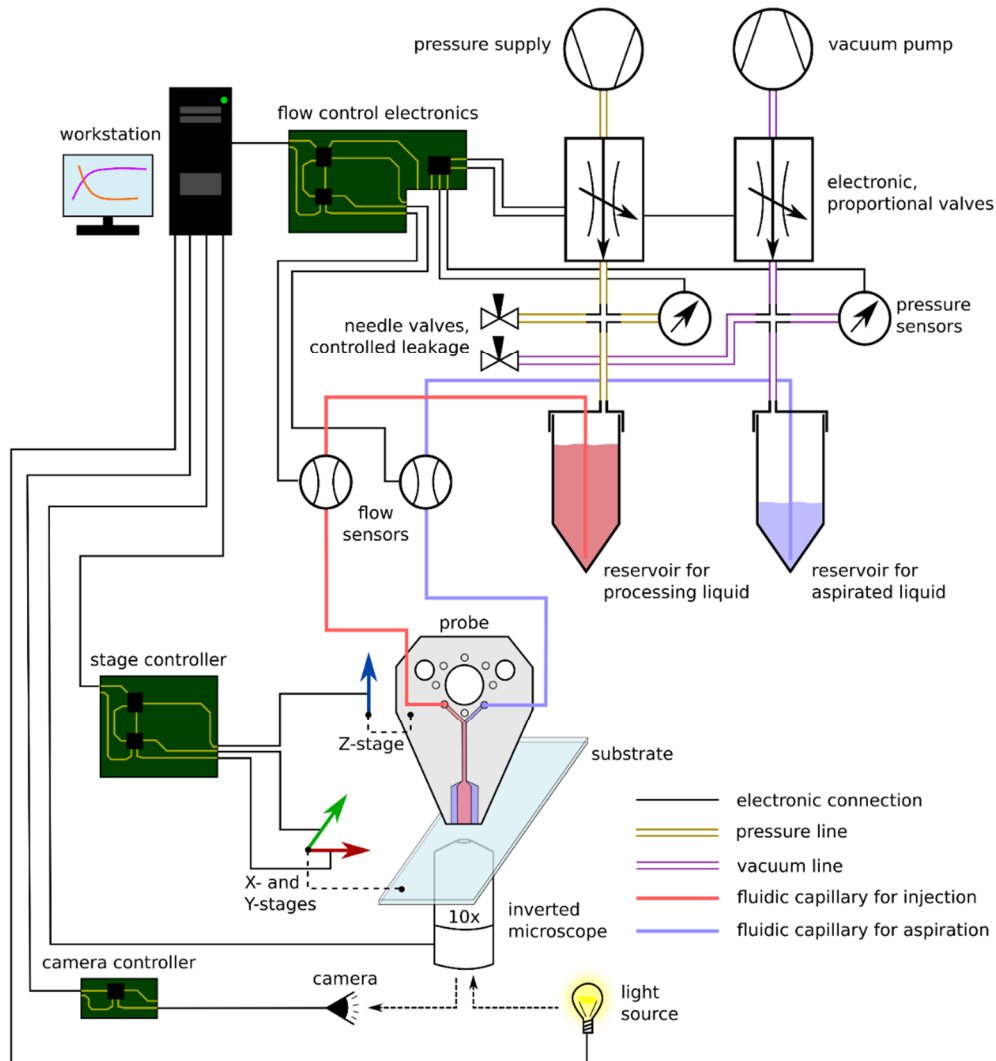


Figure 4.10: Schematic illustration of the setup. For activation of flows, the pressure or vacuum can be adjusted in the reservoirs connected to the probe. A stable adjustment of the pressure is possible, by regulating gas flow from a source with a proportional valve in combination with a controlled leakage to ambient to compensate for overshooting. Liquid flow is monitored by high precision flow sensors and the flow rates are used as feedback to adjust the pressure values in closed loop control. The substrate is supported by a stage that allows scanning in X- and Y-direction, while the probe is aligned with the optical axis of the microscope and can be moved in Z-direction for adjusting the gap between the probe and the substrate.

4.6.4 Reagent loading platform for multiplexing using aperture array designs

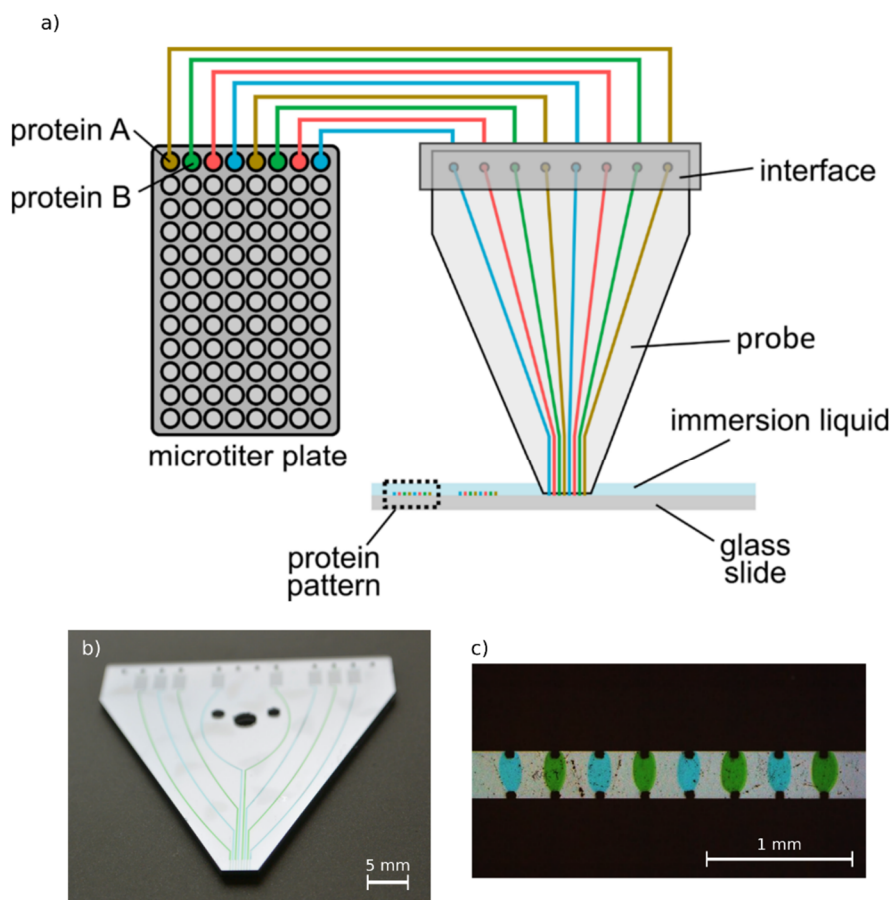


Figure 4.11: Sample loading and interfacing for probes with aperture-array designs. a) To allow for confinement of up to eight different processing liquids in parallel, the probe must be connected to a corresponding number of reservoirs individually. To enable simple loading and handling of processing liquids, we interfaced the aperture-array probe with 96-well microtiter plates: after loading of the processing liquids, the 96 well plate is inserted into a pressure chamber. The lid of the chamber holds eight capillaries, which upon closing is inserted into the wells containing the processing liquids. When the chamber is pressurized, the processing liquids are injected into the capillaries, which are interfaced with the probe via a 12-port linear connector (Dolomite Microfluidics Ltd., UK). b) Photograph of an aperture-array probe. Hydrodynamic resistors, for enabling operation in the ideal working range of the pressure control system, as well as fluidic connection ports are visible at the top end of the probe. c) Bright-field image of eight individual flows of processing liquids confined at the apex of an aperture-array probe. The processing liquids contain blue and green food dye for visualization.

4.6.5 Experimental section –rapid μ IHC

Sample preparation. MDAMB468-1510A cell block sections were purchased from AMS Biotechnology Europe (Massagno, Switzerland). A standard protocol was applied to the cell block sections to prepare the sample for the IHC experiment. This involved: deparaffinization, hydrogen peroxidase block, target retrieval and protein block. The prepared cell block sections were kept in PBS at 4 °C no longer than one day until used.

MFP system setup. Two glass slides were placed into the substrate carrier next to each other. This allowed adjusting the fluidic system to achieve stable flow confinements on a dummy glass slide, before then performing the actual experiment on the sample glass slide. The injection channels of the system were initially purged with colored liquids (diluted food colorant) until stable flow confinements were observed on the

dummy glass slide. The pressure settings for each channel were stored in the control software to enable quick switching between flow confinements with different colors.

Performing micro-IHC experiments. The MFP head was moved to the sample glass slide, which was covered with PBS, and parked at a safe distance (e.g. 15 mm) away from the cell block section. The gap distance was set to 75 μm . The reservoir tubes containing food colorant were replaced with tubes containing the reagents for IHC (primary antibody, secondary antibody and for some experiments streptavidin peroxidase and DAB substrate). The primary antibody (ab122898, anti P53) as well as the other IHC chemicals (Mouse specific HRP/DAB (ABC) Detection IHC Kit, ab64259) were purchased from Abcam (Cambridge, UK). Each injection channel was purged with the according IHC reagent until no residual food color could be observed. The pressure settings for stable flow confinements and switching between liquids were adjusted if needed. The MFP head was then moved to the X and Y zero position in relation to the cell block section (upper left corner of an imaginary square fitted around the circular cell block section). This starting point for the experiment was set to 0 for the X and Y axis in the control software. Rapid μIHC with varying incubation times of the reagents was performed by moving to designated coordinates over the cell block section and switching between the reagent injection channels while keeping the aspiration flow constant. After applying the reagents with the MFP, the sample was processed according to a standard IHC method. Depending on the number of reagents applied with the MFP, the cell block sections were incubated with streptavidin peroxidase and DAB substrate or only DAB substrate. No further treatment was needed for the cell block sections after scanning μIHC . Processed cell block sections were dehydrated and mounted using standard mounting medium and a coverslip.

Data analysis. An upright microscope was used to image the sections and color photographs were taken of each sample with 4x and 10x magnification. Quantification of the staining intensity was done using ImageJ. Features were extracted manually as it was considered sufficient for the conceptualization shown here. The individual images were analyzed the following: (1) at least 25 nuclei per spot were selected with the freehand selections tool and the mean gray value calculated from all areas, (2) the same procedure was done to calculate the mean gray value of the cytoplasm of the cells, where manually at least 25 regions per spot were selected for analysis. The normalized stain intensity per spot was then determined by subtraction of the two values.

Chapter 5 Fluidic bypass structures for improving the robustness of liquid scanning probes

The content of this chapter is based on the pre-print version of below listed research article, which was published in 2019 in *IEEE Transactions on Biomedical Engineering (IEEE TMBE)*, and is reproduced here with minor modifications with permission from the Institute of Electrical and Electronics Engineers. This article was selected as a feature article for the 2019 September issue of *IEEE TMBE*.

D. P. Taylor and G. V. Kaigala, "Fluidic bypass structures for improving the robustness of liquid scanning probes," *IEEE Transactions on Biomedical Engineering*, **2019**, doi: 10.1109/TBME.2018.2890602

5.1 Abstract

We aim to improve operational robustness of liquid scanning probes. Two main failure modes to be addressed are the leakage of processing liquid due to an obstruction of its flow path and a deviation from the desired gap distance between probe and sample. Therefore, we introduce a multi-functional design element, a microfluidic bypass channel, which can be operated in dc and in ac mode, each preventing one of the two main failure modes. In dc mode, the bypass channel is filled with liquid and exhibits resistive behavior, enabling the probe to passively react to an obstruction. In the case of an obstruction of the flow path, the processing liquid is passively diverted through the bypass to prevent its leakage and to limit the build-up of high pressure levels. In ac mode, the bypass is filled with gas and has capacitive characteristics, allowing the gap distance between the probe and the sample to be monitored by observing a phase shift in the motion of two gas-liquid interfaces. For a modulation of the input pressure at 4 Hz, significant changes of the phase shift were observed up to a gap distance of 25 μm . The presented passive design element counters both failure modes in a simple and highly compatible manner. Liquid scanning probes enabling targeted interfacing with biological surfaces are compatible with a wide range of workflows and bioanalytical applications. An improved operational robustness would facilitate rapid and widespread adoption of liquid scanning probes in research as well as in diagnostics.

5.2 Introduction

Akin to scanning probes, such as atomic force microscopes (AFM), and scanning tunneling microscopes (STM) used for applications in e.g. metrology, liquid scanning probes enabling localization of liquids on biological samples, are poised to be increasingly used in biomedical research and medical diagnostics [8], [143]. Liquid scanning probes enable local interaction with standard biological substrates, such as Petri dishes, microtiter plates and microscope glass slides. By scanning the probe across a substrate, distinct areas of interaction can be selectively chosen and interrogated.

Different variants of liquid scanning probes have been developed to localize liquids on specific regions on surfaces without cross-contamination between neighboring areas of interaction. Demonstrated implementations e.g. are based on the delivery of reagents in a second, aqueous phase to reduce mixing [103], or the release of minute amounts of reagents [9], [135]. Another approach is to create flow patterns in the gap between the liquid scanning probe and the sample by injection and simultaneous re-aspiration, to confine the flow of a reagent within a so-called hydrodynamic flow confinement (HFC). Associated methods impose no specific constraints on the properties of the applied liquids and are commensurate with the length-scales of standard substrate formats, as they enable interaction with areas ranging from tens of μm^2 to several cm^2 [144]. This principle is applied in e.g. the microfluidic fountain pen, the multifunctional pipette and the microfluidic probe (MFP) [23]–[25], [93], [145].

The MFP allows to establish a flow confinement of a liquid reagent (to as low as a few pLs) on a surface with a footprint at the scale of $100\ \mu\text{m} \times 100\ \mu\text{m}$ (see Figure 5.1b). During operation, a probe head with a flat apex is positioned at a distance of about $10\text{--}100\ \mu\text{m}$ from a sample. From apertures at the center of the apex, a processing liquid can be injected and re-aspirated together with some surrounding immersion buffer, resulting in an HFC of the processing liquid on the sample surface. The use of the MFP and its capability for spatial and temporal multiplexing of liquids on surfaces has been demonstrated in the form of local multiplexed immunohistochemistry on tissue sections, local lysis of adherent cells and the creation of protein microarrays [8], [26], [30], [143], for example.

A key aspect limiting the transition of these liquid scanning probes to the life-sciences, biology and medicine is their lack of operational robustness. This lack of robustness is mainly caused by the slow or delayed detection of the occurrence of a failure by the peripheral operating instrumentation and monitoring units (see Figure 5.1a). This can result in significant damage to the applied probe and the sample being probed. In this paper, with the exemplary example of the MFP, we identify two main operational failure modes of liquid scanning probes that rely on simultaneous injection and aspiration of liquids. As re-aspiration of a processing liquid is required in several scenarios, such failure modes can occur in scanning electrochemical microscopy (SECM) push-pull probes [146] and AFM-based probes used with liquids [147].

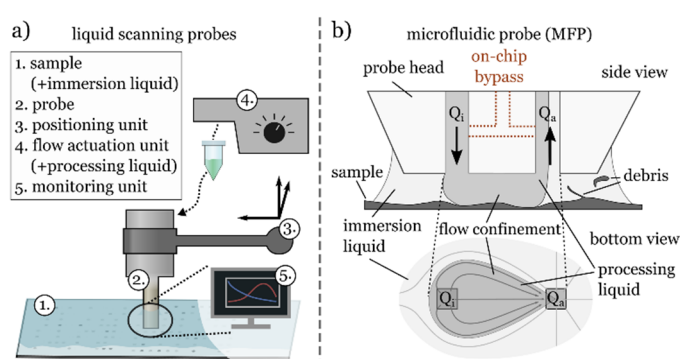


Figure 5.1: Liquid scanning probes enable interfacing with immersed biological samples. a) Liquid scanning probes functionally comprise five components. b) The probe head of a microfluidic probe has a flat apex with at least two apertures. The probe head operates in proximity ($\sim 20\ \mu\text{m}$) to the surface of an immersed sample. By injection of liquid from the first aperture and re-aspiration at a higher flow rate from the second aperture, a reagent can be confined hydrodynamically to a specific region of the sample.

The strategies outlined here are hence broadly applicable to a range of liquid scanning probes. We here propose a design element, a microfluidic bypass channel, which can be operated in two configurations to prevent

these failures by either enabling a passive response of the probe, or by extending capabilities of the monitoring unit to allow for rapid feedback.

5.3 Failure modes of liquid scanning probes and strategies to avoid them

In liquid scanning probes, the fluidic structures and the instrumentation required to operate the probes are simple, thus failures during operation largely result from the properties of the processing liquids and samples (e.g. agglomeration of solutes) and from improper handling (e.g. a misaligned placement of a sample). As biological samples and liquids can contain particles and bubbles and user-interactions are naturally prone to variation, addressing the problem of robustness is key to enable a wide-spread use of liquid scanning probes. We identified two main types of failure modes: a) the obstruction of one or more apertures resulting in a leakage of the processing liquid or damage to the components of the setup, and, b) a deviation from the desired gap distance resulting in an inhomogeneous interaction with the sample. To mitigate the impact of these two main failure modes, we introduce the concept of a fluidic bypass structure between the injection and the aspiration channel. We make use of the analogies between fluidic and electrical circuits to illustrate and analyze the behavior of the introduced concepts. In the following designs and their analysis we assume that the flow of liquids is actuated by the setting of a controlled pressure level e.g. in a reservoir connected to a microfluidic channel. We emphasize that the presented concepts are equally applicable when imposing the flow rate with e.g. a syringe pump.

5.3.1 Leakage of processing liquid due to obstruction of apertures

Partial or complete obstruction of one or several apertures can be caused by either local elevations in the sample topography, or by particles and bubbles contained in the processing or the immersion liquid. As particles and small bubbles tend to follow the flow towards the aspiration aperture, this aspiration is likely to be clogged. During operation of the MFP and other liquid scanning probes that rely on re-aspiration of a processing liquid, an obstruction of the flow path between the injection and the aspiration aperture reduces the effective re-aspiration of the injected processing liquid. This can easily result in a leakage of the processing liquid into the surrounding immersion buffer and a contamination of regions of the sample, which should not have been in contact with the processing liquid. Figure 5.2a illustrates this for partial obstruction of either the injection or the aspiration aperture. This failure mode is especially problematic in using a device with several parallel flow confinements [144]. While the probe head itself might be designed as a single-use device and be replaced in the case of an obstruction, samples often are scarce and a leakage of corresponding liquid might result in considerable damage. Further, the obstruction of an aperture may lead to the build-up of increased pressure levels within the fluidic system and result in damage to hardware components, typically capillary-chip-interfaces, as well in leakage of the processing liquid in affected parts of the instrument. In the case where the aspiration aperture is used for picking objects from a surface, such as cells, from a surface, the build-up of high differential pressure levels might result in damaging those objects [147]. To the best of our knowledge, no strategies have been demonstrated to alleviate problems related to obstruction of channels.

Here we present a fully passive solution based on a liquid filled bypass channel between the injection and the aspiration channel in the probe head (Figure 5.2b). An additional channel, the compensation channel, is connected to the bypass channel. Buffer is injected through the compensation channel at constant pressure to equalize the pressure on both sides of the flow-path element R_4 when the probe is positioned at the desired gap distance. If an obstruction of one or both apertures occurs, the differential pressure across the

bypass increases, the pressure across element R_4 is not balanced and the flow of injected reagent is redirected through the bypass.

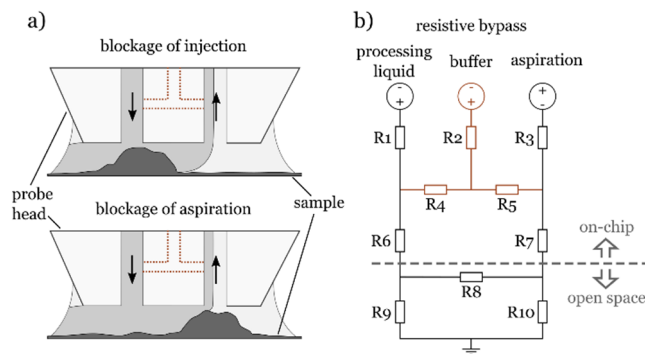


Figure 5.2: Failure mode caused by obstruction and solution based on a resistive bypass. a) A blockage of either the injection or the aspiration aperture might result in a leakage of the processing liquid into the immersion liquid. b) Equivalent electrical model of a probe head with resistive bypass to mitigate failure due to obstruction of apertures.

5.3.2 Variations of the gap distance between probe and sample

The second failure mode is induced by a deviation from the desired gap distance between the probe and the sample. Such a deviation is caused by scanning of the probe across a sample with variable topography, or by a mechanical misalignment between the scanning-plane of the probe and the surface of the sample. For given injection and aspiration flow rates, the interaction with the sample surface is specific for a gap distance [25], [148]. For small gap distances ($<5 \mu\text{m}$ for the MFP), the probe and the sample might crash, while for large gap distances ($>30 \mu\text{m}$ for the MFP, depends on the design of the probe and the ratio of aspiration/injection flow), the injected processing liquid might not be in contact with the sample surface (see Figure 5.3a). In order for the HFC to interact with a sample in a repeatable manner, as required for e.g. assays with optical readout, working at a known and constant gap distance is crucial.

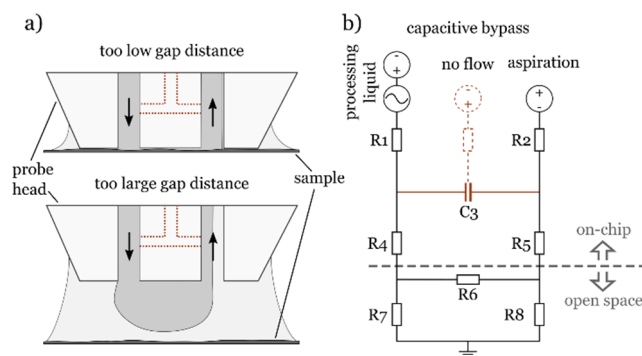


Figure 5.3: Failure mode caused by wrong gap distance and solution based on a capacitive bypass. a) In the case of a low gap distance, the probe might scratch and damage the sample. In the case of larger gap distances, the processed areas at the surface are not well defined or the processing liquid might not be in contact with the sample b) Equivalent electrical model of a probe head with capacitive bypass to mitigate failure due to obstruction of apertures.

AFM-based liquid scanning probe and probes related to scanning ion conductance microscopy (SICM) or scanning electrochemical microscopy (SECM) are readily suited for monitoring the gap distance by assessment of the deflection of a cantilever in the first case, or by measurement of a current between electrodes

in the case of the latter ones. In contrast, for purely microfluidic liquid scanning probes, continuous monitoring of the gap distance poses a challenge, as many available approaches have limited compatibility with bio-analytical applications: optical measurement techniques, for instance, depend on the optical properties of the sample and are therefore not compatible with many assays. A measurement of electrical current between electrodes, as employed in SECM, imposes conditions on the applied buffer systems and requires the implementation of electrodes, which also limits the types of compatible applications [10], [20], [138]. A measurement of the hydraulic resistance of the gap between the probe and the sample requires a relatively high flow rate (above 100 $\mu\text{l}/\text{min}$) to obtain a quantifiable signal [149]. The sample surface thus is exposed to significant shear stress, which is incompatible with e.g. assays on surface-adherent cells. Other approaches are not commensurate with the range of gap distances of 5 μm to 100 μm , at which purely microfluidic liquid scanning probes are typically operated: AFM-related probes usually are operated at gap distances smaller than 1 μm [9], while e.g. a measurement of distances in a liquid environment using ultrasound waves has a limit of resolution at the scale of 30 μm [150].

We here present a method of measuring the gap distance between a liquid scanning probe and a sample based on the above introduced bypass channel, which provides a suitable range of measurement up to 25 μm and is well compatible with a wide range of bioanalytical assays. For this, we introduce a bubble of compressible gas into the bypass channel (see Figure 5.3b) to change its behavior from purely resistive to capacitive. To stably hold the bubble in place, the geometry of the bypass channel is adapted to form a so-called coupling cavity. The pressure inside this coupling cavity can be adjusted via the compensation channel.

If the injection of reagent through the injection channel is now modulated at a certain frequency, the transduction of this modulation to the aspiration channel depends on the fluidic impedance of the fluidic network formed by the channels in the probe and the gap between the probe and the sample. A change in gap distance thus induces a change in phase shift of the transduced pressure signal. This phase shift is measurable with standard and simple imaging equipment, such as cell-phone cameras.

5.4 Theory

We designed and analyzed the bypass structures by drawing analogies between electric and fluidic circuits and making use of principles of voltage distribution across networks of electrical elements and the superposition of linear responses [151], [152].

5.4.1 Resistive bypass – dc mode

To study behavior of a resistive bypass, we performed a steady state nodal voltage analysis of the corresponding fluidic network (see Figure 5.4a). We assume that flow is driven by three ideal pressure sources connected to the injection, the aspiration and the compensation channel, respectively. Following the Norton-theorem [153], all three ideal pressure sources are converted to ideal flow sources. For the combination of flow-path elements characterized in Figure 5.4d, representing a standard probe design with resistive bypass, we numerically solved the system of linear equations to find the relative pressures at the nodes $\phi_1 - \phi_5$. With knowledge of the pressure drop across each of the involved flow-path elements, the actual flow through each element can be computed (see section 5.7.2 for details on the calculation of hydraulic resistances).

As shown in Figure 5.4c, during normal operation, there is no flow across the first section of the bypass (R_4) and all the processing liquid flows through the injection aperture into the HFC and is then re-aspirated. There is a small inflow across R_9 , as immersion buffer is drawn into the gap from either side, ensuring confinement

of all the injected flow of processing liquid. To assess the response to obstruction of either one of the two apertures, the resistance of the flow-path element linked to either the injection aperture (R_6) or the aspiration aperture (R_7) was increased across two orders of magnitude. In response to an obstruction of the injection aperture, the nodal potential ϕ_1 increases and ϕ_1 and ϕ_2 are no longer equal. Consequently, a fraction of the injected processing liquid flows through the bypass, thereby reducing the effective injection flow of processing liquid into the gap. The effective injection flow of processing liquid further decreases due to the higher resistance of the obstructed injection flow path. The more severe the obstruction of the injection aperture, the more processing liquid passes through the bypass and the less flow enters the gap. In a scenario without a bypass channel, only the second effect, the reduction of the injection flow due to an increased resistance, occurs.

In the case of an obstruction of the aspiration aperture, in a probe with a resistive bypass, the nodal potentials ϕ_2 and ϕ_3 drop and again a share of the injected processing liquid flows through the bypass. As the negative relative pressure applied to the aspiration channel in absolute numbers is higher than the positive relative pressure applied to the injection channel, the pressure drop building up across the bypass channel in the case of an obstructed aspiration aperture can be higher, accordingly. If the value of R_7 exceeds a certain threshold, all injected processing liquid flows through the bypass channel and flow across R_6 is inverted, as immersion buffer is additionally drawn into the injection aperture (obstruction factor of 30 in the discussed design, see Figure 5.4b).

In Figure 5.4b, the flow across R_6 in the case of an obstruction of either the injection (faint colors) or the aspiration aperture (intense colors), normalized by the undisturbed flow across R_6 , is plotted versus a factor of obstruction by which either R_6 or R_7 are multiplied. If there is an obstruction of the injection channel, in a probe with a resistive bypass, the reduction of the flow across R_6 is over 2-fold more pronounced than in a design without a bypass.

The benefits of a resistive bypass becomes more apparent for the case of an obstructed aspiration aperture: for a design without a bypass, the injection flow into the gap remains unaffected and processing liquid leaks into the surrounding immersion liquid. In a probe with resistive bypass, in contrast, leakage of the processing liquid is completely avoided.

5.4.2 Capacitive bypass – ac mode

For probes with capacitive bypass elements, the network analysis facilitates the design and operation by highlighting the correlations between the applied relative pressure levels, the modulation frequency, the internal volume of the coupling cavity, the gap distance, and the resulting phase shift between the input modulation and the modulation transferred to the aspiration channel. Analysis of dc (constant flow) and ac (time-dependent flow) characteristics is performed separately and the results are superimposed (see Figure 5.4e). Further, as the complex impedance is required to describe the frequency dependent properties of e.g. a capacitor (see section 5.7.2), all calculations are performed in complex space. There are two pressure sources relevant for the dc analysis: the first one supplies a constant positive relative pressure to the injection channel, whereas the second provides a constant negative relative pressure to the aspiration channel. In analogy to the above analysis of the resistive bypass, those two ideal pressure sources are converted to ideal flow sources. As there is no net current across the bypass (Z_3), this flow-path element is irrelevant for the dc analysis. Again, a system of linear equations is solved to find the dc components of the relative pressures at the nodes $\kappa_1 - \kappa_4$. For the ac analysis, the only source to be considered is a cos-type ac pressure source

connected to the injection channel, the two dc sources are treated as short circuits. After conversion of this source to an ideal flow source and the solution of the corresponding system of linear equations, one obtains the relative amplitudes and phase shifts of the pressure modulation at the nodes $\kappa_1 - \kappa_4$.

This data, superimposed with the dc distribution of pressure across the network, allows us to compute the flow across any of the flow path-elements (assuming the system has equilibrated). On the basis of the described ac model, we analyzed how strongly a change in gap distance between probe and sample would change the phase difference between κ_1 and κ_2 and how well this effect would be observable. The pressure amplitude of the modulation generated by the ac source linked to the injection channel is transferred to the node κ_2 at a factor of about 10^{-2} . Assuming input modulation amplitudes smaller than 100 mbar, a direct measurement of the transferred pressure signals using standard pressure sensors (resolution of ~ 0.25 mbar) would result in noisy signals. We thus chose to monitor the movement of the gas-liquid interface between the gas in the coupling cavity and the liquid in the aspiration channel, to which we refer as the rear interface (see Figure 5.6c), to track the modulation of the pressure in the aspiration channel. The gas-liquid interfaces between the gas in the coupling cavity and the liquid in the injection and the aspiration channel reside in tapered structures, so that the radius of curvature of each interface is free to adapt to the corresponding differential pressure. Consequently, the acceleration of the rear interface is proportional to the pressure difference between the inner volume of the coupling cavity and the pressure at κ_2 . We therefore assume that the movement of the rear interface exhibits the same relative phase shifts as the pressure at κ_2 itself.

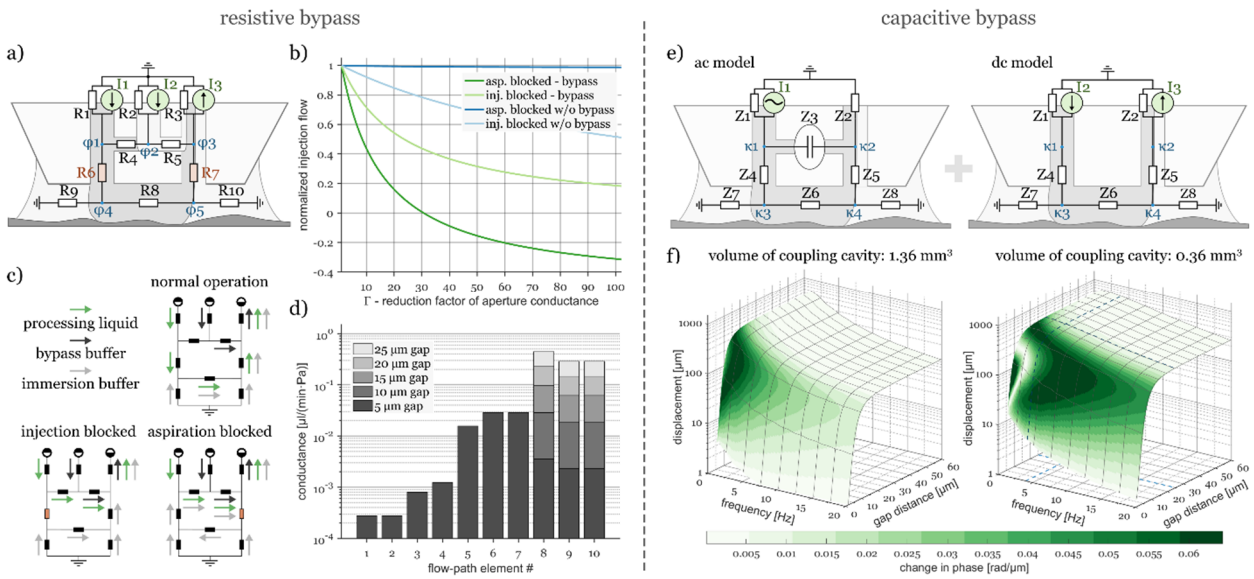


Figure 5.4: Analysis of microfluidic probe heads with resistive or capacitive bypass structures. a) Equivalent electrical model of a microfluidic probe head with a resistive bypass. b) Plot of normalized flow through the injection aperture plotted over the factor of aperture-blockage for a device with resistive bypass (green) and a device without bypass (blue). The dynamic response of a probe head with resistive bypass to the event of an obstruction significantly reduces the risk of leakage of processing liquid. c) Flow path of liquids in a probe head with resistive bypass during normal operation and blockage of either the injection or the aspiration channel. d) Conductance of the individual flow-path elements of an exemplary probe head with resistive bypass. e) Equivalent electrical model of a microfluidic probe head with a capacitive bypass. The ac and dc behavior of the system was characterized separately and superimposed. f) Transfer of a sinusoidal pressure modulation from κ_1 to κ_2 in two designs featuring coupling cavities of different volumes.

Based on the computed, time-dependent pressure levels at κ_1 and κ_2 , as well as the geometrical boundary conditions and the properties of the involved fluids, we estimate the movement amplitude of the rear

interface for a given combination of gap distance and modulation frequency (see section 5.7.6). The surface plots in Figure 5.4f display the estimated movement amplitudes for a range of modulation frequencies and gap distances, assuming a reasonable input modulation amplitude of 40 mbar. The movement amplitudes of the rear interface drop from over 100 μm to less than 20 μm , as the gap distance becomes smaller than 5 μm . This is due to the decrease of the relative pressure at κ_2 occurring when the probe is close to the surface of the sample, which results in an increased pressure drop across the rear interface. Under these conditions the rear interface adapts a relatively small radius of curvature and the changes induced by the modulation result in smaller relative changes of the interface position. Our model also predicts that the movement amplitudes get smaller for higher modulation frequencies. This occurs, because the analyzed network acts as a high-pass filter and more efficiently transfers the pressure modulation to the aspiration side at higher frequencies. A better transfer of the pressure modulation in turn results in a lower differential pressure across the coupling cavity and therefore in less movement of the gas-liquid interfaces. This effect shifts to higher frequencies as the volume of the coupling cavity is reduced. The color of the surface plots in Figure 5.4f encodes the change in phase shift between the pressure levels at κ_1 and κ_2 for a change of the gap distance of 1 μm . Regions in which changes of the gap distance induce a high change of the phase shift are marked by more intense color. It is clearly observable that the changes in phase shift are more pronounced across a wider range of frequencies and gap distances for smaller coupling cavities. Movement amplitudes in the range of 100 μm can be resolved well with e.g. low-cost optical equipment (see subsequent section). Our model therefore suggests that a simple optical tracking of the rear interface should allow an observation of relative changes of the phase shift induced by changes of the gap distance for gap distances above 5 μm , with higher movement amplitudes to be expected for low frequencies.

5.5 Results and Discussion

5.5.1 Resistive bypass for compensation of obstructions of apertures

To test and demonstrate the functionality of the resistive bypass structures, we added food colorant to the liquids used in the experiment. This allows the tracking of specific liquids within the fluidic network. The processing liquid was colored green, the immersion buffer blue and the bypass buffer, which is injected through the compensation channel, was left transparent. Figure 5.5a shows a photograph of a probe with a resistive bypass. The conductance of the individual flow-path elements of this design is displayed in Figure 5.4d. The major share of the overall resistance of the bypass is attributed to the first section of the bypass (R_4), in order to limit the flow of buffer from the compensation channel into the injection channel in situations when the distance between probe and sample is larger than the desired gap distance.

During normal operation (see Figure 5.5b), the processing liquid (green) flows through the injection channel (left hand side in Figure 5.5b) and is re-aspirated together with some of the surrounding immersion liquid (blue) through the aspiration channel (right hand side in Figure 5.5b). There is no flow across the first section of the bypass channel (R_4) and only flow of buffer (transparent) in the second section of the bypass channel (R_5).

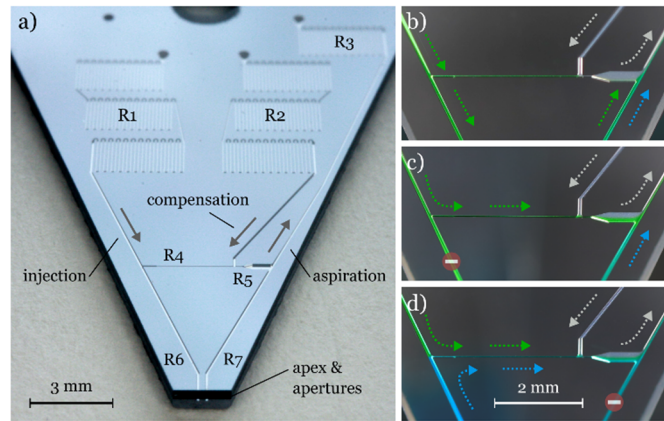


Figure 5.5: Resistive bypass for dc configuration. a) Probe head with channels etched in silicon. b) Normal operation: no flow across first section of the bypass, only flow of bypass buffer through second half of bypass. c) Complete obstruction of the injection aperture: processing liquid (green) flows through the bypass. d) Complete obstruction of aspiration aperture: immersion liquid (blue) is pulled into the injection aperture and through the bypass together with the processing liquid.

We obstructed the apertures one after another by approaching the probe head towards a slab of PDMS of 250 μm thickness, which we positioned on the microscope glass slide that served as the sample surface in the described experiments. By centering the apex of the probe on the edge of the slab of PDMS, one aperture could be blocked selectively while leaving the other one unaffected.

If there is an obstruction of the injection aperture, flow in the injection channel starts stagnating and the relative pressure in the injection channel increases. Consequently, the total pressure drop across the bypass channel increases and the injected processing liquid is partially redirected through the bypass channel (see Figure 5.5c). The probe can be brought in a full contact with the slab of PDMS and then be retracted subsequently without processing liquid leaking into the surrounding immersion liquid. In the case of a total obstruction, all injected processing liquid is redirected through the bypass.

When bringing the aspiration aperture gradually closer to the surface of the slab of PDMS, the aspiration flow across R_7 drops and the relative pressure in the aspiration channel gradually decreases. Again, this results in a higher total pressure drop across the bypass and a partial re-routing of the flow of injected processing liquid through the bypass channel. If the obstruction of the aspiration aperture is severe, all injected processing liquid is redirected through the bypass channel together with some immersion buffer, which enters the injection channel through the injection aperture (see Figure 5.5d). Also the aspiration aperture can be brought into complete contact with the PDMS obstacle and then be retracted again without leakage of processing liquid into the immersion buffer.

5.5.2 Capacitive bypass for continuous distance sensing

Fig. 6A depicts the probe used for demonstrating the concept of measuring the gap distance by observing the phase shift between the modulation of pressure in the injection and the aspiration channel. The coupling cavity has two tapered regions in order to let the front and the rear interface freely adapt to the differential pressure that drops across them [124]. The tapered region hosting the front interface is designed with a larger angle of inclination, as the differential pressure across the front interface is lower and this interface therefore adapts to larger radii of curvature than the rear interface. The drain channel and the probing channel did not have any function in the described experiments.

On the basis of the above considerations, we chose a probe design with a relatively small coupling cavity with a volume of 0.36 mm^3 and a modulation frequency of 4 Hz. This modulation frequency was found to be a good trade-off between resulting signal amplitudes, observable changes of the phase shift and the detectability of the signal with respect to noise from the environment. For tracing the phase shift between the pressure modulation in the injection channel and the pressure modulation in the aspiration channel, we decided to track the movement of the front and the rear interface using a video camera. By inferring the phase of the excitation signal and the transduced signal from the same video, we circumvent the problem of having to synchronize signals from multiple measurement devices.

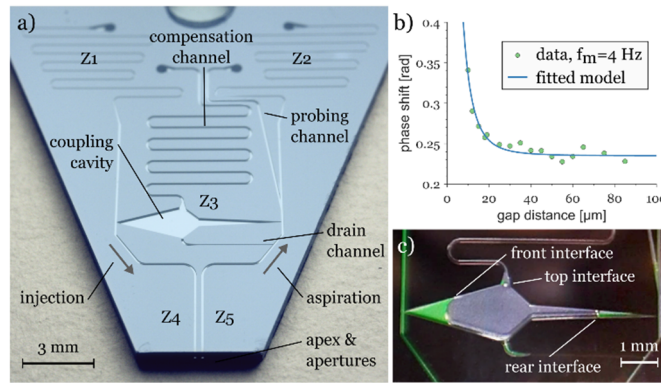


Figure 5.6: Capacitive bypass for continuous monitoring of the gap distance. a) Probe head with channels and capacitive bypass etched in silicon. b) Differential phase shift between the movement of the front and the rear interface recorded at 4 Hz (dots) and fitted theoretical model (line). c) Air-filled coupling cavity during the experiment.

We set the relative pressures in the reservoirs such that the mean injection flow rate was $3 \mu\text{l}/\text{min}$ and the mean aspiration flow rate $9 \mu\text{l}/\text{min}$. We then recorded the movement of the front and rear interface for 5 s at a given gap distance, to integrate over 20 modulation periods. For gap distances below $25 \mu\text{m}$, we randomly chose the order of the measurement points, to exclude hysteresis effects. The measured relative phase shifts between the front and the rear interface show a clear correlation with the gap distance. A change in phase shift is traceable up to gap distances of about $25 \mu\text{m}$ under the described experimental conditions. This covers the typical operating range during MFP experiments. In Figure 5.4f we highlighted the chosen experimental conditions and the observed measurement range with dashed lines in the corresponding surface plot of the modulation transfer function. The observed measurement range is in good agreement with the theoretical prediction.

In order to fit the analytical model to the recorded experimental data, two modifications have to be made. The first modification is required, because the contact angle between the materials the probe is made of and water is smaller than 90° . As a consequence, liquid wets the inner walls of the coupling cavity, which gives rise to a bypass flow of liquid through the coupling cavity [29]. This has to be taken into account by adding a resistive element to Z_3 in parallel (see section 5.7.7). A second modification is required, as in the actual experiment there are parasitic capacitances spread across the fluidic network. We take these into account by adding a capacitive element in parallel to Z_2 . By treating the properties of those additional elements as free fit parameters, the model can be fitted to the experimental data (see Figure 5.6b). To fit the experimental data, the value of the resistive element acting in parallel to the coupling cavity is estimated to be $1.25 \cdot Z_4$ and the sum of all parasitic capacitance in the network is estimated to be 1.23 times higher than the capacitance of the coupling cavity, corresponding to a volume of $0.44 \mu\text{l}$. The values of these two fit parameters do not conflict with any aspect of the physical setup and are intuitively reasonable. For further refinement of the

model, one might consider taking into account the dampening effects of viscous shear stress on the motion of the gas-liquid interfaces.

5.6 Conclusion and Outlook

We introduced a design element, a microfluidic bypass channel, which significantly improves the operational robustness of liquid scanning probes relying on re-aspiration of a processing liquid. The bypass channel can be operated in two configurations, each addressing one of the two main operational failure modes: in the dc mode, the bypass channel enables the fluidic network to intrinsically react to an obstruction by rerouting the flow of processing liquid. While not countering obstructions per se, this mechanism prevents leakage of the processing liquid into the immersion liquid and thus helps to protect the integrity of precious samples. In the ac mode, the bypass enables continuous monitoring of the gap distance without the need for sophisticated sensing equipment and without adding constraints on the performed experiments. Even though the ideal geometry of the bypass channel is different for each mode, a bypass designed to be used in ac mode can be used just as well in dc mode.

While the performance of the bypass in dc mode fully meets the requirement of preventing leakage of processing liquid into the immersion liquid, if one or several apertures are obstructed, we envisage that monitoring of the gap distance in ac mode could be further improved. The resulting range of measurement from 5 μm to 25 μm could be enhanced by adding hydrophobic patches to the coupling cavity, to suppress its resistive behavior. Also, additional capacitive flow-path elements could be added to obtain e.g. local extrema of the phase transfer function at specific gap distances. Further, a higher resolution in tracking the interface positions by means of e.g. electrode arrays, or optical line sensors would increase the range of operation in terms of gap distance and modulation frequency and help to speed up data acquisition and analysis.

We further envisage that the dc and ac functionality can be combined to directly enable leakage free operation at a constantly monitored gap distance: the differential pressure building up due to an obstruction could be employed to displace the gas in the coupling cavity and open up a resistive flow-path for internal bypassing of the processing liquid. The action of such a design element would be fully reversible and repeatable, as the gas volume would move back to its original position and close the bypass flow path for the processing liquid upon normalization of the differential pressure levels.

Bypass elements might also be used for rapid switching between different processing liquids [27]. In the context of more specific applications, the functionality of a fluidic bypass could be enhanced with additional functional elements, as e.g. spheres and bi-stable membranes. Such functional elements could open or close specific flow paths depending on the differential pressure dropping across the bypass. This would enable the probe to react to certain events with specific actions, without the need for any sensing or control infrastructure.

The presented concepts will help to improve the operational robustness, applicability and versatility of liquid scanning probes relying on the re-aspiration of liquid, while being compatible with a wide range of device concepts and bioanalytical applications. We hope the presented structures and methods help to pave the way for a reliable, long-term operation of such probes in diagnostic and analytical applications.

5.7 Materials and Methods

5.7.1 Experimental section

Probe heads and experimental platform. The MFP platform consists of five basic components: a sample holder with a sample covered by immersion liquid, a probe head, an XYZ positioning system to position the probe accurately relative to the sample, an imaging system, and a liquid flow actuation system. The probe can be made from various materials to be suited for a specific application. In the discussed case the probe is a silicon glass device [26]. Channel structures were photo-lithographically defined and then etched into the silicon at a depth of 100 μm using deep reactive-ion etching (DRIE). Subsequently, the silicon wafer was anodically bonded to a BF33 glass wafer (1.3 kV, 475 $^{\circ}\text{C}$), to seal the channel structures and single probes were then obtained by dicing. After dicing, the apex of the probe was lapped and polished on a wafer polishing tool (LP50, Logitech, UK) to obtain a well-defined and smooth surface. The positioning system consists of three linear stages (Zaber Technologies Inc., Canada) with a positioning resolution of 0.05 μm . The sample can be scanned in the XY-plane relative to the probe, while the probe itself moves only along the Z-axis, in order to stay aligned with the optical axis of the microscope. Imaging of the HFC is performed from underneath, through a transparent sample, using an inverted microscope (here: Lumascope LS620, Etaluma Inc., USA). A dye, e.g. fluorescein, can be added to the processing liquid to facilitate the visualization of the HFC. The tubing (1/16 FEP tubing, IDEX H&S, USA) is connected to the probe by a circular microfluidic connector (Dolomite Microfluidics, UK). Each fluidic channel is connected to a fluidic reservoir, in which the relative pressure is controlled using a pressure control system (EZ-Flow, Fluigent SA, France). Only DI water was used as liquid in the described experiments. For better contrast, food colorant and fluorescein were added, as needed. We used a microscope glass slide as a dummy-sample. The glass slide had 250 μm thick slabs of PDMS on it, which allowed us to selectively obstruct either the injection or the aspiration aperture.

Experimental setup for evaluating the capacitive bypass. In order to modulate the relative pressure in the reservoir connected to the injection channel in the experiments on the capacitive bypass, the reservoir was connected to a 2/3-way switch valve (24 V solenoid valve, Neptune Research & Development Inc., USA). The valve linked the reservoir to two gas-filled buffer containers with a volume of 0.5 liters each, one supplying positive relative pressure and the other one negative relative pressure (see section 5.7.5). The pressure in the buffers was controlled by a pressure control system (EZ-Flow, Fluigent SA, France). The buffers were required to prevent an interference between the alternating relative pressure in the reservoir linked to the injection channel and the pressure control system, which is configured to maintain a constant pressure at its output ports. The 2/3-way valve was supplied with power from a laboratory power supply and connected to ground across a bipolar transistor, which was switched by a square-wave signal generated with a waveform generator (33511B, Keysight Technologies, USA). To record videos of the coupling cavity at a frame rate of 240 fps during operation of the MFP, we used a Galaxy S7 cellphone (Samsung Electronics, South Korea) with a 20 \times clip-on lens. Interface movements could be reliably tracked down to movement amplitudes of about 80 μm .

Analytical modelling. The described systems of linear equations were solved using Matlab (MathWorks, Inc., USA). Also, the interior-point optimization routines used to find suitable input pressure levels, as described in section 5.7.4, were setup and run in Matlab.

Image processing and measurement of the phase shift. To assess the phase shift between κ_1 and κ_2 in probes with a capacitive bypass, we analyzed the recorded videos of the coupling cavity to track the movement of

the front interface (same relative phase shift as κ_1) and the rear interface (same relative phase shift as κ_2). The optical flow between two subsequent frames of the video was computed using Matlab, which allowed us to extract relative velocity amplitudes in defined regions of the videos [154]. This was performed for both, the front and the rear interface, then the acquired data was transformed to spectral space and finally the phase information at the modulation frequency was extracted for each interface from the corresponding fast Fourier transform (FFT) bin.

5.7.2 Estimation of parameters of flow-path elements

To calculate the hydrodynamic resistance of individual flow path elements, we used the formulas listed as follows:

For elements with round cross-section (capillaries) [64]:

$$R_{round} = \frac{8 \cdot \mu \cdot l}{\pi \cdot r^4} \quad (5.1)$$

Here, $\mu = 1.002 \cdot 10^{-3}$ Pa · s is the dynamic viscosity of water at room temperature, r is the cross-sectional radius of the flow-path element and l is its length.

For elements with rectangular cross-section (channels) [155]:

$$R_{rect} = \frac{4 \cdot \mu \cdot l}{w \cdot h^3} \cdot \frac{1}{\frac{1}{3} - \frac{64 \cdot h}{\pi^5 \cdot w} \cdot \tanh \frac{\pi \cdot w}{2 \cdot h}} \quad (5.2)$$

w is the width and h the height of the flow-path element under consideration, with $w > h$.

To estimate the hydrodynamic resistance of flow-path elements in the gap between probe and sample, we assumed purely radial flow and one central injection emitting liquid at the flow rate Q [64]. Based on continuity and assuming no-slip boundary conditions at the probe and the sample, it can be stated that

$$Q = \int_0^h dz \int_0^{2\pi} r d\theta A(r) z(h-z) \quad (5.3)$$

Here, the z -axis is oriented perpendicularly to the two parallel plates, $z = 0$ is at the surface of the sample and $A(r)$ is the area of the bounding surface at radius r . Integration over the gap distance h yields:

$$\vec{u}(r, z) = \frac{3Q}{\pi h^3} z(h-z) \vec{e}_r \quad (5.4)$$

Inserting this expression into the creeping flow approximation of the Navier-Stokes equations gives

$$\frac{\partial p}{\partial r} = -\mu \frac{\partial^2 \vec{u}}{\partial z^2} \quad (5.5)$$

and integration results in an expression for the pressure p at a given radius r

$$p(r) = \frac{6\mu Q}{\pi h^3} \ln \left(\frac{r_1}{r_2} \right) \quad (5.6)$$

Therefore

$$R_{gap} = \frac{6\mu}{\pi h^3} \ln\left(\frac{r_1}{r_2}\right) \quad (5.7)$$

We assumed $r_1 = 100 \mu\text{m}$ and $r_2 = 300 \mu\text{m}$ for the HFC (R_8 and Z_6) and $r_1 = 100 \mu\text{m}$ and $r_2 = 600 \mu\text{m}$ for the elements linking to the edge of the apex (R_9 , R_{10} and Z_7 , Z_8).

To estimate the capacitance of the volume of air in the coupling cavity, we assume ideal gas laws and fully isothermal compression. The compressibility of the gas inside the cavity therefore is $k = -1/V \cdot \partial V/\partial t = 1 \cdot 10^{-5} \text{ Pa}^{-1}$. If the pressure applied through the liquid to the gas in the cavity changes, the volume of liquid inside the cavity changes:

$$Q = C \cdot \frac{d\Delta p}{dt} \quad (5.8)$$

Q denotes the flow of liquid and C the capacitance of the cavity. Insertion of k yields:

$$Q = -\frac{dV}{dt} = -V \cdot \left(-\frac{1}{V} \frac{\partial V}{\partial p}\right) \cdot \frac{d\Delta p}{dt} = -kV \cdot \frac{d\Delta p}{dt} \quad (5.9)$$

It thus follows that

$$C = -kV \quad (5.10)$$

The impedance Z_C of the capacitive element further depends on the modulation frequency f_m :

$$Z_C = \frac{1}{i \cdot 2\pi f_m \cdot C} \quad (5.11)$$

5.7.3 Nodal analysis - systems of linear equations

Conversion of the ideal voltage sources to current sources (connected in parallel with the first flow-path element) following the Norton theorem [153]

$$I_1 = \frac{V_1}{R_1} \quad (5.12)$$

Analysis of probes with resistive bypass

The system of linear equations for a probe with resistive bypass (g_i denotes the conductance $1/R_i$):

$$\begin{pmatrix} g_1 + g_4 + g_6 & -g_4 & 0 & -g_6 & 0 \\ -g_4 & g_2 + g_4 + g_5 & -g_5 & 0 & 0 \\ 0 & -g_5 & g_3 + g_5 + g_7 & 0 & -g_7 \\ -g_6 & 0 & 0 & g_6 + g_8 + g_9 & -g_8 \\ 0 & 0 & -g_7 & -g_8 & g_7 + g_8 + g_{10} \end{pmatrix} \cdot \begin{pmatrix} \varphi_1 \\ \varphi_2 \\ \varphi_3 \\ \varphi_4 \\ \varphi_5 \end{pmatrix} = \begin{pmatrix} I_1 \\ I_2 \\ -I_3 \\ 0 \\ 0 \end{pmatrix} \quad (5.13)$$

Analysis of probes with capacitive bypass

The system of linear equations for the ac analysis of a probe with capacitive bypass (y_i denotes the admittance $1/Z_i$):

$$\begin{pmatrix} y_1 + y_3 + y_4 & -y_3 & -y_4 & 0 \\ -y_3 & y_2 + y_3 + y_5 & 0 & -y_5 \\ -y_4 & 0 & y_4 + y_6 + y_7 & -y_6 \\ 0 & -y_5 & -y_6 & y_5 + y_6 + y_8 \end{pmatrix} \cdot \begin{pmatrix} \kappa_1 \\ \kappa_2 \\ \kappa_3 \\ \kappa_4 \end{pmatrix} = \begin{pmatrix} I_1 \\ 0 \\ 0 \\ 0 \end{pmatrix} \quad (5.14)$$

The resulting values for the nodes $\kappa_1 - \kappa_4$ are phasors expressing the amplitude and phase of the respective node at the modulation frequency.

The system of linear equations for the dc analysis of a probe with capacitive bypass:

$$\begin{pmatrix} y_1 + y_4 & 0 & -y_4 & 0 \\ 0 & y_2 + y_5 & 0 & -y_5 \\ -y_4 & 0 & y_4 + y_6 + y_7 & -y_6 \\ 0 & -y_5 & -y_6 & y_5 + y_6 + y_8 \end{pmatrix} \cdot \begin{pmatrix} \kappa_1 \\ \kappa_2 \\ \kappa_3 \\ \kappa_4 \end{pmatrix} = \begin{pmatrix} I_2 \\ -I_3 \\ 0 \\ 0 \end{pmatrix} \quad (5.15)$$

5.7.4 Optimization routines for definition of adequate input parameters

Determination of input parameters for a probe with resistive bypass

We iteratively solved the system of linear equations in Matlab within an interior-point constrained optimization routine (fmincon) to find a workable combination of settings for all three sources with respect to the following conditions:

The optimization target was defined to be the minimization of the ratio of aspirated flow to the sum of the flows through the injection and the compensations channel. This makes the optimization settle in a local minimum in vicinity to the defined starting points ($p_1 = p_2 = -p_3 = 100$ mbar).

We postulate that the pressure p_1 of the source connected to the injection channel to be positive, i.e. flow is injected into this channel.

The flux Q_7 across flow-path element 7 should be three times larger than the flux Q_6 across flow-path element 6. This corresponds to an aspiration-to-injection-ratio of three in a classical probe without bypass. By experience this ratio results in a well-shaped HFC for common gap distances.

Further, the potential φ_4 should be negative relative to the ambient, to make sure there is inward flow to the gap between probe and sample and no processing liquid leaks to the immersion buffer.

The potentials φ_1 and φ_2 should be equal to suppress flow of processing liquid through the bypass during normal operation at the desired working distance.

At a working distance of 20 μm , for example, for the design characterized in Figure 5.4d, suitable relative pressures would be $p_1 = 54$ mbar, $p_2 = 120$ mbar and $p_3 = -100$ mbar, resulting in total injection/aspiration flow rates of 1.5 $\mu\text{l}/\text{min}$ through the injection channel, 3.5 $\mu\text{l}/\text{min}$ through the compensation channel and 8 $\mu\text{l}/\text{min}$ through the aspiration channel during normal operation.

Determination of input parameters for a probe with capacitive bypass

The above model of a probe with capacitive bypass is solved within an optimization routine, to find a combination of settings for the sources with respect to following conditions:

The optimization target was defined to be the minimization of the ratio of aspirated flow to the dc offset injection flow. This makes the optimization settle in a local minimum in vicinity to the defined starting points ($\hat{p}_1 = -p_3 = 100$ mbar).

We postulate that the pressure $p_1(t)$ of the source connected to the injection channel to be greater or equal to zero at all times, i.e. flow is injected into this channel.

The flux Q_5 across flow-path element 5 should be three times larger than the time averaged flux \bar{Q}_4 across flow-path element 4 to again reach an effective aspiration-to-injection-ratio of three.

Further, the time averaged potential $\bar{\kappa}_3(t)$ should be negative relative to the ambient, to make sure there is an overall inward flow to the gap between probe and sample and no processing liquid leaks to the immersion buffer.

For the proposed exemplary design (see Figure 5.9c) for the admittance values of flow path elements of the specific design we analyzed) this analysis results in a constant offset pressure at the input of 40 mbar, which is superimposed by a sinusoidal modulation with an amplitude of 40 mbar, which results in a mean flow of 2.8 μl through the injection channel. At the aspiration a constant differential pressure of -99 mbar is applied, resulting in a mean flow of 9.8 $\mu\text{l}/\text{min}$.

5.7.5 Measurement of relative phase shifts

The measurement setup used for the assessment of the phase shift between the movement of the front and the rear interface in the coupling cavity is depicted in detail in Figure 5.7. As mentioned in the main paper, buffers were required to avoid counter-productive controlling actions of the pressure control system as it would detect unstable pressure levels at its outputs if there were no buffers.

The flow sensors in each flow path are not needed in principle, but allowed to counter check the calculations of the resistance of the respective flow path and to monitor the system during the experiment more carefully.

The actual relative pressure levels set with the pressure control system during the experiment presented in Figure 5.6b, were:

Buffer 1:	410 mbar
Buffer 2:	-210 mbar
Aspiration reservoir:	-100 mbar (measured flow rate: 9.1 $\mu\text{l}/\text{min}$)
Compensation reservoir:	ambient pressure

The negative relative pressure in buffer 2 allows the modulation amplitude to be increased. The relative pressures applied in the buffers greatly exceed the modulation amplitude of about 40 mbar suggested by the model. Nevertheless, as the model is in good agreement with the measured aspiration flow and a well-defined HFC was observed through the microscope (see video 1), we assume the actual pressure modulation in the injection reservoir to be in the range of the amplitude suggested by the model. We assume that only small fractions of the relative pressure levels present in the buffers get transferred to the reservoir, considering the dead volume and resistance of the tubing, the valve and the reservoir and the short switching times (250 ms, as the pressure is modulated at 4 Hz).

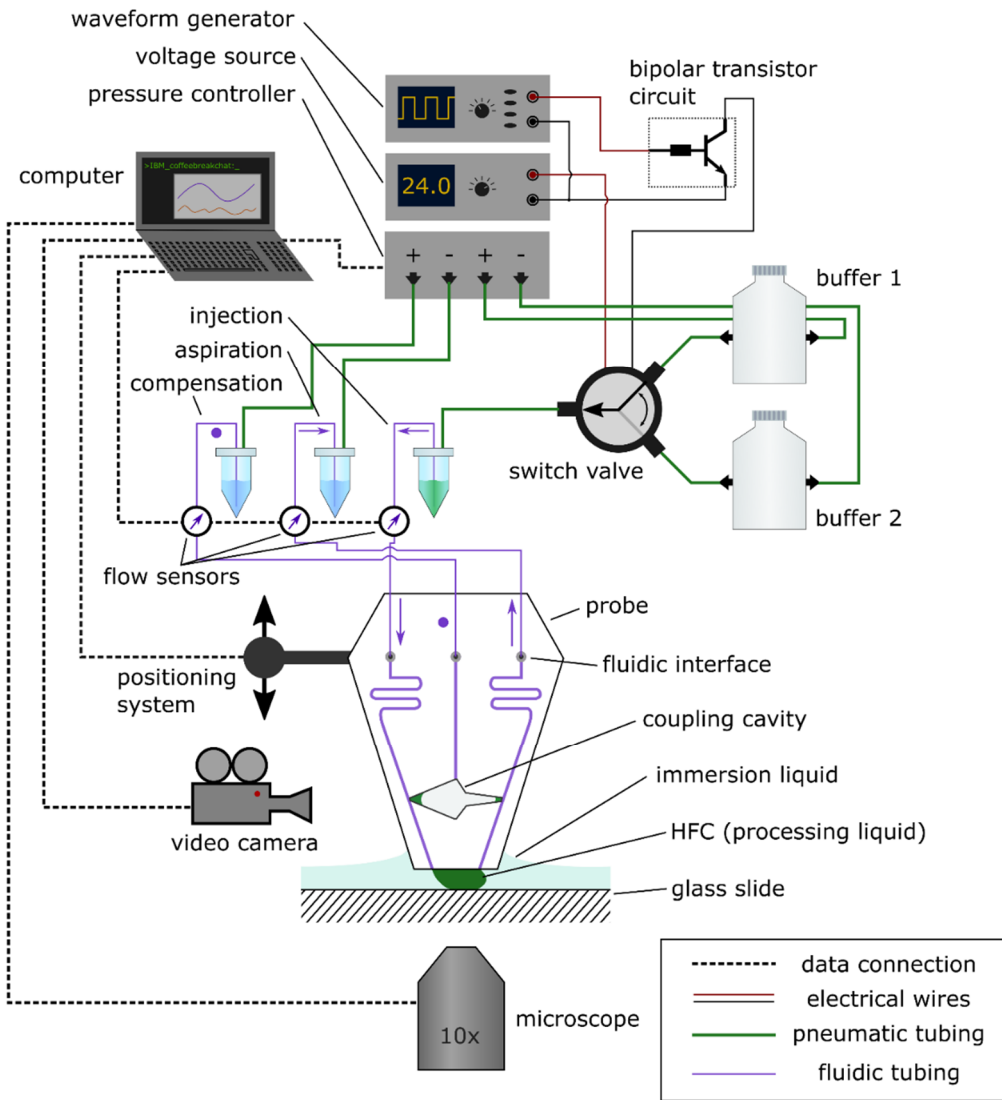


Figure 5.7: Setup for tracking the gap distance via monitoring the motion of liquid-gas interfaces. In addition to the setup required for a probe with a resistive bypass, this setup includes instrumentation required to modulate the pressure in the reservoir connected to the injection channel and a video camera for recording a side view of the probe.

5.7.6 Calculation of the relative movement amplitude of the rear interface

To estimate the movement amplitude of the rear interface we performed the following steps:

We first estimated the inner pressure of the coupling cavity in a situation with constant injection and aspiration (no modulation) at a gap distance of $20 \mu\text{m}$, by comparing the resulting positions of the front and rear interface with our observations from the experiment (see Figure 5.6c). Each interface adapts a position along the respective taper which results in a curvature of the interface corresponding to the pressure that drops across it. The opening width d_0 of the taper at the resting position of the interface is given by [124]:

$$d_0 = \frac{2 \cdot \cos(\theta - \psi)}{\frac{\Delta p}{\gamma} + \frac{h}{2 \cdot \cos(\theta)}} \quad (5.16)$$

Here, $\theta=45^\circ$ is the estimated contact angle between the liquid and the walls of the coupling cavity, ψ is the angle of inclination of the taper (15.5° for the front taper and 3.1° for the rear taper), $h=100\ \mu\text{m}$ is the etched depth of the coupling cavity and $\gamma = 75.75\ \text{mN/m}$ is the surface tension of the liquid.

As the reservoir connected to the compensation channel was mounted about 5cm above the surface of the immersion liquid surrounding the apex of the probe and no additional pressure was applied to this reservoir, we assume that a hydrostatic pressure of $p_c = 0.05\ \text{m} \cdot 0.1 \cdot 10^5\ \text{Pa/m} = 500\ \text{Pa}$ built up in the coupling cavity. With mean relative pressures of 128 Pa at κ_1 and of $-414\ \text{Pa}$ at κ_2 , the front interface, according to the model, stabilizes at a width $d_{0f} = 340\ \mu\text{m}$ and the rear interface at a width $d_{0r} = 120\ \mu\text{m}$. These interface positions are in good accordance with our experimental observations.

The resting position of the rear interface is re-calculated for each examined gap distance by taking into consideration the calculated relative pressure at κ_2 and an internal pressure of the cavity of $p_c = 500\ \text{Pa}$.

We assume the response of the interface to be linear for small variations of pressure. To find the deviation of the interface from its resting position due to the modulation of the pressure, we evaluate the maximum change of pressure drop across the coupling cavity due to the modulation $dp = \max(p_{\kappa_1}(t) - p_{\kappa_2}(t))$. Then, using the above equation, the total change in position dx is:

$$dx = \frac{d_0}{\Delta p} \cdot dp \cdot \frac{1}{\tan \psi} \quad (5.17)$$

Two effects impact dx across the space of frequencies and gap distances: for small gap distances $\frac{d_0}{\Delta p}$ becomes very small (this derivative has a quadratic dependence of the pressure in the denominator) and thus the movement amplitudes get smaller, too. For higher frequencies, the modulation of the pressure is more efficiently transduced to the aspiration channel and the pressure difference across the cavity dp becomes smaller (see Figure 5.8b), which also in a reduction of dx .

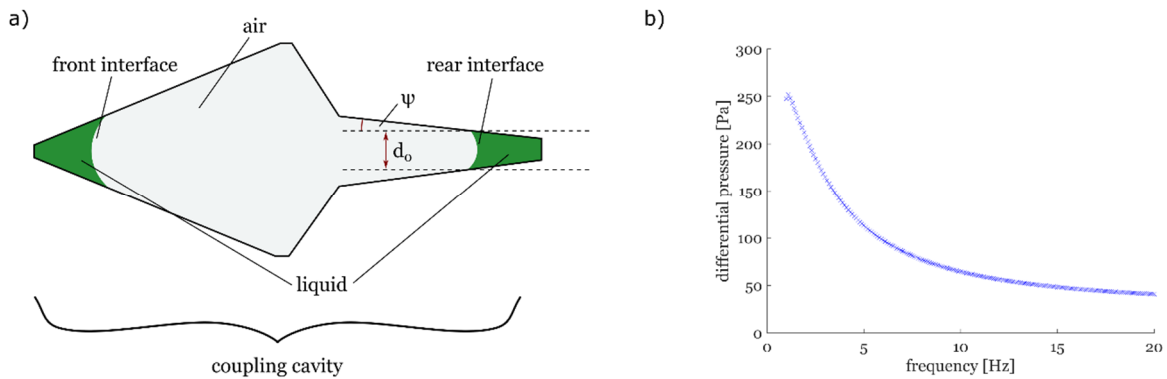


Figure 5.8: Motion of the interfaces in the coupling cavity due to the pressure modulation. a) The opening width of the taper is lower for the rear interface as the pressure drop across this interface is higher and the resulting curvature of the interface is smaller. b) The differential pressure drop across the interface decreases with increasing modulation frequency, as the transfer of the modulation is more efficient at higher frequencies.

5.7.7 Modification of the model to fit the experimental data

When comparing the recorded experimental data with the analytical model presented in the paper, we found that a capacitive element has to be introduced in parallel to Z_1 or Z_2 , in order to account for parasitic

capacitances across the fluidic network and, more importantly, a resistive element connected in parallel to the capacitor of the coupling cavity has to be taken into account. This resistive element was present as well in the described experiments: as the liquid has a contact angle to the walls of the coupling cavity lower than 90° , a liquid film covers the walls of the coupling cavity and enables a direct flow of liquid between κ_1 and κ_2 . As demonstrated in Figure 5.9b, this resistive element leads to a significant change in the behavior of the fluidic network: the blue curve represents the behavior of the model fitted to the experimental data (with an additional capacitive element added to Z_2 and a resistive element added to Z_3) and the brown curve displays the behavior of the same model, but without the resistive element added to Z_3 . The fitted model (blue curve) originally converges towards 0 for large gap distances and has to be shifted by an offset of 0.23 rad to fit the experimental data. The model without a bypass flow through the cavity (brown curve) approaches a constant value large gap distances. We therefore believe that the most accurate description of our experimental data would be a hybrid model, as the thickness of the liquid film at the walls of the cavity, and thus also the resistance of the bypass through the cavity, changes with the relative pressure that drops across the coupling cavity. We did not further investigate this, as the purpose of this study was to demonstrate the basic feasibility of assessing the probe-sample distance by observing relative phase shifts in the movement of the two interfaces. We expect that the total relative phase shift and thus the sensitivity and measurement range of the presented approach can be significantly improved by making regions of the coupling cavity hydrophobic to prevent a bypass flow of liquid.

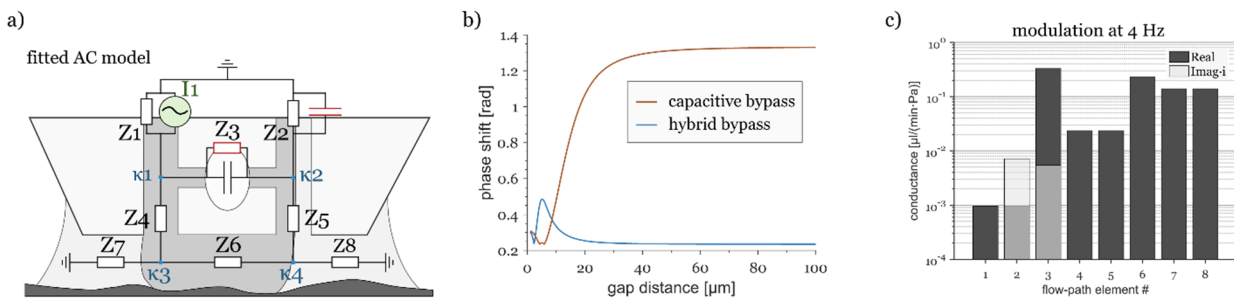


Figure 5.9: Adjusted model for ac configuration. a) In order to fit the experimental data additional flow-path elements (red) were included in the model. b) Comparison of a model with parallel resistive element in the bypass (blue) and a model without parallel resistive element in the bypass (brown). The capacitor in parallel to Z_2 was kept for both models. c) Admittances of the flow-path elements with capacitive bypass (volume of coupling cavity is 0.36 mm^3). The admittance of elements with capacitive characteristics has an imaginary part (displayed in light grey color).

Chapter 6 Reconfigurable microfluidics: real-time shaping of virtual channels through hydrodynamic forces

The content of this chapter is based on the pre-print version of below listed research article, which is currently being reviewed for publication in *Small*, and is reproduced here with minor modifications.

D. P. Taylor and G. V. Kaigala, "Reconfigurable Microfluidics: Real-time Shaping of Virtual Channels through Hydrodynamic Forces," *Small*, **2019**, under review (smll.201902854)

6.1 Abstract

To break the current paradigm in microfluidics that directly links device design to functionality, we introduce microfluidic “virtual channels” that can be dynamically shaped in real-time. A virtual channel refers to a flow path within a microfluidic flow cell, guiding an injected reagent along a user-defined trajectory solely by hydrodynamic forces. Virtual channels reproduce key microfluidic functionality: directed transport of minute volumes of liquid, splitting, merging and mixing of flows. Virtual channels can be formed directly on standard biological substrates, which we demonstrate by sequential immunodetection at arrays of individual reaction sites on a glass slide and by alternating local and global processing of surface-adherent cell-block sections. This approach is simple, versatile and generic enough to form the basis of a new class of microfluidic techniques.

6.2 Introduction

The precise control of liquid flow at the microscale is central to microfluidics and its numerous applications [4], [156]. Current microfluidic devices are designed and fabricated to perform specific tasks and allow only a few parameters to be altered during operation, such as e.g. flow rate and temperature. The most critical parameter of a microfluidic technique however is the geometry of the fluidic device itself. We believe that breaking the current paradigm of a direct linkage between the design of a microfluidic device and its functionality will spur new microfluidic methodologies. The value of versatile technological platforms is well illustrated in the field of electronics by the success of field programmable gate arrays (FPGA). To provide a similar level of flexibility, a reconfigurable microfluidic platform should be able to dynamically implement key microfluidic functions such as: (a) the directed transport of minute volumes of liquids, (b) splitting, (c) merging, and, (d) mixing of microfluidic flows.

While arrays of valves allow for switching between predefined flow paths, the corresponding devices are complex multi-valve microsystems and offer only limited dynamics [157]–[159]. Current implementations of reconfigurable microfluidic devices mostly rely on the directed motion of the contact line between a surface-born aqueous phase and an immiscible host phase to either propel single droplets across a surface [160] (digital microfluidics), or to establish steady, channel like flow-paths [39], [161] (virtual electrowetting

channels). Interfaces between immiscible liquids can be displaced by means of electrowetting [39], [160], [161], thermowetting [162], or surface acoustic waves [163]. Subject to the physics of wetting and de-wetting, these methods either exhibit slow dynamics in the reconfiguration of established channels or do not allow a continuous flow of liquid. In either case, specific surface properties are required to enable a controlled displacement of liquids. Besides their well-known applications involving electrowetting, arrays of electrodes can also be used to control flow patterns in fully aqueous environments by locally tuning non-uniform electro-osmotic flow (EOF) [60], [61]. Nonetheless, practical use of EOF is limited, as it only allows the generation of relatively low flow rates and is impacted by the composition of the used liquid. Two classes of devices have emerged that enable a dynamic implementation of microfluidic flow patterns in compatibility with a wide range of aqueous buffer conditions and flow rates: 1. microfluidic perfusion systems [12], [13], [164], [165] with a flow cell, in which flow patterns can be created and altered through injection and aspiration of liquid from openings in the side walls of the flow cell, and 2. liquid scanning probes [25], [26], [95], [140], [166], [167], which allow the creation of deterministic flow patterns atop immersed flat surfaces by continuous injection and re-aspiration of liquid from apertures at their apex. Nevertheless, both these approaches fall short of dynamically reproducing key functional aspects of classical microfluidic channels: As microfluidic perfusion systems only allow for in-plane injection and withdrawal of liquid from lateral openings, they e.g. do not allow for splitting or merging of microfluidic streams. Concepts of liquid scanning probes demonstrated so far, on the other hand do not provide enough degrees of freedom, i.e. enough independently tunable injection and aspiration flows, to enable the formation of by-design channel patterns.

Here we present a concept to guide the flow of a reagent inside a microfluidic flow cell along a reconfigurable trajectory – a “virtual channel” – which enables a dynamic implementation of key microfluidic functions. To form a virtual channel, the flow of a reagent is hydrodynamically confined to a defined flow path via the controlled injection of buffer liquid from an array of apertures featured in the bottom of the flow cell. Virtual channels can interact with widely used substrate formats, such as microscope slides and Petri dishes, in a straightforward and reversible way. We further introduce new functionalities enabled by programmed sequences of channel configurations and illustrate potential applications, i.e. the implementation of a multistep surface-immunoassay, as well the localized sequential processing of a cell block slice. We believe that the device and method we demonstrate here could form the basis of novel microfluidic methodologies to be developed in the context of research, as well as of diagnostic and industrial applications.

6.3 Results and discussion

6.3.1 Formation of virtual channels

We create virtual channels in a microfluidic flow cell (Figure 6.1a) formed by a rectangular recess ($60\text{ mm} \times 20\text{ mm} \times 0.1\text{ mm}$) which is closed from top with a glass slide (see Figure 6.6 for detailed schematics). The flow cell is uniformly filled with an aqueous immersion buffer and flow boundary conditions are applied via out-of-plane flow through apertures in the bottom of the recessed area. Through independent control of the flow rate at each aperture (see Figure 6.7 for information on flow control hardware), the velocity potential landscape within the flow cell is tuned locally to form and manipulate virtual channels. As flow within the flow cell is laminar and the directionality of flow is constant on any plane between the top and the bottom confining surface, the conformation of virtual channels can be well-described in 2D. We therefore use potential flow theory to analyze the motion of liquid within the flow cell. The resulting flow velocity at any point in the analyzed plane is the gradient of a complex potential Ω , which is a linear superposition of the complex potentials generated by each aperture (see section 6.4.2). In the standard configuration, i.e. to form elongated

virtual channels towards the open boundary of the flow cell (Figure 6.1a), aqueous immersion liquid is injected at about $250 \mu\text{l min}^{-1}$ from aperture A. Since the flow rate imposed on aperture A usually is the highest occurring flow rate, we also refer to it as the “main injection”. By injection and aspiration of immersion buffer from the apertures in the 4×4 aperture array (first row: apertures 1-4, second row: 5-8, and so on), the virtual channel guiding the flow of a reagent injected from aperture B can be dynamically altered. Reagents are injected at flow rates approximately 500-fold lower than those at aperture A.

To exploit the dynamic aspect involved in the creation of virtual channels, a user must be able to create and modify virtual channels based on visual observations or changing experimental requirements. To implement a user-defined channel configuration (step 1 in Figure 6.1b), the flow rates to be set at the individual apertures are determined via a one-step fitting scheme based on potential flow theory (see supplementary text for details). Step 2 in Figure 6.1b displays the anticipated flow pattern illustrated by contour lines of the stream function ψ , which are parallel to the streamlines of the flow.

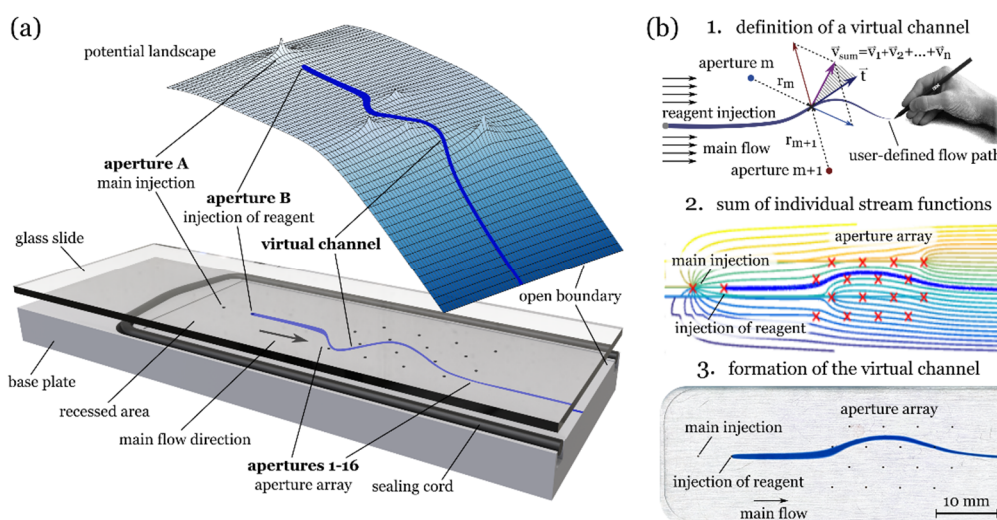


Figure 6.1: Formation of virtual channels inside a microfluidic flow cell. a) Virtual channels are generated in a flow cell with one open lateral boundary. The bottom confining surface features apertures through which liquid can be injected or aspirated. Immersion buffer is injected from apertures A and 1-16 to create and dynamically adjust flow trajectories – virtual channels – towards the open boundary of the flow cell. Aperture B serves as the inlet for injection of a reagent. b) 1. A desired channel configuration is user-defined through one or several splines. The flow rates required to match these splines are determined numerically by minimizing an analytical expression for the area spanned by the tangent vector \vec{t} to the spline and the local flow velocity \vec{v} at discretized points (see supplementary text for details). 2. The resulting flow pattern is represented by a contour plot of the stream function. 3. The desired channel configuration is formed by application of the determined flow rates. In the displayed experiment, water with blue food dye is injected into the virtual channel.

The blue streamlines highlight the anticipated trajectory of an injected reagent assuming the impact of diffusion is negligible. Calculating an average Péclet number $Pe = \bar{v} \cdot W/D$ provides good insight into the relevance of diffusion for the confinement of a reagent in a virtual channel. Here, $\bar{v} = 5 \text{ mm s}^{-1}$ is a representative mean flow velocity in the flow cell, $W = 0.5 \text{ mm}$ is the width of a virtual channel and $D = 2 \cdot 10^{-3} \text{ mm}^2 \text{ s}^{-1}$ is the diffusivity of a small molecular reagent of interest (e.g. carbon monoxide) in water. The resulting Pe here is on the order of $1.25 \cdot 10^3$, indicating that advection dominates in the transport of molecules and diffusion can be neglected for virtual channels at described length-scales and flow velocities. The determined flow rates can be output to a multichannel flow control unit, in our case an array of syringe pumps, to physically establish the desired virtual channel (step 3 in Figure 6.1b). The dynamics of the

establishment of a virtual channel are influenced by: (a) The time required for all set flow rates to stabilize, which we observed to take up to 2 s. We attribute this lag to the finite stiffness and mechanical reverse play in our self-made flow control unit and to microbubbles trapped in microfluidic fittings and connecting capillaries. (b) The time required to flush volumes of reagent left behind by a disbanded virtual channel. A full transition from the confinement of a reagent in one virtual channel to its full confinement in a subsequently formed channel depends on the overall flow velocity in the flow cell and is typically on the order of 20 s.

6.3.2 Implementing key microfluidic functionalities using virtual channels

Directed transport of a reagent to a certain position of the open boundary of the flow cell, which could be linked to e.g. reservoirs to collect finite sample volumes, is demonstrated in Figure 6.2a. This function is analogous to a microfluidic multiport selection valve that connects one inlet port to several outlet ports. A virtual channel can be rapidly linked to another position at the open boundary without cross-contamination and while allowing full optical access for e.g. process control. This concept could be applied to a continuous flow but also to trains of droplets or suspended objects. The shape of a virtual channel can also be adjusted locally, without changing its overall flow direction. This enables targeted interaction with a wide range of flat substrates, such as functionalized surfaces, or slides supporting surface-adherent cells or tissue sections, which can be used as the top surface of the flow cell. Such surfaces could be treated with reagents confined in virtual channels at well-defined interaction sites, such as the sine-shaped pattern displayed in Figure 6.2b. Analogous to classical microchannels, virtual channels can be split to fractionate the flow of a reagent, as shown in Figure 6.2c. The distribution of flow at the splitting point of a virtual channel can be adjusted to match a desired ratio of fractionation.

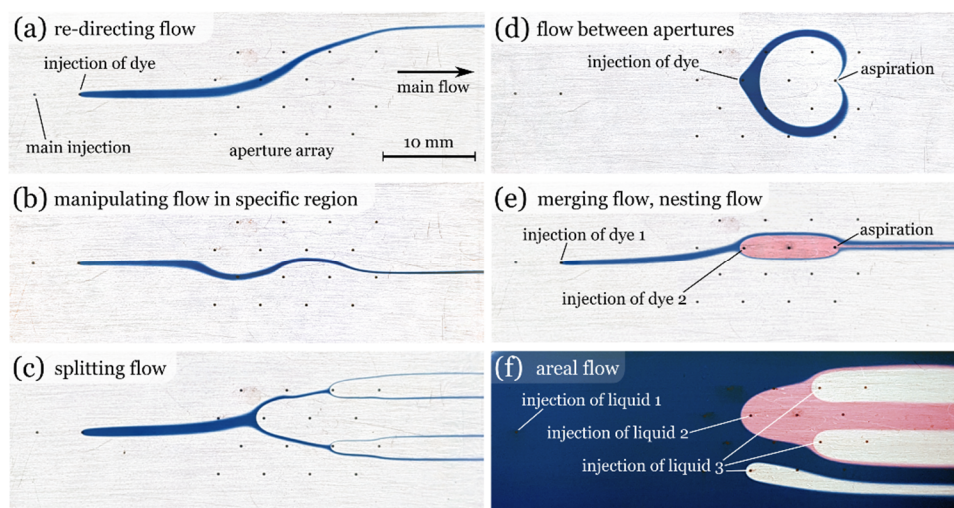


Figure 6.2: Implementing basic microfluidic functionality with virtual channels. a) A virtual channel can be directed to a certain position at the open boundary. b) Multiple inflection points can be generated to let the virtual channel pass through specific regions of the flow cell. c) Stagnation points can be generated. A virtual channel that leads to stagnation point is split. d) Circular virtual channels formed between apertures within the array. e) Nested configuration of virtual channels enabling the co-flow of two different liquids. f) Generation of multiply nested broad virtual channels.

By aspiration of liquid to an aperture, other channel shapes, e.g. circular virtual channels, can be created, as shown in Figure 6.2d. In the displayed configuration, the flow of reagent is injected and aspirated at apertures within the aperture array. Similarly, finite volumes of two different reagents could be aspirated into the microfluidic capillary linked to an aperture and be re-injected after enough time has passed for diffusive mixing

of the two reagents. The channel configuration displayed in Figure 6.2e demonstrates co-flows of different liquids to e.g. control the morphology of a reactive interface between two adjacent virtual channels. Figure 6.2f illustrates the formation of nested virtual channels which could be used to perform multiplexed, area specific treatment of surfaces.

6.3.3 Dynamic flow patterns

Dynamic control can be realized by timed execution of a sequence of flow patterns known *a priori* or by the real-time-adjustment of flow patterns based on feedback obtained from the experiment. The dynamic control of virtual channels enables a level of versatility, which is not attainable using fixed channels. By performing a cyclic sweeping-motion with a virtual channel (see Figure 6.3a), the effective exposure time of specific regions of the top surface of the flow cell to a specific reagent can be defined independently. This enables the generation of customized surface gradients, which are difficult to generate with methods that rely on diffusive transport for the formation of gradients [164].

Dynamic flow patterns can further be employed to control the position of a single droplet of an immiscible phase within a 2D flow cell. Figure 6.3b shows the directed motion of a water droplet in a flow cell filled with FC-40 oil controlled solely by hydrodynamic drag. Since the flow remains laminar at flow rates up to five orders of magnitude higher than described here, significant shear stress could be applied to droplets and we anticipate droplets could also be split and merged using the described platform. The demonstrated array of apertures would also be a well-suited vehicle to realize the simultaneous positioning of five and more particles, which has been theoretically described [74] and experimentally demonstrated for up to two particles, so far [72].

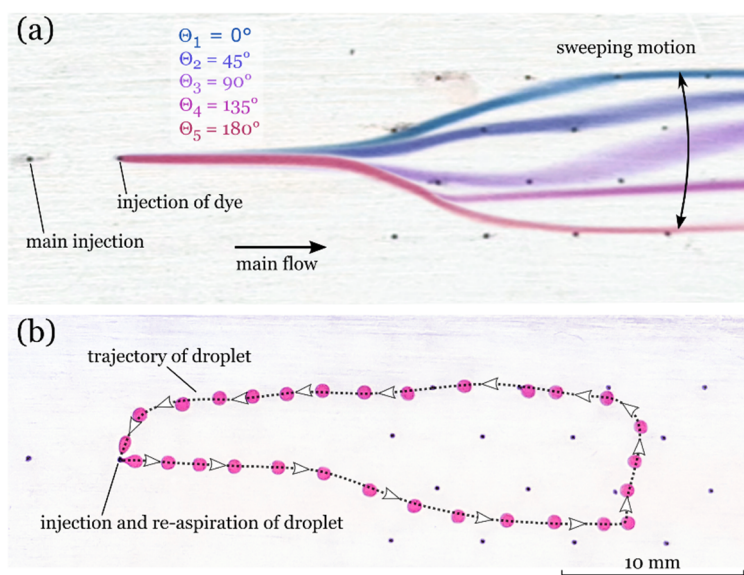


Figure 6.3: Temporal control of flow patterns. a) Sweeping motion of a virtual channel to e.g. locally control the interaction time of a reagent with the top confining surface. The false-coloring of the liquid in the virtual channel highlights that each displayed configuration corresponds to a different phase Θ of a cyclic sequence. b) In-plane positioning of a single water droplet in an oil-filled flow cell. This illustration shows an overlay of photographs taken at intervals of 3 s.

6.3.4 Surface assays through virtual channels

Surface assays are widely used across research, diagnostics and industry and play an important role in proteomics and cell biology, the diagnostic analysis of tissue sections and drug development. A prominent form of surface assays are surface-based immunoassays. Established microfluidic implementations of surface immunoassays, mostly rely on mechanical contact between an open-top channel system and a target surface [14], [15]. We here in contrast demonstrate a surface immunoassay using sequentially generated, crossing configurations of virtual channels (Figure 6.4a). This approach e.g. enables the screening of assay conditions, or even the adaptive implementation of surface assays directly at specific locations of heterogeneous surface-adherent samples without relying on mechanical contact to constrain the flow of reagents. We performed a two-step immunoassay to detect a surface-bound model antigen, as illustrated in the inset in Figure 6.4a. We injected a primary antibody into a virtual channel and let this channel persist in three different conformations for three different incubation times. In a second step, we injected a secondary antibody into another virtual channel, which we again kept in three different conformations for three different incubation times. The secondary antibody binds at the nine reaction sites, where the different conformations of the two sequentially generated virtual channels cross. Figure 6.4b shows the resulting fluorescent signature of the reaction sites. Figure 6.4c displays the mean brightness value of an area of $100 \mu\text{m}^2$ at the center of each reaction site. As expected, the different incubation times with the primary and the secondary antibody result in characteristic signal levels. While the dependence on the secondary antibody incubation time remains linear for reaction sites a-f, saturation can be observed at sites g, h and i.

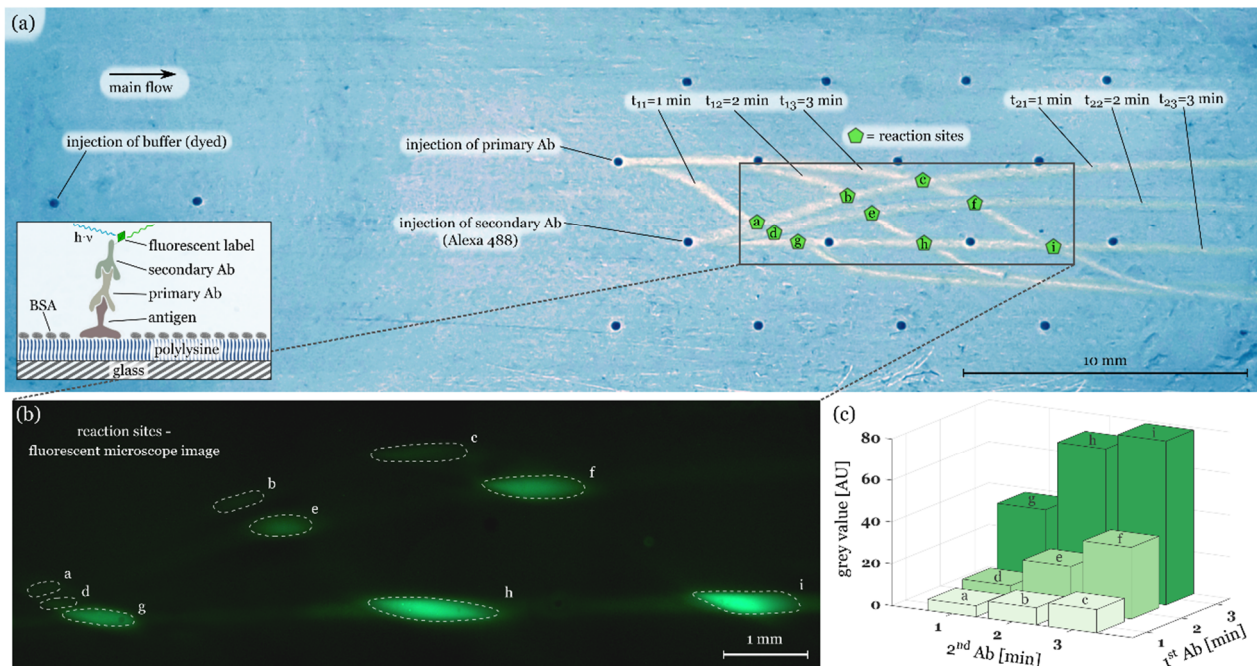


Figure 6.4: Localized immuno-patterning. a) Nine individual reaction sites with specific incubation conditions are created on the top glass slide by flowing primary Ab solution and secondary Ab solution through crossing configurations of sequentially formed virtual channels. b) Fluorescent microscope image of the reaction sites. c) Mean signal intensities at each reaction site.

Other relevant variants of surface assays focus on interactions with surface adherent cells, or cell block slices and tissue sections. While some steps in the processing of such samples must be performed on the entire sample surface, it is often desirable to perform selected steps on only a specific region to e.g. allow for

multiplexing or more detailed analysis of specific regions [13], [26]. Here we demonstrate an exemplary workflow for processing a 5 μm thick section of cultured human colon carcinoma cells attached to a microscope glass slide (see Figure 6.5).

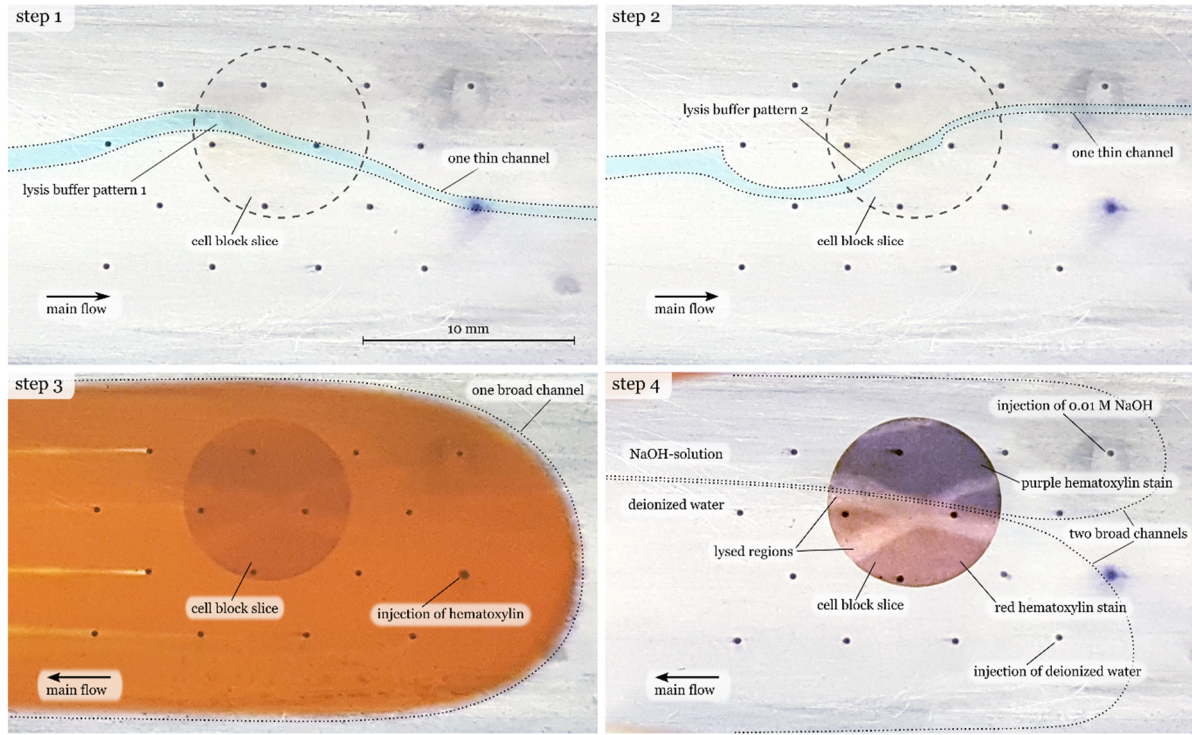


Figure 6.5: Targeted sequential sample processing. Step 1&2: Lysis buffer is locally flown over a cell block slice adhering to the top glass slide. Step 3: Global staining with hematoxylin. Step 4: Local exposure to alkalic or acidic buffer, to alter the color of the hematoxylin stain.

Through confinement of different reagents in sequential configurations of virtual channels, the cell block section was locally lysed (Figure 6.5 steps 1&2), globally stained (step 3) and then selectively exposed to different pH-conditions (step 4).

These examples illustrate how crossing configurations of virtual channels allow to perform sequential assays at any desired location of a biologically relevant surface to e.g. characterize antibody-antigen binding dynamics, or how different morphologies of virtual channels allow to alternate between local and global interaction to e.g. lyse and sample specific regions of a cell block or tissue section.

Following work on reactions between co-flowing liquids in classical channels [70], adjacent virtual channels could further be used for controlling the position of reactive interfaces between liquids to e.g. form hydrogel-walls at specific locations within a flow cell, as shown in Figure 6.8. The in-situ formation of by-design hydrogel structures e.g. offers interesting perspectives for the long-term treatment of cell colonies with specific reagents.

6.3.5 Conclusion

We have presented a device and method to dynamically create and reconfigure liquid-walled virtual channels within a flow cell (Figure 6.1a). Virtual channels have several advantages: they can be reconfigured on-the-fly to match a user-defined configuration by means of simple analytical tools (Figure 6.1b) and can reproduce

key microfluidic functions (Figure 6.2). Virtual channels therefore allow us to extend established microfluidic protocols by e.g. localized sequential reactions (Figure 6.4), or by switching between global and local interaction with a surface adherent sample (Figure 6.5). The ability to program sequences of flow patterns further enables the creation of surface gradients by sweeping motions of virtual channels, or the 2D-positioning of droplets, bubbles or suspended objects solely by hydrodynamic drag (Figure 6.3). Virtual channels can be created atop any flat substrate commonly used in the life sciences, such as Petri dishes, microscope glass slides, plastic slides, or PDMS slabs and be used to interface with a wide range of surface adherent samples (Figure 6.4 and Figure 6.5). The proposed approach can be geometrically scaled down by about two orders of magnitude (limited by practical considerations), given that the depth h of the flow cell remains much smaller than the spacing between apertures in the array to e.g. enable the handling of single suspended cells.

As with any technology, virtual channels have limitations to be considered depending on their application: First, mass transport boundary conditions in virtual channels differ significantly from those in classical channels. While this is not a drawback per se, it certainly must be taken into consideration in specific cases. Second, while classical microfluidic channels can be designed to have any shape commensurate with the chosen method of fabrication, virtual channels cannot be tuned into any desired shape: e.g. creating meandering flows with 180° turns is not possible. Applications requiring such motion of liquid could be potentially addressed by dynamic position control of finite volumes of reagents. Third, when liquids with significantly different viscosities are used, or when the viscosity of a liquid changes locally (e.g. due to the lysis of cells), the controlled formation of virtual channels is challenging, as the above presented models do not reflect the impact of heterogeneous viscosity. This limitation can be mitigated by increasing the viscosity of all applied liquids (by e.g. adding glycerol) to match the maximum expected viscosity. Fourth, the presented method requires a multi-channel flow control unit. As illustrated in Figure 6.7, such a system can be built from inexpensive standard components or be set up based on commercial multichannel flow control units.

We envision that the range of functionality of virtual channels could be further extended by implementing microfluidic features on one of the confining surfaces of the flow cell, such as herringbone structures for more efficient mixing of adjacent streams [168], constrictions for the capturing of dispersed droplets or cells [169], or pillar arrays for size-based sorting of particles [170] or for the creation of specific cross-sectional flow patterns [76]. As the flow cell is fully accessible from one side, the presented concept could further be combined with external instrumentation, such as optical microscopes, optical tweezers, heating units, electrodes, or magnets.

Even though the height of conventional samples, such as tissue sections (thickness in the range of $5\mu\text{m}$, do not significantly impact the formation of virtual channels in a flow cell with a height of $100\mu\text{m}$, effects could be observed for much more shallow flow cells. Using an inverse approach, deviations of flow patterns from their original conformation could be used to characterize surface topographies. Further, we think it would be highly interesting to employ above presented platform for the investigation of instabilities, i.e. droplet formation of a second phase. Finally, we are convinced that it would be of high merit to combine above presented platform and methods with machine learning techniques to implement self-teaching control systems for the confinement of non-Newtonian liquids, liquids with different viscosities.

To summarize, in this paper we have presented a concept for the dynamic formation of virtual microfluidic channels, which are able to implement directed transport of minute volumes of liquid, as well as splitting, merging and mixing of microfluidic flows in user-defined channel configurations. Through their dynamic nature, virtual channels enable more interactive and adaptive experimentation, which could trigger novel

microfluidic methodologies. The presented approach is conceptually simple and allows interfacing with a wide range of standard sample and substrate formats, as well as with other instrumentation. We are convinced that virtual channels have the potential to significantly foster the use of microfluidics in research and in diagnostics across a wide range of applications.

6.4 Materials and Methods

6.4.1 Experimental section

Fabrication of the Microfluidic Device. The base plate featuring the apertures and the rectangular recess, as well as the cover plate used for fixation of a microscope glass slide were made from a standard aluminum alloy using conventional CNC fabrication techniques. The holder used for mounting the base plate, the microscope glass slide and the cover plate together was made using a fused deposition modelling 3D printer (F370, Stratasys Inc., USA). The apertures were machined with a diameter of 0.3 mm in the top side of the base plate and 1.4 mm on the backside of the base plate. We used ETFE capillaries with an inner diameter of 0.25 mm and an outer diameter of ~ 1.59 mm (#1529, Upchurch Scientific Inc., USA) to link each aperture with a syringe pump of the syringe pump array setup (see Figure S2). Glass syringes (SyriQ, Schott AG, Germany) were used in the syringe pumps, as plastic syringes, due to their deformability, introduced significant lag times between the actuation of a syringe pump and the stabilization of the effected flow rate. To mount and seal the capillaries with the base plate, we first mechanically stretched one end of a capillary to make it thin enough to fit in the corresponding hole in the backside of the base plate, which has a slightly smaller diameter than the unstretched capillary. Then we heated the base plate using a hot air gun while holding the capillary in, whereupon the capillary re-expands and gets locked in place. After repeating this for all capillaries, we cast epoxy glue (Araldite Rapid, Huntsman Corp., USA) on the backside of the base plate around all capillaries to ensure proper sealing a good mechanical stability and linked each capillary to a syringe pump.

Visualization of virtual channels. In all experiments optical contrast between virtual channels and surrounding regions was provided by food dye (Trawosa AG, Switzerland) added to either the liquid injected in a virtual channel, or to the surrounding buffer liquid. A Galaxy S7 cellphone (Samsung Electronics, South Korea) mounted on a camera tripod was used for recording of images and videos of the microfluidic flow cell.

Positioning of immiscible droplet. For the 2D positioning of an aqueous droplet, the aluminum surfaces of the base plate, as well as the inward-facing surface of the microscope glass slide were treated with trichloro(1H,1H,2H,2H-perfluorooctyl)silane (#448931, Sigma-Aldrich, USA) and all syringes, capillaries and the flow cell were filled with FC-40 oil (#F9755, Sigma-Aldrich, USA). Single aqueous droplets were generated by linking an additional, water-filled syringe to the capillary linked to the injection aperture using a T-junction (#P-632, IDEX Corp., USA).

Surface immunoassay. Polylysine adhesion microscope slides (Thermo Fisher Scientific Inc., USA) were incubated on-bench with $50 \mu\text{g ml}^{-1}$ IgG from rabbit serum (#I8140, Sigma-Aldrich, USA) in PBS (Dulbecco's phosphate buffered saline, Biowest SAS, France) for 1 h, then rinsed three times with PBS and then blocked by incubation with 1% BSA (#A2958, Sigma-Aldrich, USA) in PBS. After blocking, the slide was washed another three times with PBS and then mounted on the base plate, treated side facing downwards, to close the microfluidic flow cell. Before mounting the slide, all capillaries and the rectangular recess in the base plate were pre-filled with PBS. For the creation of channels, PBS was injected at required flow rates from the corresponding apertures. A small amount of food dye was added to all PBS solutions not containing antibodies, as

degradation of antibodies was observed when the food dye was added to the antibody solution. Then, anti-rabbit IgG produced in goat (#ab6702, Abcam PLC, UK) at a concentration of $25 \mu\text{g ml}^{-1}$ in PBS was flown through a virtual channel in three different channel configurations for 1 min, 2 min and 3 min respectively. Subsequently, anti-goat IgG produced in donkey (#ab150129, Abcam PLC, UK) with a fluorescent label (Alexa 488) at a concentration of $25 \mu\text{g ml}^{-1}$ in PBS was injected into another virtual channel in three different configurations for 1 min, 2 min and 3 min, respectively. After these incubation steps, the flow cell was flushed by the continued injection of PBS from the main injection aperture. The flow rate for the injection of reagents was $1 \mu\text{L min}^{-1}$ and the main injection flow rate was $150 \mu\text{L min}^{-1}$ for all processing steps performed in the microfluidic flow cell. After removal from the microfluidic setup, the glass slide was rinsed with DI water and then dried. Imaging of the resulting fluorescent stain remaining at the reaction sites was performed with an inverted microscope (TI-E, Nikon Corp., Japan), using a corresponding FITC-filter and a 4x objective for recording images with a larger field of view (Figure 6.4b) and a 10x objective for measuring the mean fluorescent intensity at each reaction site (Figure 6.4c).

Processing of cell block sections. Before processing, the glass slide-supported formalin-fixed, paraffin-embedded (FFPE) cell block sections (ASO-3036, Applied Stemcell Inc., USA) had to be de-waxed and rehydrated by sequential incubation for 3 min in each of the following solutions: 100% Xylene, 50% Xylene 50% Ethanol, 100% Ethanol, 50% Ethanol, pure DI water. Then the recess of the base plate and the capillaries were pre-filled with PBS (Dulbecco's phosphate buffered saline, Biowest SAS, France) and the glass slide was mounted to the base plate with the cell block slice facing downwards. A virtual channel crossing the cell block slice from top left to bottom right was created and a lysis solution (PBS with 10% proteinase K and 0.5 % SDS) was flown through this channel for 5 min. Then, the configuration of this channel was changed, so that it would cross the cell block slice from bottom left to top right and the lysis solutions was flown through the channel again for 5 min. As in this protocol, several reagents were to be applied in a sequence, we also injected reagents from apertures in the aperture array, which were not used for the shaping of virtual channels in the previously described steps. To reach the cell block slice with liquid injected from apertures lying closer to the open boundary of the flow cell than the cell block slice itself, we inverted the flow at the main injection aperture which was then used to aspirate liquid. With the overall flow direction being inverted, we created one broad virtual channel to treat the entire cell block slice with Mayer's hematoxylin solution (#MHS1, Sigma-Aldrich, USA) for 7 min. In a final step, we created two tangential virtual channels, each covering about one half of the cell block slice and flowed a 1 mM NaOH solution (pH 11) through one channel and DI water (pH 6) through the other one. This turned the hematoxylin stain purple in the section of the cell block covered by the alkaline liquid and red in the section covered by the acidic liquid.

Polymerization of hydrogel walls. To polymerize alginate walls at the interface between virtual channels, we created a virtual channel containing 10% CaCl_2 nested inside another virtual channel containing a 0.25% solution of sodium alginate (#A2033, Sigma-Aldrich, USA). We let the alginate polymerize at the interface between these two virtual channels for 10 s and then flushed the unpolymerized alginate solution and the CaCl_2 out with water.

6.4.2 Analytical description of 2D flow patterns

At Reynolds numbers on the order of $5 \cdot 10^{-2}$, flow inside the flow cell is purely laminar and a streamline pattern formed on e.g. the middle plane between the bottom and the top confining surface is also formed on any other xy -plane. It is therefore enough to consider the 2D case of any xy -plane via complex potential flow theory [64], [94]. The position of the m^{th} source on a corresponding complex plane is therefore given

by a complex number $c_m = x_m + i \cdot y_m$. The complex potential Ω_m created by this source at any position $c = x + i \cdot y$ is

$$\Omega_m(c) = \phi + i\psi = \frac{Q_m}{2\pi} \cdot \ln(c - c_m) \quad (6.1)$$

The real part of the complex potential is the velocity potential ϕ , whereas the complex part is the stream function ψ . The complex potential is created by a set of n sources and can be directly written as linear superposition of the single contributions $\Omega = \Omega_1 + \dots + \Omega_n$. The complex flow velocity vector $\vec{v}(c)$ at a given position c can be conveniently derived from the complex potential $\Omega(c)$ by differentiation:

$$\vec{v}(c) = u(c) + i \cdot w(c) = \frac{d\Omega(c)}{dc^*} = \frac{d}{dc^*} \sum_{m=1}^n \frac{Q_m}{2\pi} \cdot \ln(c - c_m) \quad (6.2)$$

Here, $*$ denotes the complex conjugate and u and w are the velocity components along the real and the imaginary axes, respectively.

We assume all lateral walls are far enough away from virtual channels, so that we can ignore friction at these boundaries. We implement a no-flow, slip boundary condition at the walls and a zero-potential boundary condition at the opening of the flow cell by the summation of mirrored, virtual counterparts of the sources present in the system on the opposite sides of these boundaries. This is convenient as it only adds additional source terms to be considered and does otherwise not complicate the analysis.

6.4.3 Reproduction of user designed flow patterns

To determine the parameters required to adapt a virtual channel to a spline defined by a user, this spline is discretized at l points in the complex plane. At the k^{th} discretization point, the corresponding complex tangent vector $\vec{t}(c_k) = g_k + i \cdot h_k$ to the spline is determined, with g_k and h_k being the vector components along the real and the imaginary axes, respectively. A symbolic expression for the flow velocity vector at each discretization point can be obtained, as discussed above. The complex cross product between the tangent vector and the velocity vector returns an imaginary number, which is a measure for the area spanned by the two. In case the flow pattern generated collectively by all sources in the flow cell perfectly matches the user defined pattern, the tangent vector and the velocity vector at all discretization points are collinear and the complex cross product is identical zero:

$$\vec{t}(c_k) \times \vec{v}(c_k) = \frac{\vec{t}^*(c_k) \cdot \vec{v}(c_k) - \vec{t}(c_k) \cdot \vec{v}^*(c_k)}{2} = 0 \quad (6.3)$$

When inserting the expression for the velocity vector $\vec{v}(c)$ given above, one obtains a sum with n summands in which the m^{th} summand contains the source strength of the m^{th} source and a pre-factor a_m . Analog sum terms can be written for each discretization point and all terms can be conveniently written in matrix form by grouping the pre-factors in a coefficient matrix:

$$\begin{pmatrix} a_{11} & \dots & a_{1n} \\ \vdots & \ddots & \vdots \\ a_{l1} & \dots & a_{ln} \end{pmatrix} \cdot \begin{pmatrix} Q_1 \\ \vdots \\ Q_n \end{pmatrix} = \begin{pmatrix} 0 \\ \vdots \\ 0 \end{pmatrix} \quad (6.4)$$

To define a stagnation-point at a position c_k , an additional equation can be added to the above system, which simply writes as

$$\vec{v}(c_k) = \frac{d}{dc^*} \sum_{m=1}^n \frac{Q_m}{2\pi} \cdot \ln(c_k - c_m) = 0 \quad (6.5)$$

With sufficiently fine discretization the number of discretization points is much larger than the number of sources, i.e. $l \gg n$, and above system is overdetermined. We solve for the individual source strengths $Q_1 \dots Q_n$ by performing a conventional least-squares fit. To provide a fix reference, we choose a convenient injection flow rate for the injection from the main aperture and set this flow rate as the strength Q_1 of the first source. As the system is linear and the physical main injection flow rate is used as the reference source strength Q_1 , the determined source strengths for the sources in the array can directly be set as flow rates at the corresponding apertures. The described method of matching a user defined pattern using a single least-squares fit was our method of choice, as it is straightforward to implement and provides satisfying performance in matching basic patterns, such as single lines with multiple inflection points. To match more complicated configurations such as virtual channels or multiple virtual channels, genetic algorithm might be better suited to determine the required flow rate at each source.

6.4.4 Setup

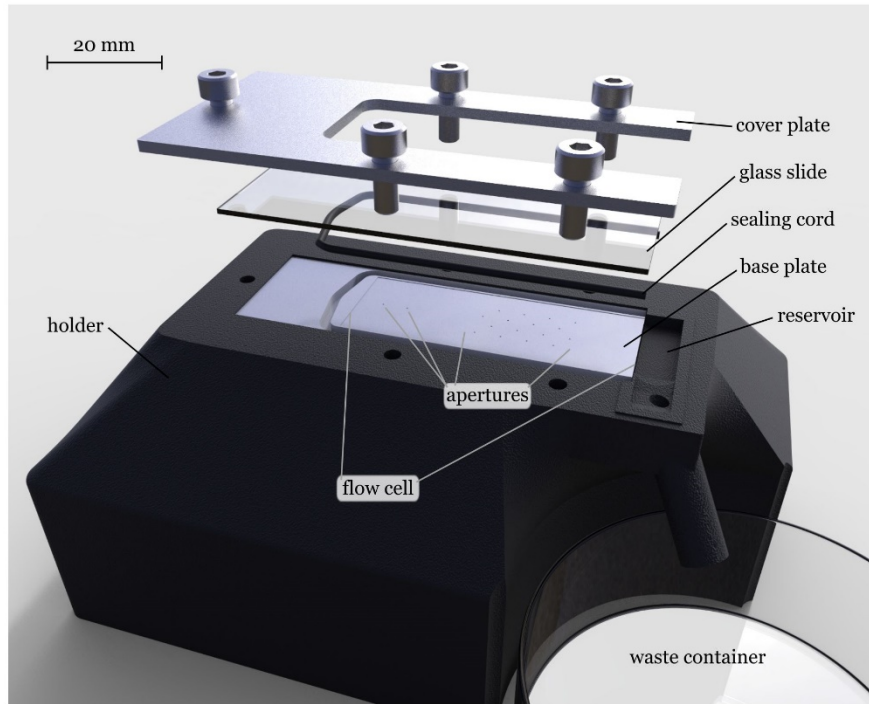


Figure 6.6: Flow cell assembly for generation of reconfigurable flow patterns. The aluminum base plate featuring the recess (which forms the lower part of the flow cell) and the apertures is mounted into a 3D printed holder. The holder has threads to allow the fixation of the top cover plate and fixates the capillaries which are connected to the rear side of the base plate. Further, a small reservoir at the open end of the flow cell ensures a homogeneous open boundary condition by ensuring the open boundary of the flow cell remains submerged. A glass slide is clamped on top of the base plate to close the flow cell by screwing a cover plate to the 3D printed holder. A sealing cord avoids leakage of liquid in between the base plate and the glass slide.

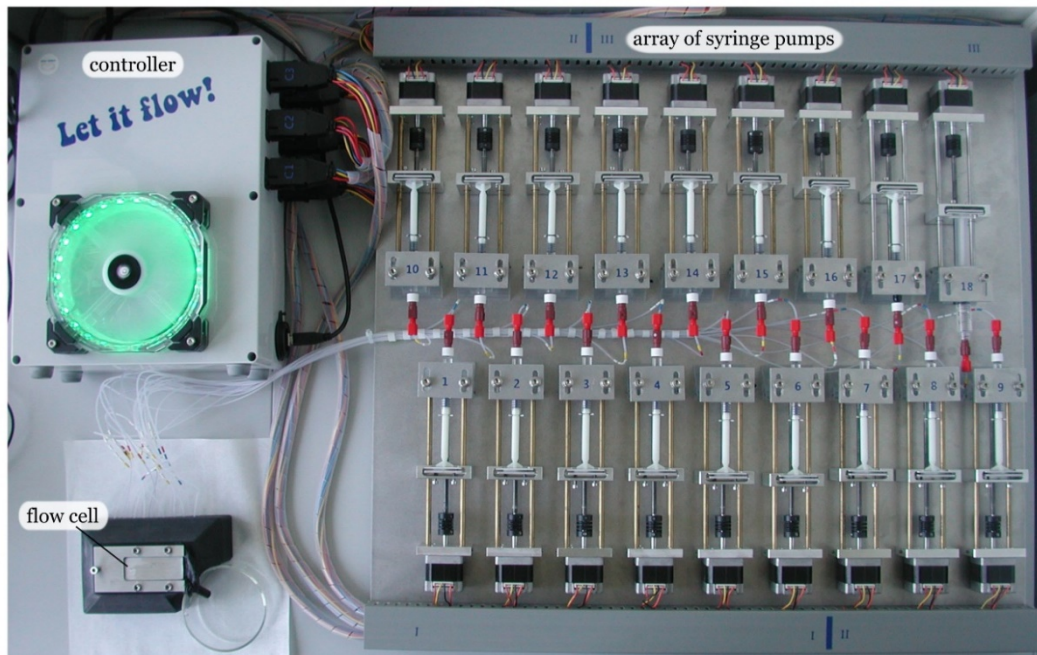


Figure 6.7: Array of syringe pumps for actuation of flow. In the described case, flow was actuated by an array of 18 syringe pumps, which were directly interfaced with the user interface for definition of flow patterns. Instructions to build such systems are available in literature [171], [172]. We adapted a design provided by Dr. Bill Connelly (University of Tasmania) due to its simplicity: <http://www.billconnelly.net/?p=176> (last accessed: Apr. 08, 2019). We used three Arduino Uno microcontroller prototyping boards, each equipped with three commercially available motor-control shields, to control the 18 bipolar stepper motors. A standard PC power supply was used to power all components.

6.4.5 In-situ polymerization

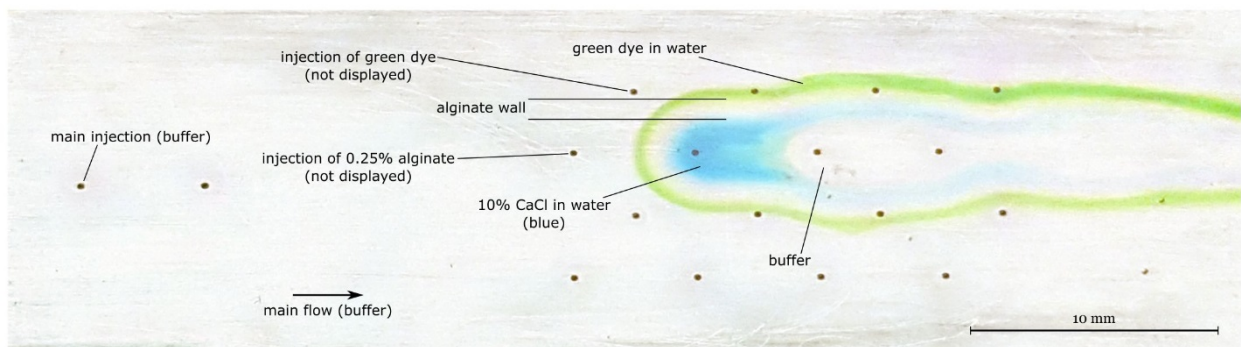


Figure 6.8: In-situ formation of alginate walls. After polymerization of an alginate wall at the interface between two adjacent virtual channels (the inner one containing 10% CaCl_2 , the outer one 0.25% sodium alginate) for 10 s, the flow cell was washed out with water. We then filled the flow cell with green food, which was subsequently flushed out with clear water again. The food dye partially diffused into the polymerized alginate wall and made it visible. This or a similar approach could be used to form in-situ semi-permeable walls in 2D flow cells for e.g. long-term cell studies. We think that it would also be interesting to flow photo-polymerizable materials in or around virtual channels, to stop all flow to suppress advection, and to then illuminate the entire flow cell to create specific microfluidic structure in analogy to established 3D printing approaches.

Chapter 7 Conclusions and outlook

This chapter summarizes work done as part of this dissertation and provides a perspective on potential future research on this topic. This dissertation presents a scaling analysis of HFC-based liquid scanning probes along the dimensions of 1.) efficiency in the use of reagents, 2.) area of interaction, 3.) time of interaction, and, 4.) degrees of freedom in flow control. Within the framework of this analysis, we demonstrated the formation of a surface protein-array by recirculation of minute volumes of reagents, cm-scale IHC-analysis of cancer tissue sections, leakage- and crash-safe operation of liquid scanning probes and the formation of dynamic, channel like flow patterns on top of biological surfaces. Except from this latter package of work, all demonstrated techniques represent a combination of one novel technique or method with the scanning stage MFP platform (see Figure 7.1).

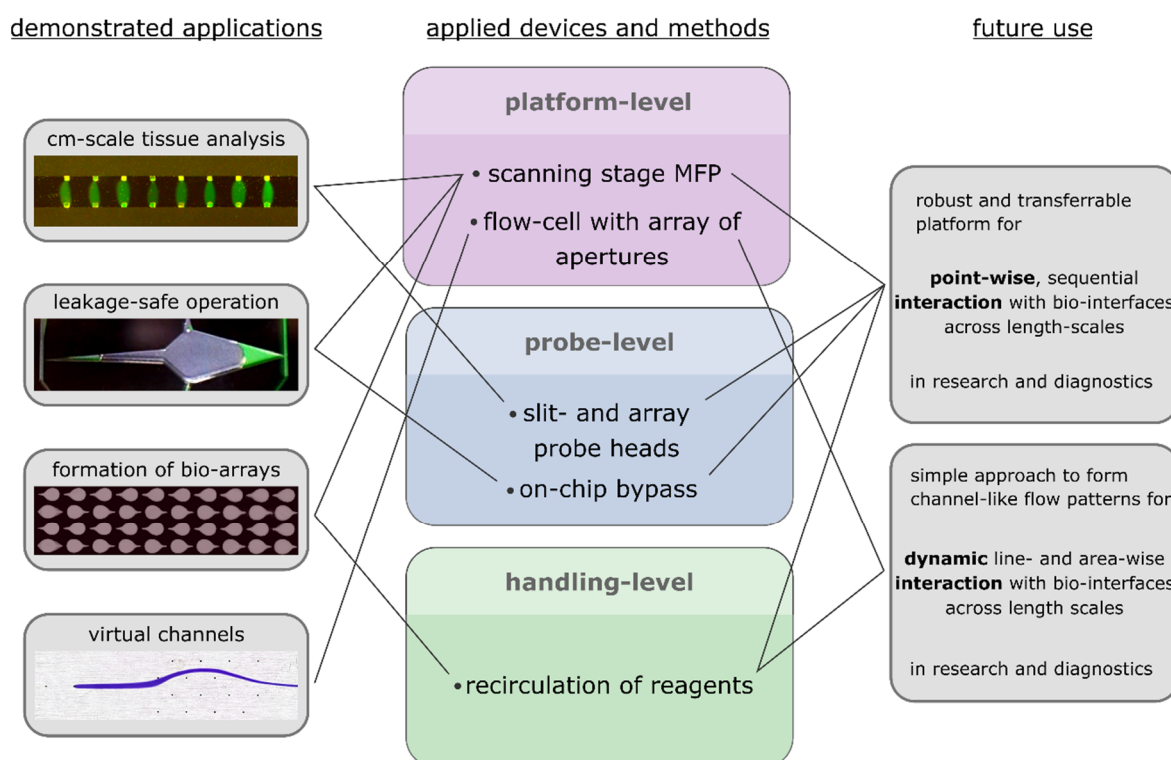


Figure 7.1: Developments presented herein and potential next steps. This dissertation discusses novel concepts to be used with liquid scanning probes and which are introduced on either the platform-level, the probe-level or the liquid handling-level. In this work, these concepts have been demonstrated alone, or exemplarily integrated in the MFP. In a next step, these single techniques should be integrated to allow their combined use, as well as their use with other platforms.

Beyond the experimental demonstrations presented in this thesis, the developed devices and methods are now available as “modules”, which can be grouped and applied in combination, to ideally configure the MFP platform and other HFC-based liquid scanning probes for optimal performance in a specific bio-analytic or diagnostic application. The presented solutions therefore are critical elements in the transfer of related

techniques to relevant applications. It would be a logical next step to combine the flow-cell platform developed for the formation of virtual channels with the method of recirculating minute volumes of reagents.

Alongside working on above discussed aspects, I contributed to the prototyping of a standardized MFP system (see Figure 7.2). I have used several prototype generations in my experimental work shown in this thesis, which both greatly facilitated my experimental workflows and helped to improve the subsequent generations of the prototype system.

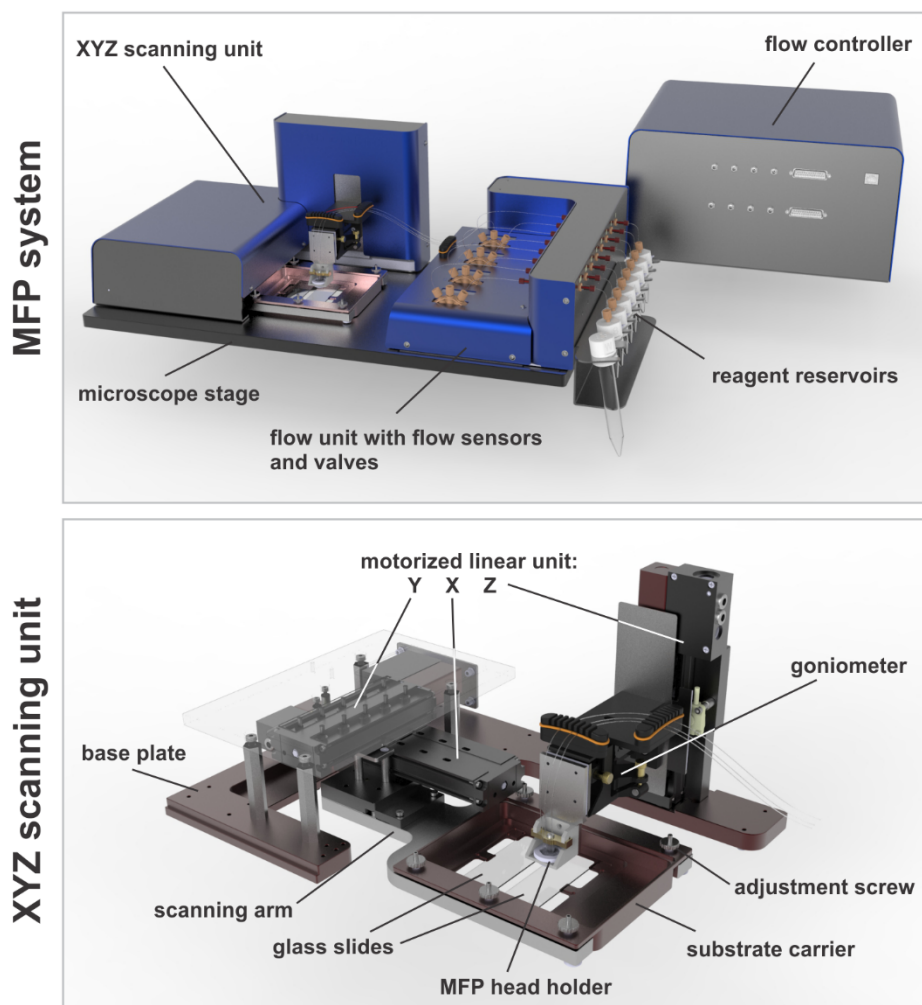


Figure 7.2 Integrated MFP system. Top: Rendering of a CAD model of the most recent MFP system prototype. The microscope, as well as fluidic and electrical connections to the flow controller are not displayed for simplicity. Bottom: The scanning unit comprises a holder for the probe head (horizontal probe head in the displayed version), which is attached to a goniometer for levelling and can be moved along the z-axis, and a sample holder, which can be scanned in the xy-plane. (renderings by Robert Lovchik)

The prototype system consists of three main units:

- The scanning unit, which allows to mount, level and connect a probe head and to scan it relative to a sample (the probe head is moved only in z and remains aligned to the optical axis of the microscope, the sample is moved in x and y).
- The flow unit, which comprises eight flow sensors and four solenoid valves for flow monitoring and routing of flows and a holder for up to eight reagent reservoirs.

- The flow controller, which consists of two 4-channel pressure controllers for controlling the pressure in the reagent reservoirs and electronics for system-level control and communication.

While the flow controller is designed as a bench-top unit, which can be placed behind the microscope, the scanning unit and the flow unit are designed to be used directly on a modified stage of a Nikon TI inverted microscope, as the probe head needs to be aligned with the optical axis of the microscope and the liquid flow paths between the reservoirs and the sample should be as short as possible. The system can control the pressure in the reagent reservoirs either in an open-loop mode, or in closed-loop mode, when using the measured flow rates as feed-back signals. We further developed a custom software interface, which enables the integrated control and script-based operation of all system components.

Main components of the system are the scanning stages (Zaber Technologies Inc., Canada), the solenoid valves (Asco Numatics GmbH, Germany), the flow sensors (Sensirion AG, Switzerland) and the pressure controllers (Fluigent SA, France).

My main contributions to the above system include considerations on the general mechanical design and architecture, as well as selecting the OEM components of the platform, the design and fabrication of custom electronic components of the flow controller, the conceptualization of the control software, as well as assembly and testing work.

7.1 Summary of results

Efficient biopatterning via recirculation of reagents:

- We implemented a method to enable recirculation of sub-microliter volumes of a processing liquid within the probe head.
- We established analytical models to understand the dominating factors in the deposition (deposition of what and where) process.
- We implemented a pressure-based approach for flow control to achieve sub-second switching of the flow direction while minimally perturbing the HFC.
- We demonstrated the patterning of 170 spots of IgG molecules by recirculation of 1.66 μL of processing liquid.
- The recirculation of the processing liquid reduced the consumption of reagents by a factor of 10 compared to deposition with the MFP without recirculation.
- Due highly controlled incubation conditions in a wet environment, a high deposition quality with an inter-spot variability of below 6% was achieved on conventional polystyrene surfaces.
- We demonstrated a first proof-of-concept towards the quantitative detection of IgG molecules in sub-microliter volumes of samples.

Cm-scale interactions using slit-aperture and aperture array probe heads and rapid μHFC :

- We developed design guidelines and scaling laws for slit aperture probe heads and aperture array probe heads through numerical simulations and experimental validation.

- Using slit-aperture probe heads forming an HFC with a width of 1.2mm, we incubated single cores (breast cancer tissue, diameter of 2mm) of a tissue microarray with a primary antibody solution within 2.5min, compared to an incubation time of 30min or more required in conventional methods.
- We introduced the concept of stabilization apertures to suppress cross-talk in arrays of HFCs, which we demonstrated for up to eight parallel HFCs. We used the approach for the 4-plex IHC analysis of tissue sections.
- We facilitated the mm-scale implementation of sequential protocols by introducing novel horizontal probe heads. We demonstrated the concept by implementing three core steps of an IHC analysis routine.
- We developed rapid μ IHC to enable fast and spot-wise immunohistochemical analysis of histological samples. Rapid μ IHC allows to systematically test different combinations of reaction times with the same sample to determine the combination of diagnostic analysis parameters which results in the best trade-off between signal level, contrast and processing time.
- In this work we used both vertical and horizontal probe heads. Each type of probe heads has its own advantages and is therefore suited for different experimental requirements. Comparing vertical and horizontal probe heads, advantages of vertical probe heads are:
 - Simple fabrication (2 etch steps, robust dies)
 - Simple interfacing
 - Simple alignment to sample

Advantages of horizontal heads are:

- Large degree of freedom in the design of apertures (radial HFCs, mm-scale HFCs)
- Eight times higher yield per wafer (more dies per wafer)

Bypass structures for a robust operation of liquid scanning probes:

- We introduced a simple design element, a bypass channel, which allowed improve the operational robustness of any liquid scanning probe relying on re-aspiration of liquid.
- When filled with liquid, the bypass channel acts as a resistive element and passively reacts to the obstruction of channels by re-routing the flow of reagent to avoid spills. Experimental verification shows that the concept is robust against full obstruction of either or both apertures in a conventional probe head.
- When filled with gas, the bypass channel acts as a capacitive element and introduces a phase shift in the transduction of pressure pulses from the injection channel to the aspiration channel. The phase shift and the gap distance can be assessed by optical tracking of the motion of the gas-liquid interfaces in the bypass channel. Experimental results show that the gap distance can be measured for distances between 5 μ m and 25 μ m with drastically increasing signal for low gap distances (maximum observed shift 0.35 rad or 20.1°).

- We developed an analytical model based on nodal voltage analysis (in analogy to electric circuit analysis) to fully understand the working mechanism of proposed solutions and to enable their targeted transfer to specific applications.

Real-time shaping of microfluidic virtual channels:

- Based on an analytical potential flow model, we developed the concept of forming hydrodynamically confined microfluidic flow patterns resembling the morphology and functionality of classical microfluidic channels.
- We developed a demonstrator setup consisting of 1.) a flow cell comprising an 18× array of apertures, which can be directly interfaced with conventional microscope glass slides, 2.) a low-cost multi-channel flow control system with corresponding electronics and firmware and 3.) a design and control software with graphical user interface.
- The established system allows a user to graphically define a desired channel configuration. The software, based on the analytical model then proposes the experimentally viable solution, which is closest to the user input. Upon confirmation of the user, the corresponding channel pattern is then established in about 20s.
- We demonstrated classical microfluidic functionality such as re-routing, splitting merging and mixing of microfluidic flows.
- The established system also enables the implementation of dynamic functions, such as sweeping motions of virtual channels, or the position control of suspended objects.
- Diffusive broadening of virtual channels can be actively countered by additional injection of buffer liquid from the array of apertures to compress the forms flow pattern. This allows for the formation of virtual channels with equal width.
- We demonstrated the versatility of virtual channel by using crossing configurations of virtual channels to implement a sequential immunoassay and by implementing a lysis protocol on a cell block section, which involves local interaction in some steps and global interactions in others.

7.2 Future directions

Efficient biopatterning via recirculation of reagents:

- Beyond *delivering* a reagent to an immersed surface, it would be useful to develop a method for recirculation of a processing liquid to *retrieve* a sample from a surface, e.g. cell lysate, to enrich the sample content in the recirculated volume over time, or to combine samples collected from different locations.
- It would be useful to develop an “reverse immunoassay”: By recirculating a volume of sample over several corresponding detection zones for different incubation times, the deposited amounts of sample allow to compute the sample concentration, given the reaction kinetics are known (and vice versa).

cm-scale interactions using slit-aperture and aperture array probe heads:

- Slit-aperture probes and aperture-array probes could be used for the creation of localized gradients on a surface. Using a slit-aperture design, gradients can be created by supplying different liquids to the injection aperture through independent channels. Probes with aperture-array designs allow the creation of discrete gradients by scanning parallel HFCs over a substrate at an inclined angle (rotation around Z-axis) to enable an overlap between the areas processed with separate HFCs.
- The discussed aperture designs could be implemented in other types of probe heads, which could be 3D-printed or be made by multi-layer lamination of plastic sheets as COC. This would allow the fabrication of probe heads with a large-area apex and mm-scale distance between the injection and aspiration apertures, improving the efficiency in the usage of reagents.
- 3D-printed or multilayer probe heads could be also used to combine the concept of slit-apertures or aperture arrays with the recirculation of processing liquids, which requires additional apertures in the direction of the main axis of flow.

Bypass structures for a robust operation of liquid scanning probes

- Monitoring the gap distance in *ac* mode could be further improved by adding hydrophobic patches to the coupling cavity, to suppress its resistive behavior.
- A higher resolution in tracking the motion of the gas-liquid interfaces in the capacitive bypass by means of e.g. electrode arrays or optical line sensors would increase the range of operation in terms of gap distance and modulation frequency.
- Additional capacitive and resistive flow-path elements could be added to obtain e.g. local extrema of the phase transfer function at specific gap distances, greatly facilitating gap distance control and monitoring in more standardized systems.
- To simultaneously benefit from the characteristics of a resistive and a capacitive bypass, the dc and the ac functionality could be combined. This would ensure leakage free operation and enable a constant monitoring of the gap distance: the differential pressure building up due to an obstruction could be employed to displace the gas in the coupling cavity and open a resistive flow-path for internal bypassing of the processing liquid in the case of severe obstructions. The action of such a design element would be fully reversible and repeatable, as the gas volume would move back to its original position and close the bypass flow path for the processing liquid upon normalization of the differential pressure levels.
- It would be interesting to further develop the idea of using gas-liquid interfaces in tapered structures as indicator elements for pressure differences at the single Pa-level.

Real-time shaping of microfluidic virtual channels

As the concept of forming virtual channels is rather generic, we think of numerous avenues where this concept can be applied, some examples are listed below:

- We have demonstrated virtual channel at widths around 500 μm . A logical next step would be to significantly downscale the channel width by means of using microfabricated apertures and by

downscaling the overall dimension of the aperture array to enable micro-scale flow control along the lateral dimensions.

- We think the functionality of the demonstrated experimental could be augmented through the combination with established microfluidic features, which could be implemented on the top or bottom confining surface of our flow cell. Structures, such as herringbone-shaped grooves [168] would allow to switch on or off the mixing between streams by directing co-flowing liquids across corresponding structures or not. Similarly, specific retention-, collection- or detection-sites could be addressed on demand.
- Pairs of microfluidic apertures can be used to form doublets (pairs of sources and sinks of equal strength), whose outer flow field resembles to the flow around a cylinder. Hence, an array of doublets could be used as an array of posts, to implement sorting of particles based on deterministic lateral displacement (DLD [170]). The advantage of such a virtual pillar array would be that critical design parameters of the pillar array could be modified in real-time to optimize the sorting process.
- The Stokes trap has been used to simultaneously manipulate the position of two suspended objects [72]. Analytical models of corresponding flow-cells with lateral apertures for flow control predict that up to $N = 6$ particles could be controlled in parallel [74]. More degrees of freedom (dF) and thus apertures are required to control more particles, following $dF = N + 1$. This limits the maximum number of particles that can be controlled, because the “zone” of influence of a specific aperture decreases with the spacing between apertures. We anticipate that this constraint can be relaxed, and higher numbers of particles can be simultaneously controlled, by distributing apertures on the top and bottom walls instead just on lateral walls of corresponding flow cells.
- Using an inverse approach, deviations of flow patterns from their original conformation could be used to characterize surface topographies.
- Presented platform and methods could be combined with machine learning techniques to implement self-teaching control systems for the confinement of non-Newtonian liquids, liquids with different viscosities.

References

- [1] N. Convery and N. Gadegaard, "30 years of microfluidics," *Micro Nano Eng.*, vol. 2, pp. 76–91, 2019.
- [2] C. Rensch *et al.*, "Solvent resistant lab-on-chip platform for radiochemistry applications," *Lab Chip*, vol. 14, no. 14, pp. 2556–2564, 2014.
- [3] S. C. Terry, J. H. Jerman, and J. B. Angell, "A gas chromatographic air analyzer fabricated on a silicon wafer," *IEEE Trans. Electron Devices*, vol. 26, no. 12, pp. 1880–1886, 1979.
- [4] G. M. Whitesides, "The origins and the future of microfluidics," *Nature*, vol. 442, no. 7101, pp. 368–373, 2006.
- [5] G. Whitesides, "Microfluidics in Late Adolescence," *Nobel Symp. 162*, vol. arXiv:1802, 2017.
- [6] G. V. Kaigala, R. D. Lovchik, and E. Delamarche, "Microfluidics in the 'Open Space' for Performing Localized Chemistry on Biological Interfaces," *Angew. Chemie Int. Ed.*, vol. 51, no. 45, pp. 11224–11240, 2012.
- [7] G. V. Kaigala, R. D. Lovchik, and E. Delamarche, "Microfluidics in the 'open Space' for performing localized chemistry on biological interfaces," *Angew. Chemie - Int. Ed.*, vol. 51, no. 45, pp. 11224–11240, 2012.
- [8] A. Kashyap, J. Autebert, E. Delamarche, and G. V. Kaigala, "Selective local lysis and sampling of live cells for nucleic acid analysis using a microfluidic probe," *Sci. Rep.*, vol. 6, no. 1, p. 29579, 2016.
- [9] A. A. Meister *et al.*, "FluidFM: Combining Atomic Force Microscopy and Nano uidics in a Universal Liquid Delivery System for Single Cell Applications and Beyond," *Nano Lett.*, vol. 9, no. 6, pp. 2501–2507, 2009.
- [10] P. Novak *et al.*, "Nanoscale live-cell imaging using hopping probe ion conductance microscopy," *Nat. Methods*, vol. 6, no. 4, pp. 279–281, 2009.
- [11] D. G. Dupouy *et al.*, "Continuous quantification of HER2 expression by microfluidic precision immunofluorescence estimates HER2 gene amplification in breast cancer," *Nat. Publ. Gr.*, 2016.
- [12] A. T. Ciftlik, H.-A. H. Lehr, and M. A. M. Gijs, "Microfluidic processor allows rapid HER2 immunohistochemistry of breast carcinomas and significantly reduces ambiguous (2+) read-outs," *Proc. Natl. Acad. Sci.*, vol. 110, no. 14, pp. 5363–5368, 2013.
- [13] M. S. Kim *et al.*, "Breast Cancer Diagnosis Using a Microfluidic Multiplexed Immunohistochemistry Platform," *PLoS One*, vol. 5, no. 5, p. e10441, 2010.
- [14] E. Delamarche, A. Bernard, H. Schmid, B. Michel, and H. Biebuyck, "Patterned delivery of

- immunoglobulins to surfaces using microfluidic networks.," *Science*, vol. 276, no. 5313, pp. 779–781, 1997.
- [15] André Bernard, A. Bruno Michel, and E. Delamarche, "Micromosaic Immunoassays," *Anal. Chem.*, vol. 73, no. 1, pp. 8–12, 2001.
- [16] S. Natarajan *et al.*, "Continuous-flow microfluidic printing of proteins for array-based applications including surface plasmon resonance imaging," *Anal. Biochem.*, vol. 373, no. 1, pp. 141–146, 2008.
- [17] D. Chen *et al.*, "The chemistode: A droplet-based microfluidic device for stimulation and recording with high temporal, spatial, and chemical resolution," *Proc. Natl. Acad. Sci.*, vol. 105, no. 44, pp. 16843–16848, 2008.
- [18] K. H. Kim, N. Moldovan, and H. D. Espinosa, "A nanofountain probe with Sub-100 nm molecular writing resolution," *Small*, vol. 1, no. 6, pp. 632–635, 2005.
- [19] P. K. Hansma, B. Drake, O. Marti, S. A. Gould, and C. B. Prater, "The scanning ion-conductance microscope.," *Science*, vol. 243, no. 4891, pp. 641–3, 1989.
- [20] F. Anariba, J. H. Anh, G.-E. Jung, N.-J. Cho, and S.-J. Cho, "Biophysical Applications of Scanning Ion Conductance Microscopy (Sicm)," *Mod. Phys. Lett. B*, vol. 26, no. 05, p. 1130003, 2012.
- [21] H. Tavana, B. B. B. Mosadegh, and S. Takayama, "Polymeric aqueous biphasic systems for non-contact cell printing on cells: Engineering heterocellular embryonic stem cell niches," *Adv. Mater.*, vol. 22, no. 24, pp. 2628–2631, 2010.
- [22] T. Yaguchi *et al.*, "Micropatterning bacterial suspensions using aqueous two phase systems.," *Analyst*, vol. 135, no. 11, pp. 2848–2852, 2010.
- [23] O. Feinerman and E. Moses, "A picoliter 'fountain-pen' using co-axial dual pipettes," *J. Neurosci. Methods*, vol. 127, no. 1, pp. 75–84, 2003.
- [24] A. Ainla, G. D. M. Jeffries, R. Brune, O. Orwar, and A. Jesorka, "A multifunctional pipette," *Lab Chip*, vol. 12, no. 7, p. 1255, 2012.
- [25] D. Juncker, H. Schmid, and E. Delamarche, "Multipurpose microfluidic probe," *Nat. Mater.*, vol. 4, no. 8, pp. 622–628, 2005.
- [26] G. V. Kaigala, R. D. Lovchik, U. Drechsler, and E. Delamarche, "A Vertical Microfluidic Probe," *Langmuir*, vol. 27, no. 9, pp. 5686–5693, 2011.
- [27] A. A. Kim *et al.*, "SU-8 free-standing microfluidic probes," *Biomicrofluidics*, vol. 11, no. 1, 2017.
- [28] C. M. Perrault, M. A. Qasaimeh, T. Brastaviceanu, K. Anderson, Y. Kabakibo, and D. Juncker, "Integrated microfluidic probe station," *Rev. Sci. Instrum.*, vol. 81, no. 11, 2010.
- [29] N. Ostromohov, M. Bercovici, and G. V. Kaigala, "Delivery of minimally dispersed liquid interfaces for sequential surface chemistry," *Lab Chip*, vol. 16, no. 16, pp. 3015–3023, 2016.
- [30] J. Autebert, J. F. Cors, D. P. Taylor, and G. V. Kaigala, "Convection-Enhanced Biopatterning with Recirculation of Hydrodynamically Confined Nanoliter Volumes of Reagents," *Anal. Chem.*, vol. 88, no. 6, pp. 3235–3242, 2016.

- [31] D. Huber, J. Autebert, and G. V. Kaigala, "Micro fluorescence in situ hybridization (μ FISH) for spatially multiplexed analysis of a cell monolayer," *Biomed. Microdevices*, vol. 18, no. 2, p. 40, 2016.
- [32] S. Matthias and F. Müller, "Asymmetric pores in a silicon membrane acting as massively parallel brownian ratchets," *Nature*, vol. 424, no. 6944, pp. 53–57, 2003.
- [33] M. J. Skaug, C. Schwemmer, S. Fringes, C. D. Rawlings, and A. W. Knoll, "Nanofluidic rocking Brownian motors.," *Science*, vol. 359, no. 6383, pp. 1505–1508, 2018.
- [34] A. Manz *et al.*, "Planar chips technology for miniaturization and integration of separation techniques into monitoring systems: Capillary electrophoresis on a chip," *J. Chromatogr. A*, vol. 593, no. 1–2, pp. 253–258, 1992.
- [35] David C. Duffy, J. Cooper McDonald, and Olivier J. A. Schueller, and G. M. Whitesides*, "Rapid Prototyping of Microfluidic Systems in Poly(dimethylsiloxane)," 1998.
- [36] J. S. Paustian, C. D. Angulo, R. Nery-Azevedo, N. Shi, A. I. Abdel-Fattah, and T. M. Squires, "Direct measurements of colloidal solvophoresis under imposed solvent and solute gradients," *Langmuir*, vol. 31, no. 15, pp. 4402–4410, 2015.
- [37] E. J. Walsh *et al.*, "Microfluidics with fluid walls," *Nat. Commun.*, vol. 8, no. 1, 2017.
- [38] M. T. Guo, A. Rotem, J. A. Heyman, and D. A. Weitz, "Droplet microfluidics for high-throughput biological assays," *Lab Chip*, vol. 12, no. 12, pp. 2146–2155, 2012.
- [39] A. Banerjee, E. Kreit, Y. Liu, J. Heikenfeld, and I. Papautsky, "Reconfigurable virtual electrowetting channels," *Lab Chip*, vol. 12, no. 4, p. 758, 2012.
- [40] B. Zhao, J. S. Moore, and D. J. Beebe, "Surface-Directed Liquid Flow Inside Microchannels," *Science*, vol. 291, no. 5506, pp. 1023–1026, 2001.
- [41] R. Harris and E. O. Ukaejiofo, "Tissue Typing Using a Routine One-Step Lymphocyte Separation Procedure," *Br. J. Haematol.*, vol. 18, no. 2, pp. 229–236, 1970.
- [42] Y.-K. Cho, J.-G. Lee, J.-M. Park, B.-S. Lee, Y. Lee, and C. Ko, "One-step pathogen specific DNA extraction from whole blood on a centrifugal microfluidic device," *Lab Chip*, vol. 7, no. 5, p. 565, 2007.
- [43] R. Nery-Azevedo, A. Banerjee, and T. M. Squires, "Diffusiophoresis in Ionic Surfactant Gradients," *Langmuir*, vol. 33, no. 38, pp. 9694–9702, 2017.
- [44] N. Shi, R. Nery-Azevedo, A. I. Abdel-Fattah, and T. M. Squires, "Diffusiophoretic Focusing of Suspended Colloids," *Phys. Rev. Lett.*, vol. 117, no. 25, pp. 1–5, 2016.
- [45] A. Banerjee, I. Williams, R. N. Azevedo, M. E. Helgeson, and T. M. Squires, "Solute-inertial phenomena: Designing long-range, long-lasting, surface-specific interactions in suspensions," *Proc. Natl. Acad. Sci.*, vol. 113, no. 31, pp. 8612–8617, 2016.
- [46] G. McNab and A. Meisen, "Thermophoresis in liquids," *J. Colloid Interface Sci.*, vol. 44, no. 2, pp. 339–346, 1973.
- [47] R. Piazza and A. Parola, "Thermophoresis in colloidal suspensions," *J. Phys. Condens. Matter*, vol. 20, no. 15, p. 153102, 2008.

- [48] J. Lim, C. Lanni, E. R. Evarts, F. Lanni, R. D. Tilton, and S. A. Majetich, "Magnetophoresis of Nanoparticles," *ACS Nano*, vol. 5, no. 1, pp. 217–226, 2011.
- [49] N. Pamme and A. Manz, "On-chip free-flow magnetophoresis: Continuous flow separation of magnetic particles and agglomerates," *Anal. Chem.*, vol. 76, no. 24, pp. 7250–7256, 2004.
- [50] M. Zborowski, G. R. Ostera, L. R. Moore, S. Milliron, J. J. Chalmers, and A. N. Schechter, "Red Blood Cell Magnetophoresis," *Biophys. J.*, vol. 84, no. 4, pp. 2638–2645, 2003.
- [51] F. Petersson, L. Åberg, A. M. Swärd-Nilsson, and T. Laurell, "Free flow acoustophoresis: Microfluidic-based mode of particle and cell separation," *Anal. Chem.*, vol. 79, no. 14, pp. 5117–5123, 2007.
- [52] P. Augustsson, C. Magnusson, M. Nordin, H. Lilja, and T. Laurell, "Microfluidic, Label-Free Enrichment of Prostate Cancer Cells in Blood Based on Acoustophoresis," *Anal. Chem.*, vol. 84, no. 18, pp. 7954–7962, 2012.
- [53] S.-C. S. Lin, X. Mao, and T. J. Huang, "Surface acoustic wave (SAW) acoustophoresis: now and beyond," *Lab Chip*, vol. 12, no. 16, p. 2766, 2012.
- [54] E. Fällman and O. Axner, "Design for fully steerable dual-trap optical tweezers.," *Appl. Opt.*, vol. 36, no. 10, pp. 2107–2113, 1997.
- [55] D. G. Grier, "A revolution in optical manipulation.," *Nature*, vol. 424, no. 6950, pp. 810–816, 2003.
- [56] J. R. Moffitt, Y. R. Chemla, S. B. Smith, and C. Bustamante, "Recent advances in optical tweezers.," *Annu. Rev. Biochem.*, vol. 77, pp. 205–228, 2008.
- [57] C. S. Effenhauser, A. Manz, and H. M. Widmer, "Glass chips for high-speed capillary electrophoresis separations with submicrometer plate heights," *Anal. Chem.*, vol. 65, no. 19, pp. 2637–2642, 1993.
- [58] E. T. Lagally, P. C. Simpson, and R. A. Mathies, "Monolithic integrated microfluidic DNA amplification and capillary electrophoresis analysis system," *Sensors Actuators B Chem.*, vol. 63, no. 3, pp. 138–146, 2000.
- [59] P. Smejkal *et al.*, "Microfluidic isotachophoresis: A review," *Electrophoresis*, vol. 34, no. 11, pp. 1493–1509, 2013.
- [60] E. Boyko, S. Rubin, A. D. Gat, and M. Bercovici, "Flow patterning in Hele-Shaw configurations using non-uniform electro-osmotic slip," *Phys. Fluids*, vol. 27, no. 10, p. 102001, 2015.
- [61] F. Paratore, V. Bacheva, G. V. Kaigala, and M. Bercovici, "Dynamic microscale flow patterning using electrical modulation of zeta potential.," *Proc. Natl. Acad. Sci. U. S. A.*, vol. 116, no. 21, pp. 10258–10263, 2019.
- [62] W. A. Bonner, H. R. Hulett, R. G. Sweet, and L. A. Herzenberg, "Fluorescence Activated Cell Sorting," *Rev. Sci. Instrum.*, vol. 43, no. 3, pp. 404–409, 1972.
- [63] D. Huber, A. Oskoei, X. Casadevall i Solvas, A. deMello, and G. V. Kaigala, "Hydrodynamics in Cell Studies," *Chem. Rev.*, vol. 118, no. 4, pp. 2042–2079, 2018.
- [64] R. B. Bird, W. E. Stewart, and E. N. Lightfoot, *Transport phenomena*. J. Wiley, 2007.

- [65] G.-B. Lee, C.-C. Chang, S.-B. Huang, and R.-J. Yang, "The hydrodynamic focusing effect inside rectangular microchannels," *J. Micromechanics Microengineering*, vol. 16, no. 5, pp. 1024–1032, 2006.
- [66] Y. Zhao, Q. Li, and X. Hu, "Universally applicable three-dimensional hydrodynamic focusing in a single-layer channel for single cell analysis," *Anal. Methods*, vol. 10, no. 28, pp. 3489–3497, 2018.
- [67] P. K. Shivhare, A. Bhadra, P. Sajeesh, A. Prabhakar, and A. K. Sen, "Hydrodynamic focusing and interdistance control of particle-laden flow for microflow cytometry," *Microfluid. Nanofluidics*, vol. 20, no. 6, p. 86, 2016.
- [68] G. K. Batchelor, *An introduction to fluid dynamics*. Cambridge University Press, 1999.
- [69] H. Bruus, *Theoretical microfluidics*. Oxford University Press, 2008.
- [70] P. J. A. Kenis, R. F. Ismagilov, and G. M. Whitesides, "Microfabrication Inside Capillaries Using Multiphase Laminar Flow Patterning," *Science*, vol. 285, no. 5424, pp. 83–85, 1999.
- [71] S. K. Y. Tang, C. A. Stan, and G. M. Whitesides, "Dynamically reconfigurable liquid-core liquid-cladding lens in a microfluidic channel," *Lab Chip*, vol. 8, no. 3, p. 395, 2008.
- [72] A. Shenoy, C. V Rao, and C. M. Schroeder, "Stokes trap for multiplexed particle manipulation and assembly using fluidics," *Proc. Natl. Acad. Sci. U. S. A.*, vol. 113, no. 15, pp. 3976–3981, 2016.
- [73] D. B. Wolfe *et al.*, "Dynamic control of liquid-core/liquid-cladding optical waveguides.," *Proc. Natl. Acad. Sci. U. S. A.*, vol. 101, no. 34, pp. 12434–8, 2004.
- [74] T. M. Schneider, S. Mandre, and M. P. Brenner, "Algorithm for a Microfluidic Assembly Line," *Phys. Rev. Lett.*, vol. 106, no. 9, p. 094503, 2011.
- [75] D. Di Carlo, "Inertial microfluidics.," *Lab Chip*, vol. 9, no. 21, pp. 3038–3046, 2009.
- [76] H. Amini *et al.*, "Engineering fluid flow using sequenced microstructures," *Nat. Commun.*, vol. 4, 2013.
- [77] J. M. Martel and M. Toner, "Inertial Focusing in Microfluidics," *Annu. Rev. Biomed. Eng.*, vol. 16, no. 1, pp. 371–396, 2014.
- [78] W. R. Dean, "Fluid Motion in a Curved Channel," *Proc. R. Soc. A Math. Phys. Eng. Sci.*, vol. 121, no. 787, pp. 402–420, 1928.
- [79] B. P. Ho and L. G. Leal, "Inertial migration of rigid spheres in two-dimensional unidirectional flows," *J. Fluid Mech.*, vol. 65, no. 2, pp. 365–400, 1974.
- [80] J. Zhang *et al.*, "Fundamentals and Applications of Inertial Microfluidics: A Review," *Lab Chip*, vol. 16, pp. 10–34, 2016.
- [81] I. D. Johnston, M. B. McDonnell, C. K. L. Tan, D. K. McCluskey, M. J. Davies, and M. C. Tracey, "Dean flow focusing and separation of small microspheres within a narrow size range," *Microfluid. Nanofluidics*, vol. 17, no. 3, pp. 509–518, 2014.
- [82] D. Di Carlo, D. Irimia, R. G. Tompkins, and M. Toner, "Continuous inertial focusing, ordering, and separation of particles in microchannels.," *Proc. Natl. Acad. Sci. U. S. A.*, vol. 104, no. 48,

- pp. 18892–18897, 2007.
- [83] M. G. Lee, S. Choi, and J.-K. Park, “Three-dimensional hydrodynamic focusing with a single sheath flow in a single-layer microfluidic device,” *Lab Chip*, vol. 9, no. 21, p. 3155, 2009.
- [84] D. R. Gossett *et al.*, “Label-free cell separation and sorting in microfluidic systems,” *Anal. Bioanal. Chem.*, vol. 397, no. 8, pp. 3249–3267, 2010.
- [85] M. E. Warkiani *et al.*, “Ultra-fast, label-free isolation of circulating tumor cells from blood using spiral microfluidics,” *Nat. Protoc.*, vol. 11, no. 1, pp. 134–148, 2016.
- [86] E. Ozkumur *et al.*, “Inertial focusing for tumor antigen-dependent and -independent sorting of rare circulating tumor cells.,” *Sci. Transl. Med.*, vol. 5, no. 179, p. 179ra47, 2013.
- [87] D. Stoecklein, C.-Y. Wu, D. Kim, D. Di Carlo, and B. Ganapathysubramanian, “Optimization of micropillar sequences for fluid flow sculpting,” *Phys. Fluids*, vol. 28, p. 12003, 2016.
- [88] M. Frankowski *et al.*, “Microflow Cytometers with Integrated Hydrodynamic Focusing,” *Sensors*, vol. 13, no. 4, pp. 4674–4693, 2013.
- [89] J. P. Golden *et al.*, “Multi-wavelength microflow cytometer using groove-generated sheath flow,” *Lab Chip*, vol. 9, no. 13, p. 1942, 2009.
- [90] X. Mao, J. R. Waldeisen, and T. J. Huang, “‘Microfluidic drifting’—implementing three-dimensional hydrodynamic focusing with a single-layer planar microfluidic device,” *Lab Chip*, vol. 7, no. 10, p. 1260, 2007.
- [91] A. M. Leshansky, A. Bransky, N. Korin, and U. Dinnar, “Tunable Nonlinear Viscoelastic ‘Focusing’ in a Microfluidic Device,” *Phys. Rev. Lett.*, vol. 98, no. 23, p. 234501, 2007.
- [92] D. Li, X. Lu, and X. Xuan, “Viscoelastic Separation of Particles by Size in Straight Rectangular Microchannels: A Parametric Study for a Refined Understanding,” *Anal. Chem.*, vol. 88, no. 24, pp. 12303–12309, 2016.
- [93] M. A. Qasaimeh, T. Gervais, and D. Juncker, “Microfluidic quadrupole and floating concentration gradient.,” *Nat. Commun.*, vol. 2, no. 1, p. 464, 2011.
- [94] H. M. Haitjema, *Analytic element modeling of groundwater flow*. Academic Press, 1995.
- [95] P.-A. Goyette, É. Boulais, F. Normandeau, G. Laberge, D. Juncker, and T. Gervais, “Microfluidic multipoles theory and applications,” *Nat. Commun.*, vol. 10, no. 1, p. 1781, 2019.
- [96] H. Nygren and M. Stenberg, “Immunochemistry at interfaces.,” *Immunology*, vol. 66, no. 3, pp. 321–7, Mar. 1989.
- [97] H. Chandra, P. J. Reddy, and S. Srivastava, “Protein microarrays and novel detection platforms,” *Expert Rev. Proteomics*, vol. 8, no. 1, pp. 61–79, 2011.
- [98] R. L. Stears, T. Martinsky, and M. Schena, “Trends in microarray analysis,” *Nat. Med.*, vol. 9, no. 1, pp. 140–145, 2003.
- [99] T. Kodadek, “Protein microarrays: prospects and problems,” *Chem. Biol.*, vol. 8, no. 2, pp. 105–115, 2001.
- [100] A. Dias, D. Kingsley, and D. Corr, “Recent Advances in Bioprinting and Applications for Biosensing,” *Biosensors*, vol. 4, no. 2, pp. 111–136, 2014.

- [101] J. T. Delaney, J. Smith, and U. S. Schubert, "Inkjet printing of proteins," *Soft Matter*, vol. 5, no. 24, p. 4866, 2009.
- [102] V. Romanov *et al.*, "A critical comparison of protein microarray fabrication technologies," *Analyst*, vol. 139, no. 6, p. 1303, 2014.
- [103] H. Tavana *et al.*, "Nanolitre liquid patterning in aqueous environments for spatially defined reagent delivery to mammalian cells," *Nat. Mater.*, vol. 8, no. 9, pp. 736–741, 2009.
- [104] G. MacBeath *et al.*, "Printing proteins as microarrays for high-throughput function determination," *Science (80-.)*, vol. 289, no. 5485, pp. 1760–3, 2000.
- [105] ArrayIt Corp., "ArrayIt pinspotting system," Available: <http://www.arrayit.com/>.
- [106] Bio-Rad Corp., "Bio-Rad pinspotting system," Available: <http://www.bio-rad.com>.
- [107] H. Hu and R. G. Larson, "Marangoni Effect Reverses Coffee-Ring Depositions," *J. Phys. Chem. B*, vol. 110, no. 14, pp. 7090–7094, 2006.
- [108] A. Bernard, E. Delamarche, H. Schmid, B. Michel, H. R. Bosshard, and H. Biebuyck, "Printing Patterns of Proteins," *Langmuir*, vol. 14, no. 9, pp. 2225–2229, 1998.
- [109] A. Liberski, R. Zhang, and M. Bradley, "Inkjet fabrication of polymer microarrays and grids-- solving the evaporation problem.," *Chem. Commun. (Camb.)*, no. 3, pp. 334–336, 2009.
- [110] I. Barbulovic-Nad, M. Lucente, Y. Sun, M. Zhang, A. R. Wheeler, and M. Bussmann, "Bio-microarray fabrication techniques--a review.," *Crit. Rev. Biotechnol.*, vol. 26, no. 4, pp. 237–259, 2006.
- [111] J. Ziegler, M. Zimmermann, P. Hunziker, and E. Delamarche, "High-performance immunoassays based on through-stencil patterned antibodies and capillary systems," *Anal. Chem.*, vol. 80, no. 5, pp. 1763–1769, 2008.
- [112] M. O. Reese, R. M. van Dam, A. Scherer, and S. R. Quake, "Microfabricated fountain pens for high-density DNA arrays.," *Genome Res.*, vol. 13, no. 10, pp. 2348–52, 2003.
- [113] J.-U. Park *et al.*, "High-resolution electrohydrodynamic jet printing.," *Nat. Mater.*, vol. 6, no. 10, pp. 782–789, 2007.
- [114] A. Bruckbauer *et al.*, "Writing with DNA and Protein Using a Nanopipet for Controlled Delivery," *J. Am. Chem. Soc.*, vol. 124, no. 30, pp. 8810–8811, 2002.
- [115] T. M. Squires, R. J. Messinger, and S. R. Manalis, "Making it stick: convection, reaction and diffusion in surface-based biosensors.," *Nat. Biotechnol.*, vol. 26, no. 4, pp. 417–426, 2008.
- [116] H.-P. P. Chou, M. A. Unger, and S. R. Quake, "A microfabricated rotary pump," *Biomed. Microdevices*, vol. 3, no. 4, pp. 323–330, 2001.
- [117] P. K. Yuen, G. Li, Y. Bao, and U. R. Muller, "Microfluidic devices for fluidic circulation and mixing improve hybridization signal intensity on DNA arrays.," *Lab Chip*, vol. 3, no. 9731, pp. 46–50, 2003.
- [118] J. M. Ottino and S. Wiggins, "Introduction: mixing in microfluidics.," *Philos. Trans. A. Math. Phys. Eng. Sci.*, vol. 362, no. 1818, pp. 923–935, 2004.
- [119] N.-T. Nguyen and Z. Wu, "Micromixers—a review," *J. Micromechanics Microengineering*, vol.

- 15, no. 2, pp. R1–R16, 2005.
- [120] J. Autebert, A. Kashyap, R. D. Lovchik, E. Delamarche, and G. V. Kaigala, “Hierarchical hydrodynamic flow confinement: Efficient use and retrieval of chemicals for microscale chemistry on surfaces,” *Langmuir*, vol. 30, no. 12, pp. 3640–3645, 2014.
- [121] K. Murphy, P. Travers, and M. Walport, *Janeway’s Immunobiology*, 7th ed., Garland Science, 2008.
- [122] J. S. Newman and K. E. Thomas-Alyea, *Electrochemical systems*. J. Wiley, 2004.
- [123] J. F. Cors, R. D. Lovchik, E. Delamarche, and G. V. Kaigala, “A compact and versatile microfluidic probe for local processing of tissue sections and biological specimens,” *Rev. Sci. Instrum.*, vol. 85, no. 3, p. 034301, 2014.
- [124] X. F. van Kooten, J. Autebert, and G. V. Kaigala, “Passive removal of immiscible spacers from segmented flows in a microfluidic probe,” *Appl. Phys. Lett.*, vol. 106, no. 7, p. 074102, 2015.
- [125] T. Jøssang, J. Feder, and E. Rosenqvist, “Photon correlation spectroscopy of human IgG,” *J. Protein Chem.*, vol. 7, no. 2, pp. 165–71, 1988.
- [126] T. G. Fernandes, M. M. Diogo, D. S. Clark, J. S. Dordick, and J. M. S. S. Cabral, “High-throughput cellular microarray platforms: applications in drug discovery, toxicology and stem cell research,” *Trends Biotechnol.*, vol. 27, no. 6, pp. 342–349, 2009.
- [127] S.-R. Shi, Y. Shi, and C. R. Taylor, “Antigen retrieval immunohistochemistry: review and future prospects in research and diagnosis over two decades,” *J. Histochem. Cytochem.*, vol. 59, no. 1, pp. 13–32, 2011.
- [128] O. I. O. I. Berthuy, L. J. L. J. Blum, and C. A. Marquette, “Cells on chip for multiplex screening,” *Biosens. Bioelectron.*, vol. 76, no. c, pp. 29–37, 2016.
- [129] S. G. Hays, W. G. Patrick, M. Ziesack, N. Oxman, and P. A. Silver, “Better together: Engineering and application of microbial symbioses,” *Curr. Opin. Biotechnol.*, vol. 36, pp. 40–49, 2015.
- [130] A. P. Blanchard, R. J. Kaiser, and L. E. Hood, “High-density oligonucleotide arrays,” *Biosens. Bioelectron.*, vol. 11, no. 6–7, pp. 687–690, 1996.
- [131] C. M. Waters and B. L. Bassler, “Quorum sensing: cell-to-cell communication in bacteria,” *Annu. Rev. Cell Dev. Biol.*, vol. 21, no. 1, pp. 319–346, 2005.
- [132] G. Macbeath, “High-Throughput Function Determination Printing Proteins as Microarrays for High-Throughput Function Determination,” *Sci. York*, vol. 1760, no. 2000, pp. 1760–1763, 2009.
- [133] T. Yaguchi *et al.*, “Micropatterning bacterial suspensions using aqueous two phase systems,” *Analyst*, vol. 135, no. 11, pp. 2848–2852, 2010.
- [134] A. Waldbaur, B. Waterkotte, K. Schmitz, and B. E. Rapp, “Maskless projection lithography for the fast and flexible generation of grayscale protein patterns,” *Small*, vol. 8, no. 10, pp. 1570–1578, 2012.
- [135] R. D. Piner, J. Zhu, F. Xu, S. Hong, and C. A. Mirkin, “‘Dip-Pen’ Nanolithography,” *Science (80-.)*, vol. 283, no. 5402, pp. 661–663, 1999.

- [136] D. S. Ginger, H. Zhang, and C. A. Mirkin, "The Evolution of Dip-Pen Nanolithography," *Angew. Chemie - Int. Ed.*, vol. 43, no. 1, pp. 30–45, 2004.
- [137] M. Zhang, B. Su, F. Cortés-Salazar, M. Hojeij, and H. H. Girault, "SECM photography," *Electrochem. commun.*, vol. 10, no. 5, pp. 714–718, 2008.
- [138] F. Cortés-Salazar *et al.*, "Soft stylus probes for scanning electrochemical microscopy," *Anal. Chem.*, vol. 81, no. 16, pp. 6889–6896, 2009.
- [139] R. D. Lovchik, G. V. Kaigala, M. Georgiadis, and E. Delamarche, "Micro-immunohistochemistry using a microfluidic probe," *Lab Chip*, vol. 12, no. 6, p. 1040, 2012.
- [140] A. Ainla, E. T. Jansson, N. Stepanyants, O. Orwar, and A. Jesorka, "A microfluidic pipette for single-cell pharmacology," *Anal. Chem.*, vol. 82, no. 11, pp. 4529–4536, 2010.
- [141] F. V. Peale *et al.*, "Tissue microarray (TMA) technology: Miniaturized pathology archives for high-throughput in situ studies," *J. Pathol.*, vol. 195, no. 1, pp. 72–79, 2001.
- [142] J. F. Cors, A. Stucki, and G. V. Kaigala, "Hydrodynamic thermal confinement: creating thermochemical microenvironments on surfaces," *Chem. Commun.*, vol. 52, no. 88, pp. 13035–13038, 2016.
- [143] J. F. Cors, A. Kashyap, A. Fomitcheva Khartchenko, P. Schraml, and G. V. Kaigala, "Tissue lithography: Microscale dewaxing to enable retrospective studies on formalin-fixed paraffin-embedded (FFPE) tissue sections," *PLoS One*, vol. 12, no. 5, p. e0176691, 2017.
- [144] D. P. D. P. D. P. Taylor, I. Zeaf, R. D. R. D. R. D. R. D. Lovchik, and G. V. Kaigala, "Centimeter-Scale Surface Interactions Using Hydrodynamic Flow Confinements," *Langmuir*, vol. 32, no. 41, pp. 10537–10544, 2016.
- [145] A. Sarkar, S. Kolitz, D. A. Lauffenburger, and J. Han, "Microfluidic probe for single-cell analysis in adherent tissue culture," *Nat. Commun.*, vol. 5, no. 1, p. 3421, 2014.
- [146] D. Momotenko, F. Cortes-Salazar, A. Lesch, G. Wittstock, and H. H. Girault, "Microfluidic Push–Pull Probe for Scanning Electrochemical Microscopy," *Anal. Chem.*, vol. 83, no. 13, pp. 5275–5282, 2011.
- [147] O. Guillaume-Gentil, T. Zambelli, and J. A. Vorholt, "Isolation of single mammalian cells from adherent cultures by fluidic force microscopy," *Lab Chip*, vol. 14, no. 2, pp. 402–14, 2014.
- [148] A. Oskoei and G. V. Kaigala, "Deep-reaching hydrodynamic flow confinement: Micrometer-scale liquid localization for open substrates with topographical variations," *IEEE Trans. Biomed. Eng.*, vol. 64, no. 6, pp. 1261–1269, 2017.
- [149] M. Hitzbleck, G. V. Kaigala, E. Delamarche, and R. D. Lovchik, "The floating microfluidic probe: Distance control between probe and sample using hydrodynamic levitation," *Appl. Phys. Lett.*, vol. 104, no. 26, pp. 1–5, 2014.
- [150] R. H. Silverman, "High-resolution ultrasound imaging of the eye - a review," *Clin. Experiment. Ophthalmol.*, vol. 37, no. 1, pp. 54–67, 2009.
- [151] K. W. Oh, K. Lee, B. Ahn, and E. P. Furlani, "Design of pressure-driven microfluidic networks using electric circuit analogy," *Lab Chip*, vol. 12, no. 3, pp. 515–545, 2012.
- [152] D. C. Leslie *et al.*, "Frequency-specific flow control in microfluidic circuits with passive

- elastomeric features," *Nat. Phys.*, vol. 5, no. 3, pp. 231–235, 2009.
- [153] M. E. Van Valkenburg, "Impedance functions and network theorems," in *Network analysis*, 3rd ed., Prentice-Hall Of India Pvt. Limited, 1974
- [154] S. M. Karlsson and J. Bigun, "Lip-motion events analysis and lip segmentation using optical flow," *2012 IEEE Comput. Soc. Conf. Comput. Vis. Pattern Recognit. Work.*, pp. 138–145, 2012.
- [155] M. Bahrami, M. M. Yovanovich, and J. R. Culham, "Pressure Drop of Fully-Developed, Laminar Flow in Microchannels of Arbitrary Cross-Section," *J. Fluids Eng.*, vol. 128, no. 5, p. 1036, 2006.
- [156] T. M. Squires and S. R. Quake, "Microfluidics: Fluid physics at the nanoliter scale," *Rev. Mod. Phys.*, vol. 77, no. 3, pp. 977–1026, 2005.
- [157] T. Thorsen, S. J. Maerkl, and S. R. Quake, "Microfluidic large-scale integration.," *Science*, vol. 298, no. 5593, pp. 580–4, 2002.
- [158] L. M. Fidalgo and S. J. Maerkl, "A software-programmable microfluidic device for automated biology," *Lab Chip*, vol. 11, no. 9, p. 1612, 2011.
- [159] K. A. Shaikh *et al.*, "A modular microfluidic architecture for integrated biochemical analysis.," *Proc. Natl. Acad. Sci. U. S. A.*, vol. 102, no. 28, pp. 9745–50, 2005.
- [160] M. Abdelgawad and A. R. Wheeler, "The digital revolution: A new paradigm for microfluidics," *Adv. Mater.*, vol. 21, no. 8, pp. 920–925, 2009.
- [161] M. Dhindsa *et al.*, "Virtual electrowetting channels: electronic liquid transport with continuous channel functionality," *Lab Chip*, vol. 10, no. 7, p. 832, 2010.
- [162] A. A. Darhuber, J. P. Valentino, S. M. Troian, and S. Wagner, "Thermocapillary actuation of droplets on chemically patterned surfaces by programmable microheater arrays," *J. Microelectromechanical Syst.*, vol. 12, no. 6, pp. 873–879, 2003.
- [163] X. Ding *et al.*, "Surface acoustic wave microfluidics," *Lab Chip*, vol. 13, no. 18, p. 3626, 2013.
- [164] G. A. Cooksey, C. G. Sip, and A. Folch, "A multi-purpose microfluidic perfusion system with combinatorial choice of inputs, mixtures, gradient patterns, and flow rates," *Lab Chip*, vol. 9, no. 3, pp. 417–426, 2009.
- [165] P. Skafte-Pedersen, C. G. Sip, A. Folch, and M. Dufva, "Modular microfluidic systems using reversibly attached PDMS fluid control modules," *J. Micromechanics Microengineering*, vol. 23, no. 5, p. 055011, 2013.
- [166] O. Feinerman and E. Moses, "A picoliter 'fountain-pen' using co-axial dual pipettes," *J. Neurosci. Methods*, vol. 127, no. 1, pp. 75–84, 2003.
- [167] K. V. Christ *et al.*, "Design of hydrodynamically confined microfluidics: controlling flow envelope and pressure.," *Lab Chip*, vol. 11, no. 8, pp. 1491–1501, 2011.
- [168] A. D. Stroock, S. K. W. Dertinger, A. Ajdari, I. Mezic, H. a Stone, and G. M. Whitesides, "Chaotic mixer for microchannels.," *Science*, vol. 295, no. 5555, pp. 647–651, 2002.
- [169] W. H. Tan and S. Takeuchi, "A trap-and-release integrated microfluidic system for dynamic

microarray applications," *Proc. Natl. Acad. Sci. U. S. A.*, vol. 104, no. 4, pp. 1146–1151, 2007.

- [170] L. R. Huang, E. C. Cox, R. H. Austin, and J. C. Sturm, "Continuous particle separation through deterministic lateral displacement," *Science*, vol. 304, no. 5673, pp. 987–990, 2004.
- [171] B. Wijnen, E. J. Hunt, G. C. Anzalone, and J. M. Pearce, "Open-Source Syringe Pump Library," *PLoS One*, vol. 9, no. 9, p. e107216, 2014.
- [172] V. E. Garcia, J. Liu, and J. L. DeRisi, "Low-cost touchscreen driven programmable dual syringe pump for life science applications," *HardwareX*, vol. 4, p. e00027, 2018.

Curriculum Vitae

DAVID TAYLOR

Alte Landstrasse 10, 8800 Thalwil, Switzerland | +41 76 624 4551 | david.weinsfeld@gmail.com |
Date of Birth: May 05, 1987 | Married, 2 Children | Nationality: German |
ORCID ID: 0000-0001-9759-4084



OBJECTIVE

I strive to expand my scientific and technical expertise in a leading research group to pursue a career in academic research.

EDUCATION

- | | |
|---|------------------------|
| Microsystems and Microelectronics Doctoral School (EDMI)
<i>École polytechnique fédérale de Lausanne</i> | Dec. 2015 - Oct. 2019 |
| Advisors: Prof. Philippe Renaud (EPFL), Dr. Govind Kaigala (IBM Research) | |
| <ul style="list-style-type: none">• Doctoral courses: Quantum Optics, Physics of Biological Macromolecules, Design of Experiments, Energy Autonomous Wireless Smart Systems | |
| Master of Science, Micro- and Nanotechnology
<i>Munich University of Applied Sciences, Germany</i> | Mar. 2013 - Sept. 2014 |
| <ul style="list-style-type: none">• Main courses: Quantum mechanics, physics of low dimensional structures, semiconductor physics | |
| Bachelor of Science, Engineering Physics
<i>Munich University of Applied Sciences, Germany</i> | Oct. 2009 - Feb. 2013 |
| <ul style="list-style-type: none">• Main courses: Mechanics, thermodynamics, electrodynamics, optics, quantum mechanics | |
| Abitur (A-level equivalent)
<i>Gymnasium Hilpoltstein, Germany</i> | Sept. 1997 – Jun. 2006 |
| <ul style="list-style-type: none">• Main courses: Mathematics, Biology, French | |

WORK EXPERIENCE

- | | |
|--|-----------------------|
| UCSB, Department of Chemical Engineering (Santa Barbara, US)
<i>Visiting fellow – SNF Doc.Mobility</i> | Jan. 2019 - Aug. 2019 |
| Host: Prof. Todd Squires | |
| <ul style="list-style-type: none">• Measurement and analysis of solvophoresis and diffusiophoresis by interferometric assessment of concentration gradients | |
| IBM Research – Zurich (Rüschlikon, CH)
<i>Pre-Doc</i> | Apr. 2015 – Nov. 2018 |
| Advisor: Dr. Govind Kaigala | |
| <ul style="list-style-type: none">• Analysis of mass transport phenomena in microfluidic probe systems• Experimental verification of theoretical analysis and validation of new device concepts• Consulting of external partners | |

IBM Research – Zurich (Rüschlikon, CH)

Apr. 2014 – Mar. 2015

Working student, Intern

Advisors: Dr. Emmanuel Delamarche, Dr. Govind Kaigala

- Analysis of mass transport phenomena in microfluidic probe systems
- Master thesis "A manually operable microfluidic probe system"

GE Global Research (Garching, DE)

Oct. 2011 - Mar. 2014

Working student, Intern

Advisor: Dr. Christian Rensch

- Bachelor thesis "Optimization of a microfluidic valve for lab-on-chip systems"
- Design, sourcing and setup of microfluidic valve test setup, measurement, automation and data acquisition utilizing LabView
- Simulation of valve behavior in integrated systems with Simulink

Airbus Helicopters (Ottobrunn, DE)

May 2011 - Sept. 2011

Intern

Advisor: Dr. Patrizia Dabalà

- Characterization of optical aircraft mission equipment, such as displays and night vision systems
- Study on confocal measurement system for angular characterization of display systems

German Army, NATO Response Force (Kerpen, DE)

Oct. 2006 - Oct. 2008

Private First Class

- Deputy group leader in a reconnaissance infantry unit during an ISAF mission

PUBLICATIONS IN BOOKS AND JOURNALS

- [Taylor, D. P.](#); Kaigala, G. V. "Reconfigurable microfluidics: real-time shaping of virtual channels through hydrodynamic forces." *Small* (**under review: smll.201902854**)
- [Taylor, D. P.](#); Kaigala, G. V. "Fluidic bypass structures for improving the robustness of liquid scanning probes." *IEEE Transactions on Biomedical Engineering*, **2019**, DOI: 10.1109/TBME.2018.2890602
- Lovchik, R. D.; [Taylor, D. P.](#); Zeaf, I.; Delamarche, E.; Kaigala, G. V. "Hydrodynamic flow confinement-assisted immunohistochemistry from micrometer to millimeter-scale," *Open-Space Microfluidics: Concepts, Implementations, Applications*. Wiley-VCH Verlag GmbH, **2018** (ISBN: 978-3-527-34038-5)
- Cors, J. F.; Autebert, J.; Kashyap, A.; [Taylor, D. P.](#); Lovchik, R. D.; Delamarche, E.; Kaigala, G. V. "Hierarchical Hydrodynamic Flow Confinement (hHFC) and Recirculation for performing Microscale Chemistry on Surfaces," *Open-Space Microfluidics: Concepts, Implementations, Applications*. Wiley-VCH Verlag GmbH, **2018** (ISBN: 978-3-527-34038-5)
- [Taylor, D. P.](#); Zeaf, I.; Lovchik, R. D.; Kaigala, G. V. "Centimeter-Scale Surface Interactions Using Hydrodynamic Flow Confinements." *Langmuir*, **2016**, *32* (41), 10537-10544.
- Autebert, J.; Cors, J. F.; [Taylor, D. P.](#); Kaigala, G. V. "Convection-Enhanced Biopatterning with Recirculation of Hydrodynamically Confined Nanoliter Volumes of Reagents." *Anal. Chem.*, **2016**, *88* (6), 3235-3242.
- Rensch, C.; Lindner, S.; Salvamoser, R. H.; Leidner, S.; Böld, C.; Samper, V.; [Taylor, D. P.](#); Baller, M.; Riese, S.; Bartenstein, P.; Wängler, C.; Wängler, B. "A solvent resistant lab-on-chip platform for radiochemistry applications." *Lab Chip*, **2014**, *14* (14), 2556 – 2564.

MANUSCRIPTS IN PREPARATION

- [Taylor, D. P.](#); Manthur, P.; Squires, T. M.; Renaud, P.; Kaigala, G. V. "Review: hydrodynamic confinement of flow at the microscale."
- Lovchik, R. D.; [Taylor, D. P.](#); Kaigala, G. V. "Rapid Multiplex-Immunohistochemistry."

CONTRIBUTIONS TO CONFERENCES

- Taylor, D. P.; Cors, J. F.; Autebert, J.; Lovchik, R. D.; Delamarche, E.; Kaigala, G. V. "Microfluidic probe platforms to locally alter the physics & chemistry on biological surfaces." *Nanobiotech Montreux*, **2014**, Montreux, Switzerland, **poster presentation**
- Taylor, D. P.; Zeaf, I.; Lovchik, R. D.; Kaigala, G. V. "Efficient mm-scale immunohistochemistry on tissue sections using hydrodynamically confined liquids." *Nanobiotech Montreux*, **2015**, Montreux, Switzerland, **poster presentation**
- Taylor, D. P.; Cors, J. F.; Autebert, J.; Oskoei, A.; Kaigala, G. V. "Tailoring μm length-scale interactions of hydrodynamically confined liquids with immersed substrates." *Basheva de Rothschild Seminar on Physics of Microfluidics*, **2017**, Sde Boker, Israel, **poster presentation**
- Taylor, D. P.; Kaigala, G. V. "Reconfigurable Microfluidics: Real-time shaping of virtual channels through hydrodynamic forces." *Harrington Symposium on Physics of Microfluidics*, **2019**, Austin, USA, **poster presentation**
- Taylor, D. P.; Kaigala, G. V. "Reconfigurable Microfluidics: Real-time shaping of virtual channels through hydrodynamic forces." *13th Southern California Flow Physics Symposium*, **2019**, Santa Barbara, USA, **oral presentation**
- Taylor, D. P.; Kaigala, G. V. "Reconfigurable Microfluidics: Real-time shaping of virtual channels through hydrodynamic forces." *23rd International Conference on Miniaturized Systems for Chemistry and Life Sciences*, **2019**, Basel, Switzerland, **oral presentation**

PATENTS

- Kaigala, G. V.; Lovchik, R. D.; Taylor, D. P.; Zeaf, I. Device for centimeter-scale processing of surfaces with hydrodynamic flow confinement. CH920150116US1, submitted **06/28/2015**.
- Taylor, D. P.; Lovchik, R. D.; Kaigala, G. V. Bypass channels for passive compensation of failures during usage of microfluidic probes. CH920160096US1, submitted **08/18/2016**.
- Kaigala, G. V.; Lovchik, R. D.; Taylor, D. P.; Trainito, C. I. Specialized microfluidic probe heads for cell deposition on a surface. CH920160060, submitted **04/26/2016**.
- Lovchik, R. D.; Taylor, D. P.; Bürge, M.; Kaigala, G. V.; Barak, I.; Yochanan, U. Device for hydrodynamically confining bio-chemicals within microtiter plates. CH820160144, submitted **07/13/2016**.

AWARDS AND HONORS

- Outstanding Technical Achievement Award, IBM Research – Zurich, May 2018
- Doc.Mobility fellowship, Swiss National Science Foundation, May 2018
- Patent Plateau Award, IBM Research – Zurich, May 2017

SKILLS AND ABILITIES

Languages

German (native), English (fluent), French (advanced), Spanish (advanced)

Laboratory skills

Microfabrication (photolithography, wet and dry etching, glass etching, wafer bonding, thin film deposition, polishing and dicing, metrology), microfluidics (design and fabrication of microfluidic devices and flow control systems, surface treatments, flow and pressure sensing, formation and handling of suspensions and dispersions, handling of biological and clinical samples), fluorescence and confocal microscopy, optical systems (laser safety officer certification according to the German regulation §6 BGV B2), microcontrollers, setup automation, mechanical processing (turning, milling, CNC operated systems), training in handling of radioactive substances (German certification "Fachkunde Strahlenschutz")

Computing

Matlab/Simulink/Simscape, Minitab, Comsol Multiphysics, ANSYS, OpenFOAM, SolidWorks, Catia, LabView, C++, Python, ImageJ, Inkscape, Blender, GIMP, LaTeX, Microsoft Office

Free-time activities

Spending time with our kids Levi (4) and Noa (1), foreign languages (learning Arabic) and travelling, playing guitar, outdoor sports (running, hiking, biking), voluntary firefighter (Thalwil fire department, respiratory protection team, heavy vehicle operator)

